SMART NANOCOMPOSITES

Volume 1 Issue 2

Table of Contents

Nova Science Publishers, Inc.
New York

Smart Nanocomposites

This Journal presents new studies in the fast growing area of smart materials, in particular, composite nanostructured materials. It focuses on the physics and physical chemistry of surfaces, interfaces, thin films and coatings, nanoparticles and other nanostructures, as well as on their new and smart applications. Original approaches in fabrication and applications of nanostructured materials will get special attention. Nanostructured ceramics, alloys, various nanocarbon forms (nanotubes, fullerenes, graphene) and their composites used in sensors (including single molecule sensing) and actuators, artificial metabolism, drug delivery, selective membranes, fuel cells, energy storage, and photovoltaics are just a few examples of new classes of materials and applications that are within the scope of the Journal. It features the results of interdisciplinary research from universities, national labs, and privately owned companies.

The Journal is peer-reviewed with the highest standards and quality of publications. The purpose of this Journal is to bring the most up-to-date advances in nanotechnology together, and to give research groups the opportunity to compare their results with other groups' data. To achieve this, the Journal focuses mostly on practical applications of nanodevices, and on proof of the concept publications. Areas of interest include (but not are limited to): sensors, smart membranes, smart coatings for corrosion protection, aspects of significance to nanorobots: power supplies, nanorobot manipulating devices, and microchips for artificial intelligence. The Journal also deals with safety issues: safety of nanotechnology to the environment, controlling the nanodevices, and other aspects.

Smart Nanocomposites

is published quarterly by

Nova Science Publishers, Inc.

400 Oser Avenue, Suite 1600

Hauppauge, New York 11788-3619, U.S.A.

Telephone: (631) 231-7269

Fax: (631) 231-8175

E-mail: novapublishers@earthlink.net

Web: www. novapublishers.com

Institutional Subscription Rate (2011): $195

Personal Subscription Rate (2011): $50

ISSN: 1949-4823

Instructions for manuscript preparation can be found on our website.

Additional color graphics may be available in the e-journal version of this journal.

Smart Nanocomposites
Volume 1, Issue 2
ISSN: 1949-4823

MOLECULAR DESIGN OF PRECURSOR IN THE SYNTHESIS OF CATALYTIC NANOCOMPOSITE SYSTEM PT-AL_2O_3

***O. B. Belskaya*[1,2], *V. K. Duplyakin*[1] *and V. A. Likholobov*[1,2]**
[1]Institute of Hydrocarbons Processing SB RAS (Omsk), Omsk, Russia
[2]Omsk State Technical University, Omsk, Russia

ABSTRACT

The effect of the transformation sequence of metal complex precursor at the early stages of catalyst preparation on the state of platinum nanoparticles composing the active surface of the finished catalyst is demonstrated using the formation of catalytic nanocomposite system Pt/Al_2O_3 as an example. The existing views on the nature of chemical binding between metal complexes and the support surface are reported. Approaches to quantitative differentiation of the ion-exchangeable (outer-sphere) and coordinatively bound (inner-sphere) adsorbed metal complex species, determination of their chemical composition, and synthesis of catalysts from the supported precursor uniformly interacting with the support are considered.

INTRODUCTION

As known, the term ‘nanomaterials’ embraces a wide spectrum of various-purpose substances. The size of catalysts, except bulk ones, allows regarding them as nanomaterials, which are the subjects of scientific investigation and commercial products for industry. Hence, long before the emergence of a new science — nanotechnology — catalyst designers dealt with the nanosized structures of functional substances.

The world annual sales of catalysts exceed 10 billion US dollars [1]; these catalysts are used to produce tens of thousands items of products only from mineral resources (natural gas, oil and carbon) amounting to 10 trillion US dollars [2]. Besides, selective catalysis is the key to ‘green chemistry’, which implies the transformation of raw material into the target product

* E-mail: obelska@ihcp.oscsbras.ru

without any by-products. Thus, owing to its range of activity and importance, the catalyst industry is going to become a base sector of nanoindustry.

In this field, innovations are aimed at developing the advanced methods for synthesis of nanoporous and nanostructural materials. Nanoparticles of noble metals, such as Pt, Pd, Rh, Au, and their alloys with other metals dispersed over the high surface area supports are widely used to catalyze the transformations of organic molecules (oil refinement, petrochemistry, general and fine organic synthesis, pharmacy, etc.). However, the fundamental knowledge of molecular structure and reactivity of these systems remains rather limited. Now it is clearly understood that nanoparticle size, shape, structure and composition are essential for attaining high catalytic performance [3]. For a particle size less than 1.5 nm, the size effect should be examined in combination with the electronic state of atoms [3, 4]. Novel approaches and new knowledge are vital for the development of methods that could produce stable metal nanoparticles with strict control of size, shape and electronic state of atoms, which determine the pronounced functional properties of the catalyst.

The conventional empirical approach guided by experience, scientific intuition and analogies is not sufficient for effective solution of this problem; a more promising basis is the ideology of chemical constructing of nanocomposites that provides for a continuous molecular design of precursors over the entire technological chain aimed at creation of a new functional material.

This work is devoted to the development of such new approach exemplified by the synthesis of platinum-on-alumina systems, which are typical representatives of supported catalysts of the adsorption type. For many decades, alumina–platinum catalysts have been among the most used catalytic systems widely employed in oil refinement, petrochemistry, and exhaust gas remediation. However, to avoid reduction of the study to special cases, these objects are considered as systems rather than catalysts for individual reactions; so, a usual problem of improving the empirically attained level of catalytic performance is not set here. The objective is to reveal general regularities and generalizations that have a predictive power and provide deep insight into the processes of active component formation.

The common preparation procedure for this type of catalysts includes several stages: adsorption of the active component from aqueous solution of transition metal complex onto support, drying, calcination and reduction of the sample.

Consideration of this multistage scheme of synthesis is often accompanied by discussions concerning the relevance and expedience of comprehensive examination of processes at each stage of the synthesis. In particular, it is believed that investigation of initial stages, including the transformation of metal complex precursors in aqueous solutions and on the alumina surface upon sorption interactions, is of little practical importance because high-temperature treatments employed in the catalyst preparation bring the system to an equilibrium state irrespective of its ‘past history’.

This statement may be true in some cases, but it is not a general rule, as will be shown below. In the review, main attention is focused on the studies of chemical transformations of metal complexes specifically at the initial stages of catalyst preparation: these are the studies of parent solutions of metal complexes, adsorption of a precursor, and catalyst drying. Within a typical adsorption system H_2PtCl_6 Al_2O_3, we consider approaches to differentiation between the mechanisms of metal complex fixation to the support and show the role of precursor nature and type of its binding to the support in the properties of active component being formed. Our review is based particularly on the studies (both published and unpublished) that

were performed at the Institute of Hydrocarbons Processing of Siberian Branch of Russian Academy of Sciences (IHP SB RAS) in the period of 2005–2010.

THE STATE OF PLATINUM CHLORO COMPLEXES IN AQUEOUS SOLUTIONS

In the preparation of supported catalysts, transition metal complexes are often used as precursor compounds of the active component. In the case of alumina–platinum catalyst, such complex precursor is conventionally represented by chloroplatinic acid $H_2[PtCl_6]$. It is essential that the chemical composition of these complexes in solution, closeness to thermodynamic equilibrium and their charge state largely determine the nature of further sorption processes. Thus, to understand processes taking place at the first stage of catalyst preparation — the interaction of support with aqueous solution of metal complex — information on the chemical reactions proceeding upon $H_2[PtCl_6]$ dissolution in water and factors that may affect the state of complexes in solution is necessary.

Hydrolysis of complex platinum chloro compounds was first reported at the beginning of the XX century [5-6]. More comprehensive studies have been performed since 1950s by representatives of Russian [7-17] and foreign [18-27] scientific schools. The extent of hydrolysis was estimated mainly from the electrical conductivity of solution and the concentration of chloride ions. Further works [28-34] dealt with the processes of acid and alkaline hydrolysis; results of kinetic measurements and identification of Pt(IV) aqua, hydroxo and mixed aquahydroxo complexes in solutions were reported. The main methods used to investigate and identify metal complexes in solutions were electron spectroscopy [22, 30, 31], ^{195}Pt NMR [18, 23, 24, 33], and in more recent studies, EXAFS (extended X-ray absorption fine structure spectroscopy) [34].

Analysis of the literature reveals three principal models of chloroplatinate hydrolysis reported by Miolati [5], Sillen [19] and Knozinger [35]. The earliest of these works suggests the occurrence of only one type reactions — exchange of chloride ligands for hydroxide ions, and does not take into account that aquated species may form and complex ions with a charge different from –2 may be present. The Knozinger's model [35] supposes that $H_2[PtCl_6]$ is capable of substituting only two chloride ligands by aqua or hydroxo groups. Sillen et al. [19] consider $H_2[PtCl_6]$ as a strong dibasic acid, but also limit the extent of its hydrolysis by two stages, which may be explained by the use of fairly concentrated solutions and insufficiently broad pH range in their work. Further examination of the processes occurring in aqueous solutions of these complexes was made by Lambert et al. [36] and Regalbuto et al. [34] by means of EXAFS and ^{195}Pt NMR spectroscopy.

Some of the works consider not only thermodynamic and kinetic aspects of the ligand exchange reactions in the platinum(IV) chloro complexes, but also the factors accelerating hydrolysis of the complexes in solution. Such factors include temperature [13, 29], exposure to light [28, 32], and introduction of a catalyzing component into solution [11, 25, 37], for example, the Pt(II) complex [11, 37].

Thus, the existing concepts of chloroplatinate hydrolysis suggest that, depending on conditions, aqueous solution may contain a wide spectrum of mixed complexes that differ not only in their chemical composition, but also in the charge. Spieker et al. [34] analyzed all

theoretically possible octahedral complexes of Pt(IV) with chloride, hydroxide and aqua ligands (isomeric species are neglected). High concentrations of $H_2[PtCl_6]$ and Cl^- as well as low pH are advantageous for maximum coordination of chlorine and hydrolysis leading to aquated species. In contrast, low concentrations of $H_2[PtCl_6]$ at increasing pH values and absence of excess chloride ions can result in profound hydrolysis of the complex with the formation of hydroxo species. Thus, a combination of some parameters (concentration of chloroplatinic acid and chloride ions, acidity, duration of aging, light, temperature, admixtures) may increase the probability of forming one or another complex. Therefore, the contradictory literature data on the state of platinum complexes in solution can be explained both by imperfect laboratory equipment used in the early works and by insufficiently comprehensive control of experimental conditions.

In [38], chemical transformations of Pt(IV) chloro complexes in the impregnating solutions with the platinum concentration 0.5–10.3 mmol/l, which are used for preparation of both the model and commercial catalyst, are considered. The concentration measurement of hydrogen ions and free noncoordinated chloride ions, which appear in the solution due to hydrolysis of complex anion, in combination with the analysis of EXAFS and UV spectra of solutions revealed that, even in diluted solutions, main amount of chloride ions resides in the coordination sphere of platinum, and the averaged composition of the complexes corresponds to the formula $[PtCl_{5.7}(H_2O)_{0.3}]^{-1.7}$.

Meanwhile, even holding the solutions at natural lighting may strongly affect the chemical composition of platinum complexes [39]. Hydrolysis of the complexes can be monitored by the decreasing intensity of the characteristic Cl–Pt charge transfer band (262 nm (*38000 cm^{-1}*)) in the electronic spectrum of $[PtCl_6]^{2-}$ [37, 40] (Figure 1). Simultaneous measurement of the concentration of protons and free chloride ions in the solution allowed determining the averaged composition of hydrolyzed species. Thus, mixed aquachloro hydroxo complexes of the calculated composition $[PtCl_3(OH)(H_2O)_2]^0$ with the charge close to zero were found in a solution exposed to light for 5 h.

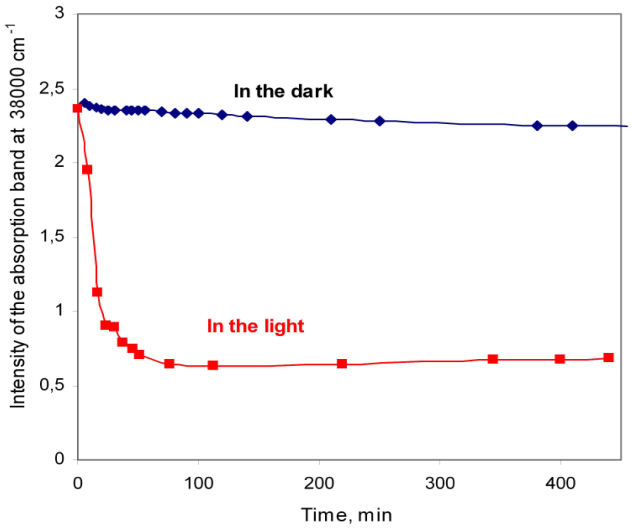

Figure 1. Evolution of the absorption band at 38000 cm^{-1} in the electronic absorption spectrum of $H_2[PtCl_6]$ solution in the dark and in the light.

Another topical question is the effect of temperature on hydrolysis of the complexes, because in the synthesis of supported catalysts, heat release takes place when support is wetted with the impregnating solution, hot impregnation is often used, and elevated temperatures are needed to remove solvent from the pores (especially meso- and micropores) in the case of precursor solution localized in the pore space of support. In all these stages, metal complex is under hydrothermal conditions. Experiments [41], where solutions of chloroplatinic acid ($0.5\ 10^{-3}$ M) were heat treated in the dark at 50, 80, 100 and 150°C, showed that thermal treatment substantially accelerates the hydrolysis, especially at temperatures above 80°C. Note that the specified conditions led to the preferential formation of anionic hydroxo species of $[PtCl_4(OH)_2]^{2-}$ composition, probably due to acceleration of the aqua ligands deprotonation [41].

It was found that the extent of chloroplatinate hydrolysis under hydrothermal conditions can be increased considerably by the introduction of palladium(II) into solution of the chloro complex [42]. The joint presence of metal complexes inhibited the hydrolysis of the labile palladium complex (the intensity of the characteristic charge transfer band at 237 nm remained virtually unchanged). At the same time, a more profound hydrolysis of chloroplatinate, up to the formation of insoluble hydroxo complex, was observed. The electronic absorption spectrum showed a decrease in the intensity of chloroplatinate band (charge transfer band at 262 nm) (Figure 2), and the platinum concentration in the solution decreased nearly twofold, from 0.5 to 0.26 mmol/l, whereas the palladium concentration remained virtually constant. The heating might accelerate ligand exchange in the complexes, which made possible the migration of chloride ligands from the tetravalent platinum complex to the bivalent palladium complex with the formation of a platinum(IV) aqua complex. This process is feasible if the aquation of the platinum(IV) chloro complex is thermodynamically more favorable than the further aquation of the $[PdCl_3(H_2O)]$ complex:

$$[PtCl_6]^{2-} + H_2O \leftrightarrow [PtCl_5(H_2O)]^- + Cl^- \qquad lgK_5(st) = 2.20\ [12] \qquad (I)$$

$$[PdCl_3(H_2O)]^- + H_2O \leftrightarrow [PdCl_2(H_2O)_2] + Cl^- \qquad lgK_3(st) = 2.68\ [43] \qquad (II)$$

Therefore, the $[PdCl_2(H_2O)_2]$ complex can bind Cl^- into $[PdCl_3(H_2O)]^-$ more strongly than the $[PtCl_5(H_2O)]^-$ complex into $[PtCl_6]^{2-}$. The literature gives only limited information about cumulative and stepwise stability constants of these complexes, especially for the kinetically inert Pt(IV) complexes. However, according to [12, 43], the equilibrium constant of the reaction (I) ($[PtCl_6]^{2-}$ aquation) is actually three times greater than that of the reaction (II). The revealed facts are quite surprising and indicate the discovery of a new phenomenon: the hydrolysis of a stable and inert $[PtCl_6]^{2-}$ complex becomes more profound after addition of more labile and prone to hydrolysis substances ($[PdCl_4]^{2-}$).

Thus, analysis of the results obtained for aqueous solutions of chloroplatinic acid demonstrates that main chemical transformations of Pt(IV) chloro complexes can be estimated at a quantitative level, and the effect of most important factors, such as chloroplatinate concentration, light, temperature, and presence of a more labile metal complex, on the process of their hydrolysis can be determined. In the general case, these data emphasize the importance of a preliminary study of impregnating solution for scientific bases of catalyst preparation.

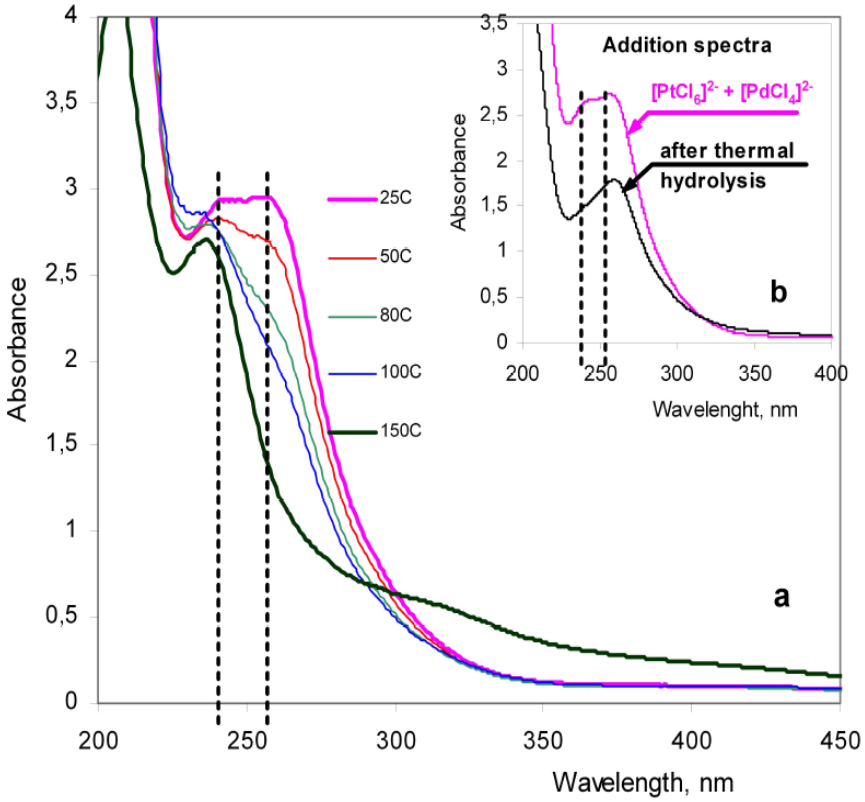

Figure 2. Thermal hydrolysis of aqueous solutions of a mixture of H_2PtCl_6 and H_2PdCl_4: (a) experimental spectra of solutions held at 25 to 150°C; (b) addition spectra as the superposition of the spectra of the initial platinum and palladium complexes at 25°C and of the platinum and palladium complexes subjected to thermal hydrolysis at 150°C.

Such study will reveal the chemical composition and structure of precursor, whose chemical transformations start from dissolution of the initial substance and are further determined by numerous conditions of the synthesis. The derived regularities allow one to control the transformation of metal complexes in aqueous solution and make a reasonable rather than empirical choice of conditions for their fixation to the support at the impregnation stage.

THE COMPOSITION OF FIXED PLATINUM COMPLEXES AND THE NATURE OF THEIR INTERACTION WITH SUPPORT

Numerous studies are devoted to adsorption of platinum complexes on different oxide surfaces in a broad range of pH [44-48]. The work by Brunelle (1978) [49] was among the first reviews dealing with adsorption of noble metal complexes on mineral oxides. The analysis of experimental data and his views of the precursor fixation are based on ‘electrostatic adsorption’. Although the study was made at a qualitative level, the proposed approach dominated for long years. Later, it was used to develop a model of ‘physical

adsorption', which is examined in detail by Regalbuto et al. for the adsorption of platinum(IV) chloro complexes [50-61].

The model of 'physical adsorption' (RPA, revised physical adsorption model) implies the electrostatic interaction between the anionic platinum complexes present in the impregnating solution and the alumina surface, which is protonated and positively charged at low pH of solution. In this case, the chemical composition and structure of metal complexes in the solution are similar to those fixed on the surface. Main simplification underlying the model and casting doubt upon its correctness for the surface processes is that in the case of platinum adsorption only the double-charged anion $[PtCl_6]^{2-}$ is considered, and a possible formation of aquated complexes with different charge in aqueous solution at certain concentration and pH values [34] is neglected. However, in some of their studies [51, 61], Regalbuto et al. tried to interpret platinum adsorption from uncharged complexes by the electrostatic adsorption mechanism. According to their ideas, even at a moderately high solution pH, platinum is adsorbed as a double-charged anionic complex, which forms from uncharged species upon contacting with the surface, either via fast H_2O-OH exchange in the coordination sphere of platinum at high pH of the adsorption layer (III):

$$[PtCl_2(OH)_2(H_2O)_2]^0 \leftrightarrow [PtCl_2(OH)_4]_2^- + 2H^+ \quad \text{(III)}$$

or via protonation of the alumina surface (IV):

$$2Al\text{--}OH + [PtCl_2(OH)_2(H_2O)_2]^0 \leftrightarrow 2Al\text{—}OH_2^+\text{--}[PtCl_2(OH)_4]^{2-}. \quad \text{(IV)}$$

On the other hand, to describe a great body of experimental data accumulated in recent decades, one should take into account the possibility of not only electrostatic, but also more specific interactions [62]. As a result, a model of 'chemical adsorption' was suggested, according to which fixation of transition metal complexes is accompanied by their more profound interaction with the oxide surface via the ligand exchange with the surface groups. Surprisingly, even similar experimental results obtained for the same catalytic system are described by different research groups either in terms of electrostatic model or on the hypothesis that only specific adsorption takes place. For example, fixation of the platinum(IV) chloro complexes on the alumina surface can be considered in the context of coordinative interaction. At that, the leaving group may be either a chloride ion of the platinum complex or a surface hydroxo group of the support [63, 64]:

$$\sim Al\text{--}OH + [PtCl_6]^{2-} \leftrightarrow \sim Al\text{--}[(OH)\text{-}PtCl_5]^- + Cl^- \quad \text{(V)}$$

$$\sim Al\text{--}OH + H_3O^+ + [PtCl_6]^{2-} \leftrightarrow \sim Al\text{--}[Cl\text{-}PtCl_5]^- + 2H_2O \quad \text{(VI)}$$

It is essential that this mechanism allows the hydroxyl ligand exchange between partially hydrolyzed complexes and neutral or negatively charged surface:

$$\sim Al\text{--}OH + [PtCl_4(OH)_2]^{2-} \leftrightarrow [\sim Al(OH) - PtCl_4(OH)]^- + OH^- \quad \text{(VII)}$$

$$\sim AlO^- + [PtCl_4(OH)(H_2O)]^- \leftrightarrow [(\sim AlO) - PtCl_4(H_2O)]^- + OH^- \quad \text{(VIII)}$$

Various metal complexes may exist in H_2PtCl_6 aqueous solutions in dynamic equilibrium, and the surface OH groups of alumina may have different acidic properties. This gives grounds to suppose not only the existence of adsorbed complexes with different extent of hydrolysis, but also the possibility of simultaneous implementation of different mechanisms of their binding to the oxide support. Nevertheless, only a few works [36, 65-68] admit that electrostatic binding, where the so-called outer-sphere complexes reside on the surface, may take place simultaneously with a deeper interaction leading to inner-sphere complexes with the surface groups (Al-OH) (Figure 3). It was deduced from variation of ^{195}Pt NMR intensity that coordination binding becomes irreversible as the temperature is raised up to 90°C [36].

It is assumed also that aluminum ions of the support are directly involved in the sorption of platinum complexes [69]. The dissolution of a small part of alumina upon interaction with chloroplatinic acid is considered as the first stage of the process. This is followed by the interaction between the hydrolyzed Al^{3+} cation that passed into solution and the $[PtCl_6]^{2-}$ anion and by their joint adsorption on the support surface with the formation of ~Al-O-$Al^{2+}[PtCl_6]^{2-}$. However, it seems unlikely that dissolution of the support can significantly contribute to platinum fixation, because this process is much slower as compared to the metal complex sorption [70].

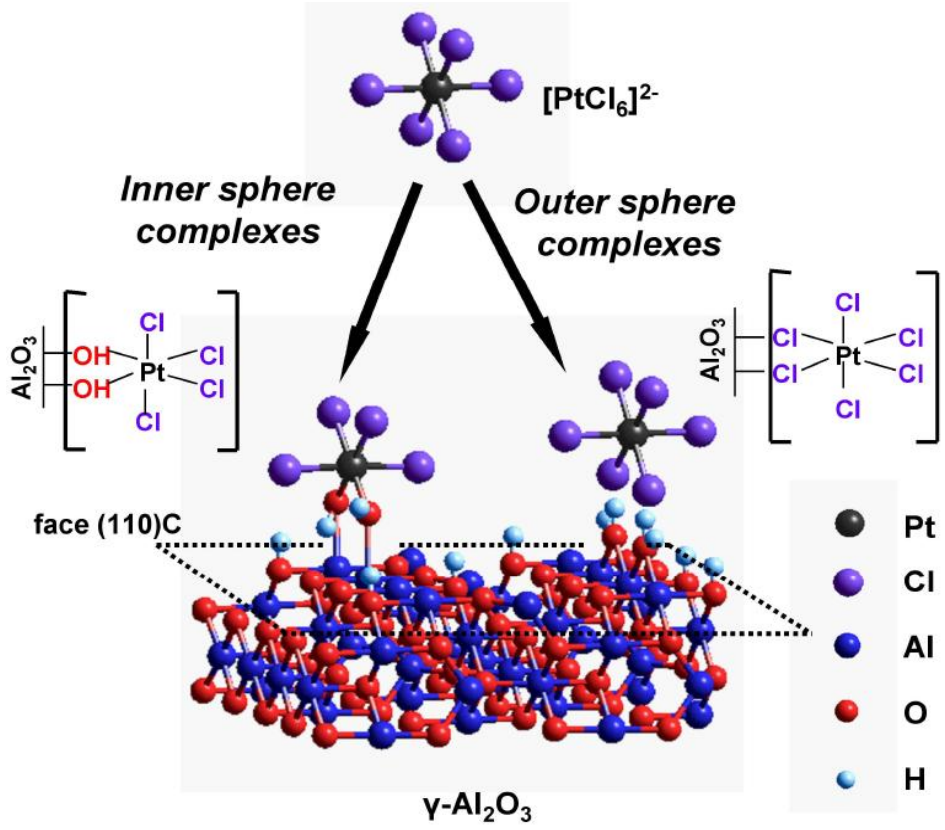

Figure 3. Illustration of existing views on the types of interaction between platinum(IV) chloro complexes and surface groups of alumina via the formation of outer- and inner-sphere complexes.

Besides, metal complex fixation may depend on the choice of preadsorbed modifying anion. In particular, on alumina pretreated with perchloric, hydrofluoric and acetic acids, platinum is fixed by the mechanism of ClO_4^-, F^-, CH_3COO^- exchange for a metal complex ion [54, 71-73]. Spectral characteristics of both the surface and desorbed complexes correspond to $[PtCl_6]^{2-}$. Meanwhile, chloroplatinate sorption on prebrominated alumina leads to the mixed chlorobromo complexes of platinum, which directly indicates the occurrence of the ligand substitution reaction. The adsorption site contains 1 to 5 Br atoms, whereas mixed Pt complexes are represented exclusively by cis-isomers [71].

A detailed systematization of the methods used for metal complex fixation in the synthesis of supported catalysts in terms of underlying processes is presented in a recent review by Bourikas et al. (2006) [62]. Although methods of precursor fixation are numerous (electrostatic adsorption through ion pair formation in the outer or in the inner plane of the compact region of the interface, retention through hydrogen bond formation, formation of inner sphere surface complexes, surface dissolution of the support and formation of mixed solid phases, surface or interface oligomerization, polymerization and precipitation, etc [62]), analysis of the nature of interaction between metal complex and support usually deals with two extreme cases: nonspecific (electrostatic interaction) and specific (formation of the inner-sphere surface complexes) adsorption. The preferential occurrence of one or another type depends on the nature of both participants of the synthesis and on the conditions of supporting. The most essential parameters are pH, the concentration of metal complex, ionic strength of solution, temperature and impregnation time.

Indeed, revealing the nature of metal complex – support interaction is very important for prediction of the catalytic system properties. Thus, the formation of coordinatively bound inner-sphere complexes at the stage of precursor fixation will tighten the interaction between metal complex and support and result in the formation of highly dispersed catalysts. A conventional analysis of the interaction between metal complex solution and support in the catalyst synthesis includes control of the active metal concentration in solution before and after the sorption, acidity of the medium, and appearance in the impregnating solution of possible products of precursor compound transformation, e.g., during hydrolysis. Upon interaction of chloroplatinic acid solutions with the alumina surface, adsorption of the complexes is accompanied by a sharp increase in the solution pH and by appearance of extra Cl^- ions in the equilibrium solution [38].

According to current concepts of the mechanisms of $H_2[PtCl_6]$ fixation [36, 51, 63-66], neutralization of protons, which increases the solution pH, takes place at their interaction with hydroxo groups of the support, and the increase in the chloride ion concentration in the solution after platinum adsorption can be attributed both to hydrolysis of the adsorbed complex caused by increasing pH of the impregnating solution and to replacement of Cl^- by the entering hydroxide ligands of the support.

Study of the adsorbed platinum complexes by EXAFS and diffuse reflectance spectroscopy demonstrated that interaction with the support surface gives rise to substantial changes in the coordination sphere of platinum. As follows from EXAFS data for the supported complexes (Figure 4), the average oxygen coordination number is 3 [38]. The charge transfer band in the electronic spectra of platinum complexes is shifted to the high frequency region, which also indicates an increase in the amount of oxygen-containing ligands in the coordination sphere of platinum [37, 40].

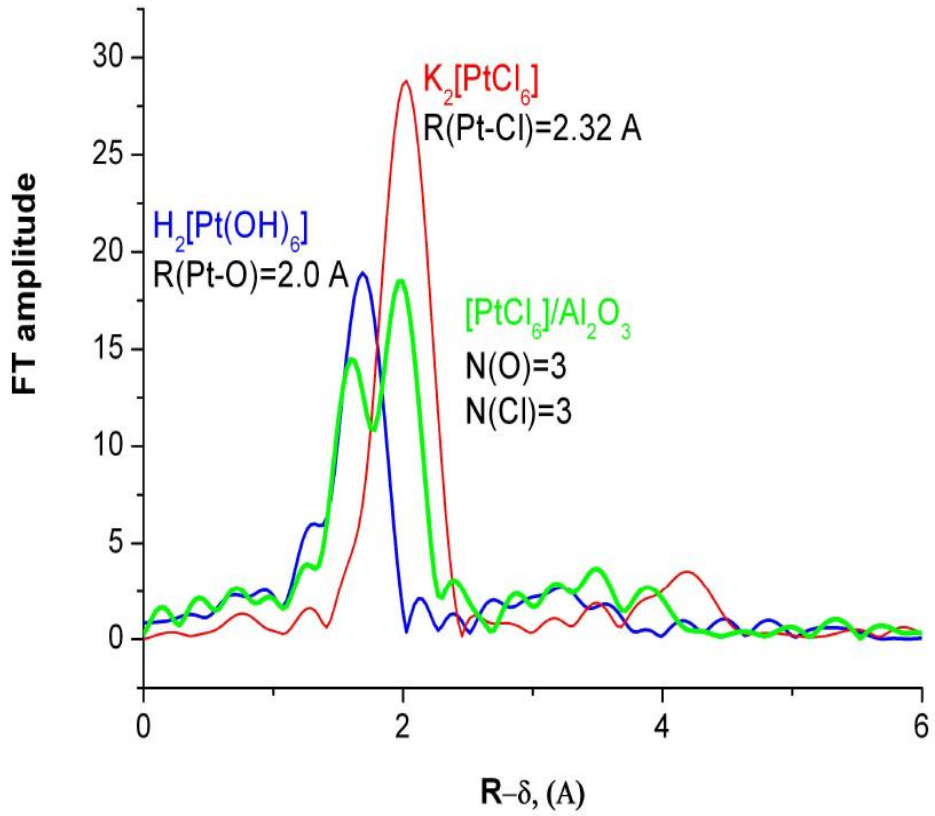

Figure 4. Atomic radial distribution curves from EXAFS for sample H_2PtCl_6/Al_2O_3 (2% Pt, N(O) = N(Cl) = 3) and for the reference compounds $K_2[PtCl_6]$ (N(Cl) = 6, R(Pt–Cl) = 2.32 Å) and $H_2[Pt(OH)_6]$ (N(O) = 6, R(Pt–O) = 2.0 Å). The sample was dried at 25°C for 50 h before examination [38].

The results obtained by physical methods provide an averaged information. To assess the uniformity of adsorbed complexes in terms of their chemical composition and nature of interaction with the support, it was suggested to use sequential desorption of surface complexes followed by separate investigation of desorbed species in the solution (electron spectroscopy, ionometry) and undesorbed species on the surface (diffuse reflectance spectroscopy, EXAFS).

The surface platinum species fixed via electrostatic interaction on the protonated alumina surface in the form of anionic complexes can be removed by 'recharging' of the surface. In this case, a gradual increase of the eluent pH to the values exceeding the zero charge point of the surface results in desorption of the anionic platinum complexes [38]. Another method was also used in [38, 41, 74]: the fixed anionic platinum complexes passed from the surface to solution upon competitive adsorption of specially chosen anions. The desorbing solution was composed of acids having different basicities. As the concentration and desorbing power of competing anions were increased (gradient elution), the ion-exchangeable platinum complexes were forced out. The resulting high acidity of the medium hindered hydrolysis of the complexes, and the anionic part of acids in the eluent solution (A^{n-}), competing for the adsorption sites of the support, forced out the surface complexes into solution without changing the coordination sphere of platinum.

$$Al\text{-}[Pt(H_2O)_xCl_{6-x}]_{surf} + A^{n-}{}_{p\text{-}p} \leftrightarrow Al\text{-}A_{surf} + [Pt(H_2O)_xCl_{6-x}]^{m-}{}_{p\text{-}p} \quad (IX)$$

Irrespective of the desorption technique used (the elution with changes in the eluent pH or the acidic elution), a part of the fixed platinum species was not removed from the alumina surface [38]. Probably, their interaction with alumina was not based on ion exchange, rather it followed the coordination mechanism with ligand substitution in the coordination sphere of platinum, alumina serving as a macroligand. Analysis of the desorption profiles (Figure 5) made it possible to distinguish the regions of platinum removal corresponding to desorption of the complexes adsorbed on the support surface with different strengths; moreover, a quantitative separation of desorbable ion-exchanged species and nondesorbable coordinatively bound platinum species was made.

Study of the eluates by electron spectroscopy and ionometry revealed that a Cl/Pt ratio in the readily desorbable complexes is close to 5, whereas more strongly bound species are hydrolyzed to a great extent. According to EXAFS data on the composition of complexes at the support surface (Table 1), the removal of species weakly bound to the support increases the amount of oxygen-containing ligands in the coordination sphere of platinum. Thus, the strength of platinum fixation correlates with the precursor composition: the metal complex – support interaction is stronger when platinum is present as the partially hydrolyzed species. In this case, nondesorbable coordinatively bound complexes had an oxygen coordination number of N(O) = 4 and were represented by the surface compounds of composition $PtCl_2O_4$.

Results of the studies [38, 41, 74] allowed the authors to suggest the following scheme of reactions proceeding upon fixation of metal complexes on the alumina surface:

$$\sim Al\text{—}2OH + 2H^+ + [PtCl_6]^{-2}$$
$$\Downarrow 1$$
$$\sim Al\text{—}2OH_2^+ \text{-} [PtCl_6]^{-2}$$
$$\Downarrow 2$$
$$\sim Al\text{-}[\text{-}(OH)_2\text{—}PtCl_4] + 2Cl^- + 2H^+$$
$$\Downarrow 3$$
$$\sim Al\text{-}[\text{-}(OH)_4\text{—}PtCl_2] + \sim Al\text{—}2Cl + 2Cl^- + 2H^+,$$

where ~Al—OH stands for the alumina surface.

The first of these reactions is fast electrostatic adsorption, which is accompanied by a sharp growth of pH and causes no changes in the chemical composition of the bound metal complex. The second reaction leads to a partial substitution of chloride ligands in the $[PtCl_6]^{2-}$ complex by the surface groups of the support: a more strongly bound complex $[PtCl_4(OH)_2]^{2-}$ is formed, which can desorb only under the action of di- and tribasic competing acids. A nondesorbable species (reaction 3) is the product of further transformation of the metal complex in the adsorption layer: a profound chloroplatinate hydrolysis (coordination number

of N(O) = 4), probably involving the most basic OH groups of the support, and formation of the inner-sphere complexes take place.

Table 1. EXAFS data for samples obtained by sequential desorption of surface complexes. Samples were dried at 25°C for 48 h before examination [38]

Entry	Sample	R(Pt-Cl)	N(Cl)	R(Pt-O)	N(O)
1	$Pt/\gamma Al_20_3$ initial	2.29	3.0	1.98	3.0
2	$Pt/\gamma Al_20_3$ (I) weakly bound species are desorbed	2.28	2.3	1.99	3.7
3	$Pt/\ \gamma Al_20_3$ (I+II) two kinds of platinum species are desorbed	2.30	2.2	2.03	3.8
4	$Pt/\ \gamma Al_20_3$ (I+II+III) surface platinum species nondesorbable by ion exchange	2.30	1.9	2.01	4.1

Note: R(Pt–Cl) and R(Pt–O) are the Pt–Cl and Pt–O bond lengths, respectively;
N(Cl) and N(O) are, respectively, the chlorine and oxygen coordination numbers of the Pt atom.

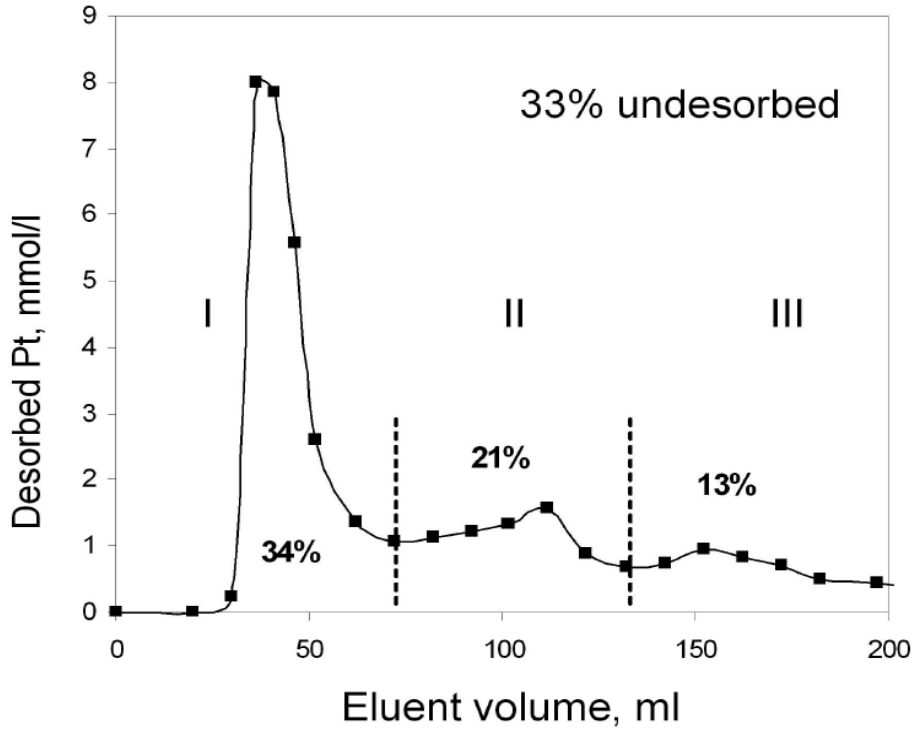

Figure 5. Results of the gradient elution of platinum compounds with solutions of chloric ($HClO_4$), oxalic ($C_2O_4H_2$), citric ($C_6O_7H_8$) acids. The sample was dried at 25°C for 48 h before desorption experiments. For desorption region I, the eluent composition is 1N $HClO_4$ + 0.1N $C_2O_4H_2$ + 0.01N $C_6O_7H_8$; for desorption region II, 1.8N $HClO_4$ + 0.5N $C_2O_4H_2$ + 0.3N $C_6O_7H_8$; for desorption region III, 1.2N $HClO_4$ + 0.6N $C_2O_4H_2$ + 0.7N $C_6O_7H_8$.

Temperature-programmed reduction (TPR) showed (Figure 6) that sequential removal of adsorbed species differing in the chemical composition and strength of their interaction with the support increases the reduction temperature of complexes remaining on the surface. At that, nondesorbable platinum species (after platinum removal, in regions I, II and III of the gradient elution profile (Figure 5)) were reduced at a temperature above 300°C (Figure 6c). Therefore, samples with a uniform coordinative fixation of precursor can be obtained by the removal of ion-exchangeable platinum species.

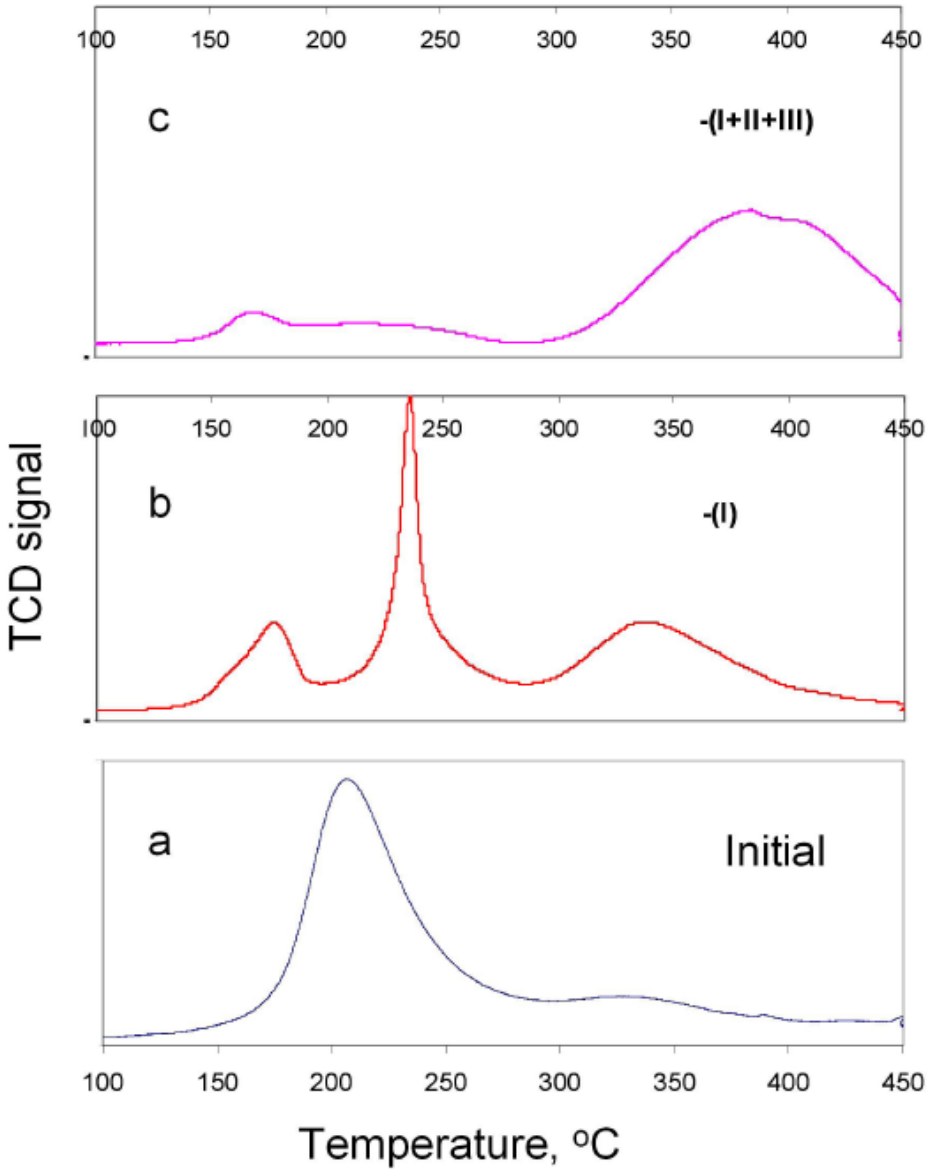

Figure 6. Profiles of the temperature-programmed reduction of platinum complexes: a – initial sample comprising all platinum species; b – sample after removal of readily desorbable complexes (platinum species corresponding to region I in the gradient elution profile (Figure 5) are removed), c – sample

comprising only nondesorbable platinum species (platinum species corresponding to regions I, II and III in the gradient elution profile (Figure 5) are removed).

Nonuniform interaction of adsorbed platinum species with the support surface may be caused both by the chemical composition of the complexes and by inhomogeneity of adsorption sites on the alumina surface. Hydroxo groups on the alumina surface are known to possess different acidic properties [75-90]. In particular, bridged OH groups are stronger Broensted acid sites in comparison with terminal hydroxyls. Most basic is the OH group bound to octa- and pentahedral aluminum. For example, IR spectroscopic study of the surface of some phase-homogeneous oxides [83] identified different OH groups and determined their amount. It was shown that more basic terminal OH groups, which are likely more capable of exchange with the metal complex ligands, constitute less than 30% of the total amount of the surface hydroxo groups.

If adsorption sites that can coordinatively bind metal complex are present on the oxide surface in a specified amount, the amount of strongly bound nondesorbable platinum complexes will also have a limiting value for a particular support. Indeed, variation of the platinum content from 0.1 to 2.5 wt.% showed [74] that in the low-percentage samples platinum is present mainly in nondesorbable coordinatively bound complexes. At that, the absolute amount of coordinatively bound platinum species increased with raising the total metal content of the sample to 1.0% and remained virtually constant upon further increase in the surface concentration of metal complexes (Figure 7). The plot corresponds to the Langmuir equation, the maximum amount of coordinatively fixed platinum in the sample being 0.6 wt.%.

In [41] it was shown that the content of coordinatively bound complexes can be increased effectively using the thermal hydrolysis of adsorbed chloride precursor, which not only accelerates the hydrolysis of chloro complexes, but also activates extra OH groups of the support. According to this method, complexes adsorbed on the alumina surface are held in an aqueous medium at temperatures above 100°C. In the experiments, titanium autoclaves with glass inserts were used at a solid to liquid phase ratio 1:10 under variation of temperature (120–190°C) and time (3–12 h) of hydrothermal treatment (HTT).

Changes in the composition of supported complexes caused by hydrolysis of adsorbed chloroplatinate were monitored by means of diffuse reflectance spectroscopy and EXAFS. Analysis of EXAFS spectra (Figure 8) revealed that hydrothermal treatment of the fixed complex made oxygen atoms prevailing in the first coordination sphere of platinum. Thus, the oxygen coordination number attained 4.5 at 150°C, and further temperature elevation did not increase it. According to the desorption experiments, variation of hydrothermal conditions can provide up to 80% of non-ion-exchangeable platinum species. Invariable chemical composition of the complexes in the temperature range of 150–190°C ($PtCl_{1,5}O_{4.5}$) as determined by EXAFS gave a constant proportion of different platinum species on the surface in the desorption experiment [41].

Meanwhile, as the HTT conditions were toughened, reflexes from the second and third coordination spheres of platinum increased in the EXAFS spectra of adsorbed complexes (Figure 8). This fact may indicate that along with increasing contribution of coordinative fixation of the metal complexes at a deeper hydrolysis, polycondensation becomes possible, which leads to the formation of polynuclear structures with the oxygen coordination number close to 5. The fundamental possibility of Pt-O(OH)-Pt bond formation was demonstrated in

the study of model platinum(IV) hydroxo complexes under HTT conditions with the use of spectral and XRD methods [91].

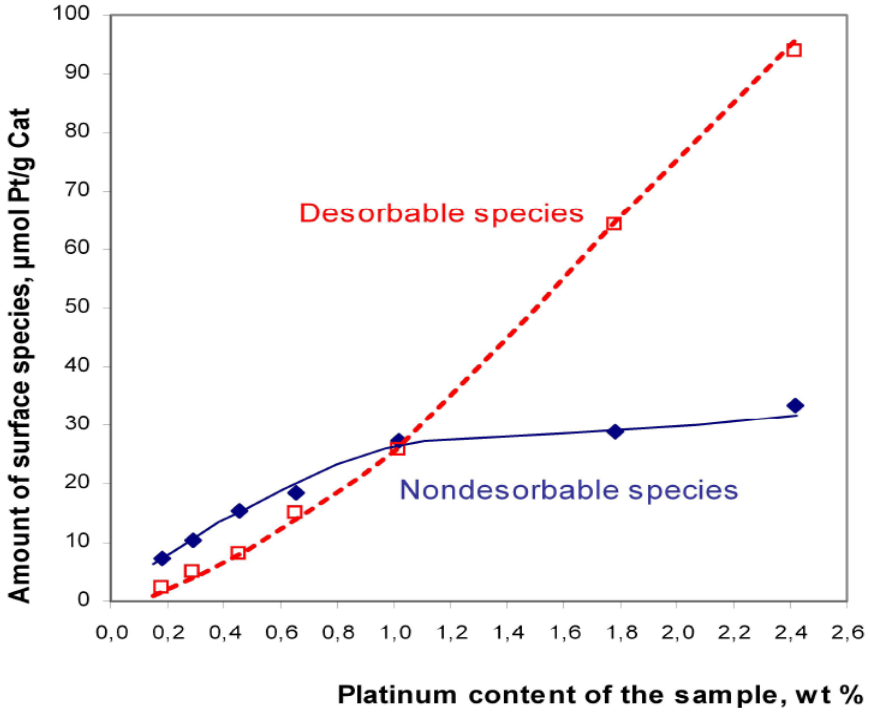

Figure 7. Platinum distribution between desorbable and nondesorbable species as a function of metal content of the sample [74].

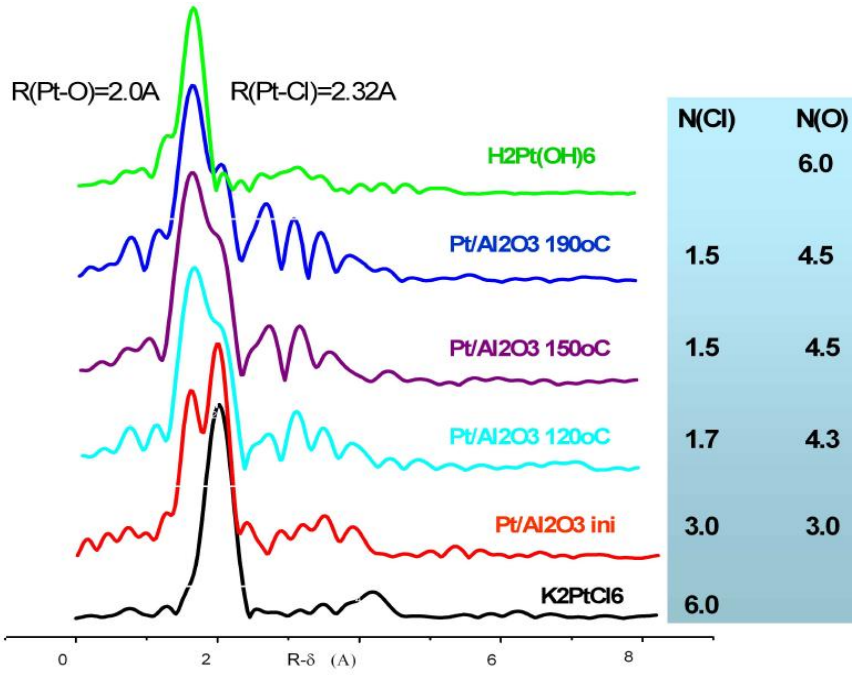

Figure 8. EXAFS data for H_2PtCl_6/Al_2O_3 (2% Pt) samples: initial, after hydrothermal treatment at 120, 150 and 190°C, and for the reference compounds $K_2[PtCl_6]$, $H_2[Pt(OH)_6]$ [41].

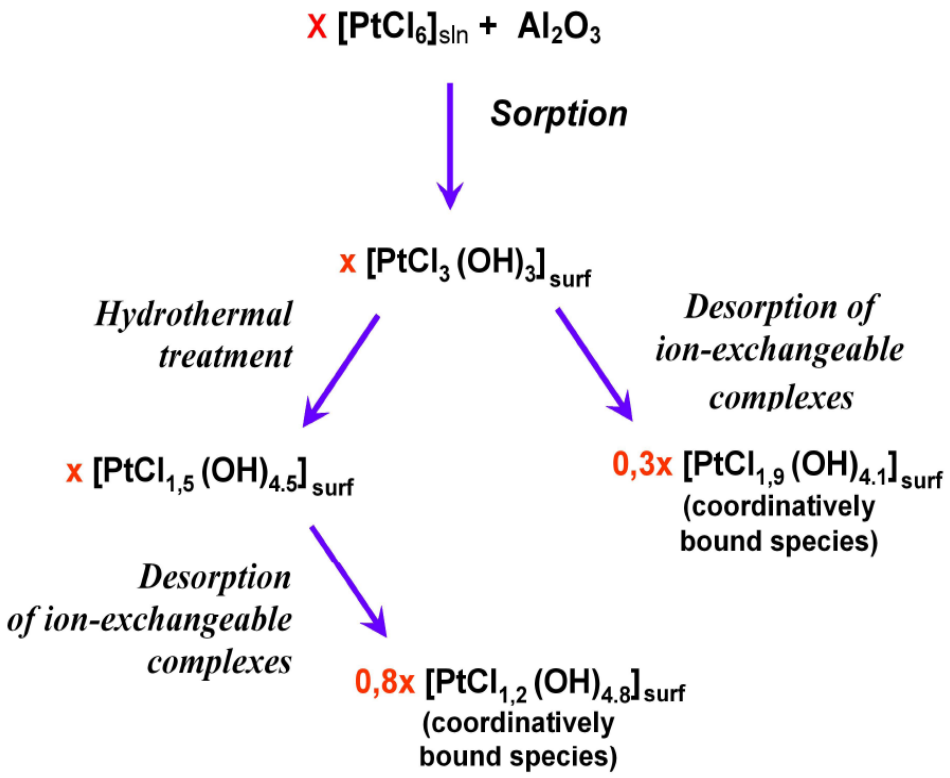

Figure 9. Transformations of the chloroplatinate ion upon its interaction with Al_2O_3 and subsequent hydrothermal and desorption treatment.

Thus, the prevailing content of coordinatively fixed platinum species in the samples can be attained not only by supporting very small amounts of metal complex and desorption of weakly bound species from the support surface, but also by introducing the procedure of hydrothermal treatment of adsorbed complexes (Figure 9). At that, nearly the entire supported precursor (up to 80%) uniformly interacts with the support.

SURFACE TRANSFORMATIONS OF ADSORBED COMPLEXES AT THE DRYING STAGE

Analysis of the works published in recent decades demonstrates that in multistage preparation of supported catalyst, in particular, the Pt/Al_2O_3 system, major attention is paid to the final procedures: calcination aimed at turning the precursors into oxide phase [92-96], and reduction of platinum ions leading to the formation of dispersed metal phase [97-101]. However, a necessary stage of catalyst drying is not considered in terms of possible chemical processes. Thus, the potential of molecular design of precursors at this stage is virtually neglected, and the role of chemical composition, structure, nature of metal complex binding

to the support at the stages preceding high-temperature treatment in the formation of the finished catalyst features is ignored.

Even in the present-day publications, drying of samples with the supported precursor compound in the temperature range of 25–200°C [102] is often considered only as a procedure of solvent removal from the pores of support. The drying stage seems to be essential only for preparation of catalyst with the weak precursor – support interaction. In this case, removal of solvent upon drying provides transport of the active metal compounds to evaporation surface, i.e., to the pore entrance and external surface of the grain. This may coarsen the supported metal grains and give nonuniform grain size distribution [100].

Only a few studies demonstrate that this stage provides further transformation of platinum complexes adsorbed on the oxide surface. Shelimov et al. [65-66, 103], using EXAFS and ^{195}Pt NMR spectroscopy, revealed that upon drying (20°C) of high-percentage model samples of $[PtCl_6]^{2-}/Al_2O_3$, two chloride ligands in chloroplatinate adsorbed on the alumina surface were substituted by two OH groups of the support. The formation of such inner-sphere complexes resulted in disappearance of NMR signal due to increased anisotropy of the chemical shift at a strong distortion in octahedral symmetry of the platinum complexes. An increase of the drying temperature to 90°C accelerated this process, which is regarded by the authors as 'thermoactivated reaction of the ligand substitution'. Thus, results of these works unambiguously point to chemical transformation of the fixed complexes upon drying. However, processes occurring at this stage are described on a qualitative level, and individual chemical reactions are merely postulated.

In [104], main attention is focused on the transformations of platinum complexes adsorbed on the oxide surface upon drying at 25 and 120°C; the role of chemical processes at this stage in the formation of properties of the catalyst metal sites is also elucidated. Subjects of investigation are the platinum(IV) complexes chemisorbed on the γ-Al_2O_3 surface upon interaction of alumina with the aqueous solution of H_2PtCl_6. The concentration of platinum is 0.3 wt.%, which corresponds to the platinum content of industrial reforming catalysts. After careful washing for removal of nonchemisorbed components of solution from the pore space of the support, the samples were dried at 25±1°C and natural lighting for different time. A sample dried to looseness for 2 h at room temperature in the dark was taken as the parent sample (in the plots, drying time of 0 h). The samples obtained at different drying time were studied by diffuse reflectance spectroscopy, ^{195}Pt NMR, gradient elution, and temperature-programmed reduction.

Upon contacting the adsorbed chloroplatinate with alumina, the extent of hydrolysis of the complex increased with the contact time: absorption intensity decreased in the region of 38000 cm^{-1} corresponding to Cl $\rightarrow$ Pt charge transfer, and the charge transfer band was shifted to high frequencies. However, after 50 h drying, changes in the composition of the complex became less pronounced (Figure 10a). Quantitative data obtained by gradient elution indicate that changes in the proportion of desorbable and nondesorbable species as well as changes in the chemical composition of the complexes were most pronounced over the first hour of drying and did not appear after 50 h. Thus, in the freshly prepared samples (dried at natural lighting for 0 and 1 h), platinum was present mainly in desorbable complexes, whereas the fraction of nondesorbable species was 10-30%. On completion of the drying process, the fraction of nondesorbable platinum stabilized at 60% (Figure 10b). Probably, moisture removal initiates a transition from the outer-sphere complexes, which are held by

electrostatic forces, to the inner-sphere complexes coordinatively bound to the surface. This inference is supported by the ^{195}Pt NMR MAS study of adsorbed complexes [104].

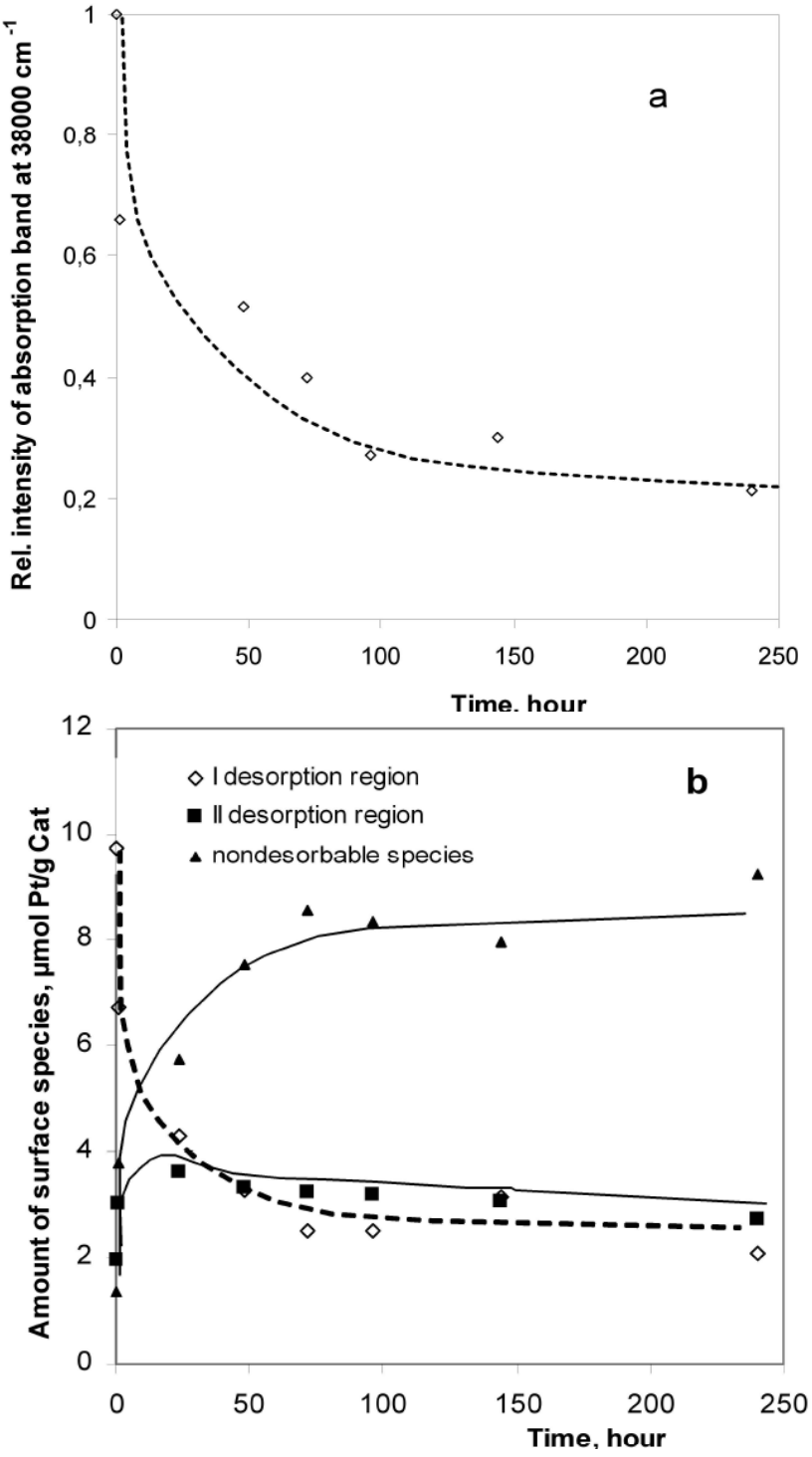

Figure 10. Effect of the drying time at 25°C on the chemical composition and proportion of desorbable and nondesorbable platinum species: a) evolution of the absorption band in the region of 37500 cm^{-1}

corresponding to charge transfer Cl → Pt.; b) changes in the proportion of desorbable and nondesorbable complexes versus drying time. In each sample, platinum content was 0.3 wt.%.

The employed method does not allow studying the samples with low concentration of supported precursor; so, the authors had to prepare samples of chemisorbed platinum complexes with the metal content of 4.5%, which corresponds to the limiting sorption capacity of the support. According to NMR spectra (Figure 11a), weak electrostatic interaction of platinum(IV) complexes with the support surface takes place in a freshly dried sample without noticeable distortions of their geometry [36].

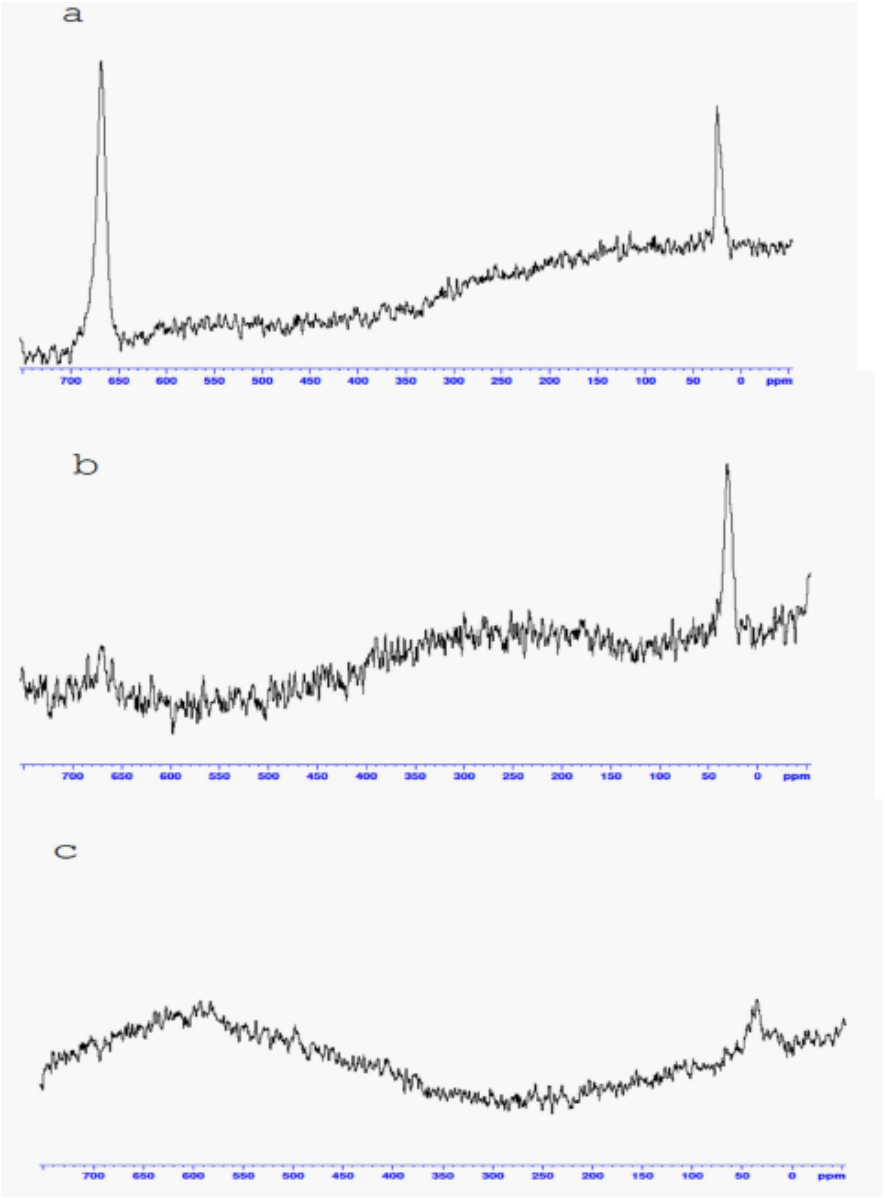

Figure 11. NMR ^{195}Pt MAS data for platinum complexes adsorbed on γ-Al_2O_3: a – freshly dried sample, b – drying of sample (a) at natural lighting for 2 h, drying of sample (a) in the light for 6 h. The

platinum content was 4.5%. ^{195}Pt NMR spectra of the solid samples were obtained on an Avance^{III} 400 spectrometer (Bruker) with a SB4 multiphase detector. Magic angle spinning frequency 10^4 Hz, $H_2[PtCl_6]$ standard.

The adsorbed platinum species are represented by chloride $[PtCl_6]^{2-}$ (10 ppm) and monosubstituted chloro-hydroxo complexes $[PtCl_5(OH)]^{2-}$ (660 ppm). Further drying of the sample at natural lighting (Figure 11b) strongly decreases the intensity of the latter signal, which confirms that hydrolyzed platinum species are capable of a more tight coordinative interaction. A more prolonged drying is accompanied by substantial hydrolysis of the adsorbed complexes, which increases the fraction of coordinatively bound complexes and hence results in virtually complete vanishing of NMR signals (Figure 11c).

Effect of the chemical composition of adsorbed complex and especially the nature of its binding to the surface was clearly seen upon temperature-programmed reduction (TPR) of the samples. In the case of freshly dried sample (1 h drying), with the content of platinum species in different desorption regions and in nondesorbable complexes equal to 50%, 22% and 28%, respectively (Figure 10b), three reduction region were observed in the TPR profile (Figure 12).

A considerable fraction of hydrogen (about 50%) was adsorbed in the low-temperature region with a maximum rate of adsorption at 80°C. Besides, TPR peaks were obtained at 200°C and in the region of higher temperatures, at 350°C. Therefore, a rare case of independent reduction of different platinum species was observed. When the proportion of platinum species was close to equilibrium (50 h drying), the low-temperature peak of hydrogen absorption significantly decreased, and main region of hydrogen absorption corresponded to the temperature range 150-300°C with a maximum rate at 210°C.

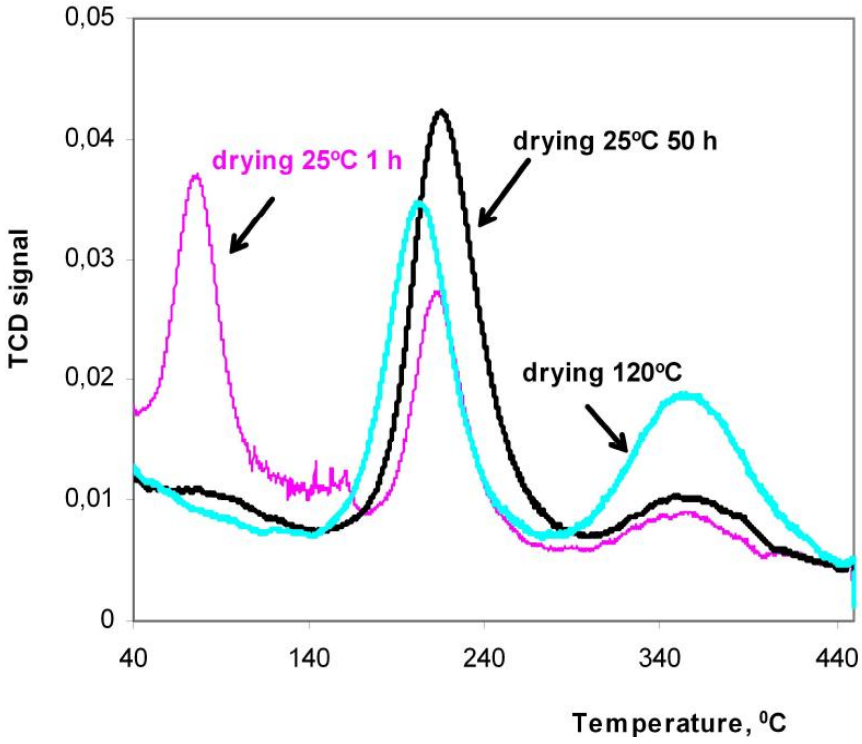

Figure 12. TPR profiles of platinum complexes for samples 2-01 and 4-48 differing in the drying time (1 and 50 h at 25°C) and temperature (25 and 120°C). C(Pt) = 0.3%.

Table 2. Chemical adsorption data for 0.3% Pt/γ-Al_2O_3. Dispersion was measured after sample reduction by hydrogen at 450°C

Sample	TPR		$D(H_2)$, %	D(CO), %
	μmol/g	$\sum H_2$/Me		
2-01	35.1	2.3	34	25
4-48	42.3	2.8	85	68
2-01, drying at 120°C, 6 h	50.5	2.8	86	56
2-01, calcination at 400°C, 3 h	31.5	1.8	85	67

The amount of difficultly reducible platinum species (at a temperature above 300°C) remained virtually unchanged for both samples. The obtained results provide a reliable evidence that reduction conditions are determined by the nature of binding and the strength of metal complex interaction with the support. These factors determine also the dispersity of platinum particles being formed (Table 2). Dispersity of supported platinum in these samples upon reduction in hydrogen at 450°C was estimated by the pulse chemisorption of hydrogen and carbon dioxide. The presence of readily desorbable complexes fixed via the ion-exchange mechanism led to formation of more coarse particles, whereas measures for tightening the interaction of metal complexes with the surface groups of support, even at increased temperature of reduction, facilitate higher dispersity of supported metal particles. This opens a way for obtaining the highly dispersed platinum without stages of high-temperature (120, 400°C) oxidative treatment (Table 2).

As shown by diffuse reflectance spectroscopy experiments, when samples predried at 25°C (for 50 h) were treated at the elevated temperature of 120°C, this produced no changes in the chemical composition of platinum complexes [104]. However, effect of the drying temperature showed up in the dynamics of platinum reduction. According to temperature-programmed reduction data (Figure 12), the elevated drying temperature decreased hydrogen adsorption at 200°C and simultaneously increased the adsorption at 350°C. The growing fraction of difficultly reducible platinum species under heat treatment of the adsorbed complex at 120°C may be due to increased probability of the multisite coordinative fixation of precursor. Probably, the elevated temperature activates additional, less basic OH groups of the alumina surface, and gets them involved in multisite coordinative binding of the fixed octahedral Pt(IV) complexes. Besides, such conditions make possible the condensation of hydrolyzed platinum species with the formation of polynuclear hydroxocomplexes, which, as shown in our earlier study [91], are also characterized by a higher reduction temperature.

EFFECT OF PRECURSOR NATURE AND ITS BINDING TO SUPPORT ON THE PROPERTIES OF THE FINISHED CATALYST ACTIVE SURFACE

In the concluding part of review, it seems reasonable to return to the question about role of our knowledge concerning the composition and structure of precursor and the nature of its

interaction with the support: how useful is this knowledge in deliberate formation of the adsorption and catalytic properties of supported catalysts. An efficient catalyst can be obtained if the active metal particles are optimally distributed over the support surface and have the controllable composition, size and structure. The intermediate position of supported nanoparticles between bulky metal and individual atom predetermines a deviation of their physicochemical properties from those of bulky metals, on one hand, and from the properties of isolated atoms, on the other. In the process of catalyst development, most interesting are changes in the surface structure and electronic features of metal nanoparticles, because these characteristics determine the specificity of interaction between reactants and the active component surface, the nature and reactivity of adsorbed particles and, finally, the activity and selectivity of nanosystems in heterogeneous catalysis.

First attempts to relate the rate of catalytic reaction with the particle size of active component were made in the late 1930s by N.I. Kobozev [105]. In the early 1950s, G.K. Boreskov formulated the rule stating that the specific catalytic activities (SCA) of substances with the same chemical composition are nearly equal [106, 107]. Later, reactions obeying this rule were called structure-insensitive by M. Boudart et al. [108, 109]. Further investigation of the particle size effect on the catalytic activity of metals [110-113] showed that all metal-catalyzed reactions can be divided into four main groups with respect to SCA: 1) SCA weakly depends on the particle size of supported metal (structure-insensitive reactions); 2) SCA diminishes as the particle size decreases (negative size effect); 3) SCA increases as the particle size decreases (positive size effect); 4) a maximum SCA is shown by intermediate size particles. Since the size of supported nanoparticles of the active component may affect the relative rates of individual stages in multi-route catalytic reactions, this will change the formation selectivity of some products. Both positive and negative effects were revealed; in some cases, selectivity happened to be independent of the particle size [114-116]. A considerable increase in selectivity toward commercially important products at decreasing particle size was observed in [117, 118]. For example, platinum clusters of the zeolite provided nearly 100% selectivity of n-hexane conversion to benzene [117]. In the catalytic system Au/SiO_2, gold nanoparticles of size 2-4 nm catalyzed propylene epoxidation, and particles of a smaller size — its hydrogenation [119, 120].

Size of supported metal particles largely depends on the strength of interaction between precursor compound and support surface at the stage of supporting; the strength can be controlled by variation of the nature of metal complex and the support. A minimum interaction occurs in the synthesis of so-called ‘impregnation’ catalysts, where a precursor solution is localized in the pore volume without sorption interaction with the support. In this case, metal complexes weakly bound to the support surface are capable of diffusion over the surface at heat activation stages, which leads to the formation of more coarse metal particles.

Variation of the catalyst properties with the use of different supports and precursors was considered in [121], where Pd/SiO_2 catalysts were prepared from various palladium compounds and the strength of metal complex – support interaction was monitored by TPR. The temperature of palladium reduction was shown to rise with the strength of precursor – support interaction increasing in a series H_2PdCl_4 (25°C) < $Pd(C_3H_5)_2$ (100°C) < $Pd(NH_3)_4(OH)_2$ (180°C) = $Pd(NH_3)_4Cl_2$ (190°C), which increased the metal dispersity and decreased the hydrogenation activity of supported palladium. A great body of experimental data comparing the activities of Pt/Al_2O_3 catalysts prepared from different platinum

compounds ($H_2PtCl_6 \cdot 6H_2O$, $Pt(NO_2)_2(NH_3)_2$, $[Pt(NH_3)_4]Cl_2$) is presented in [122] for the oxidation of propane and CO, hydrogenation of ethylene and naphthalene, dehydrochlorination of 1,1,1-trichloroethane, and hydrocracking of hexane. A review paper [62] reports a substantial increase of the catalyst activity in catalytic reactions of different types when going from 'impregnation' to 'sorption' catalysts.

Within the chemisorption interaction, the strength of metal complex fixation can be varied effectively by the introduction of special competing ions on the support surface or in the solution of precursor compound [54, 123, 124]; note that such a competitor may be represented also by the solvent molecules [125]. The use of chloroplatinic acid dissolved in water and organic solvents upon its fixation on alumina and carbon supports demonstrated the effect of solvent on the distribution of adsorbed platinum complexes, their resistance to sintering and activity in hydrogenation of 1-octene and nitrobenzene [125].

Rather scarce are the works where data on the molecular structure of adsorbed precursor and nature of its binding with the support are used to synthesize catalysts with optimal surface characteristics and high activity. A rare example is the study [126] showing the effect of pH of the impregnating solution on the interaction between MoO_4^{2-} anion and TiO_2 support. It was found that, depending on the solution pH, precursor can be fixed as mono- or disubstituted species [127]. The latter are more resistant to sintering upon calcination and form, according to XPS and electron spectroscopy data, more fine MoO_3 particles on the support surface. As a result, with the same amount of supported metal, the catalyst provided a twofold higher activity in selective catalytic reduction of NO.

Variation of precipitation conditions for palladium complexes on the surface of carbon material Sibunit[1] was examined in [128]; as the $NaOH/[PdCl_4]^{2-}$ molar ratio was raised from 0 to 1.2, this increased the fraction of palladium fixed in polyhydroxo complexes. A comprehensive study of the structure of polynuclear complexes and the mechanism of their adsorption by carbon materials is presented in [128, 129]. It was revealed that palladium reduction made such catalysts more active toward hydrogenation of phenylacetylene, styrene, nitrobenzene, cyclohexene as compared to catalysts prepared from mononuclear complexes.

Changes in the nature of precursor binding to the support when going from coordinatively fixed inner-sphere complexes to ion-exchangeable outer-sphere species can affect the catalytic activity of supported phase in the finished $MoO_3/\gamma\text{-}Al_2O_3$ catalyst [130]. Thus, fixation of molybdate anion at pH = 6.3 on the $\gamma\text{-}Al_2O_3$ surface leads to inner-sphere complexes [131], whereas a lower pH of the impregnating solution causes the preferential formation of polymolybdates capable of fixation to the support surface by electrostatic forces and/or by hydrogen bonds. Upon calcination, such more weakly bound polymolybdates formed a dispersed phase, which is characterized by higher reducibility and concentration of octahedral oxidized species that can readily be sulfided. Being used in catalyst preparation, they provided a higher catalytic activity in thiophene hydrodesulfurization [130].

The above examples demonstrate unambiguously that the structure of precursor compound and the nature of its interaction with the support surface at the initial stage of synthesis can have a pronounced effect on the surface characteristics and activity of supported catalyst even in the case of multistage process of catalyst preparation. According to our studies, this conclusion holds true for the catalytic system Pt/Al_2O_3. When going from

[1] Carbon-carbonaceous material Sibunit was developed at the Boreskov Institute of Catalysis SB RAS and patented in the USA; the trademark is registered in Russia and abroad.

chloride precursor in the 'impregnation' $[PtCl_6]/SiO_2$ sample to hydrolyzed coordinatively bound $[PtCl_{6-x}(OH)_x]/Al_2O_3$ species, platinum reduction became hindered due to a stronger interaction of adsorbed complexes with the support. Samples of the adsorbed complexes after their thermal hydrolysis under different conditions were examined by means of temperature-programmed reduction (Figure 13) [132].

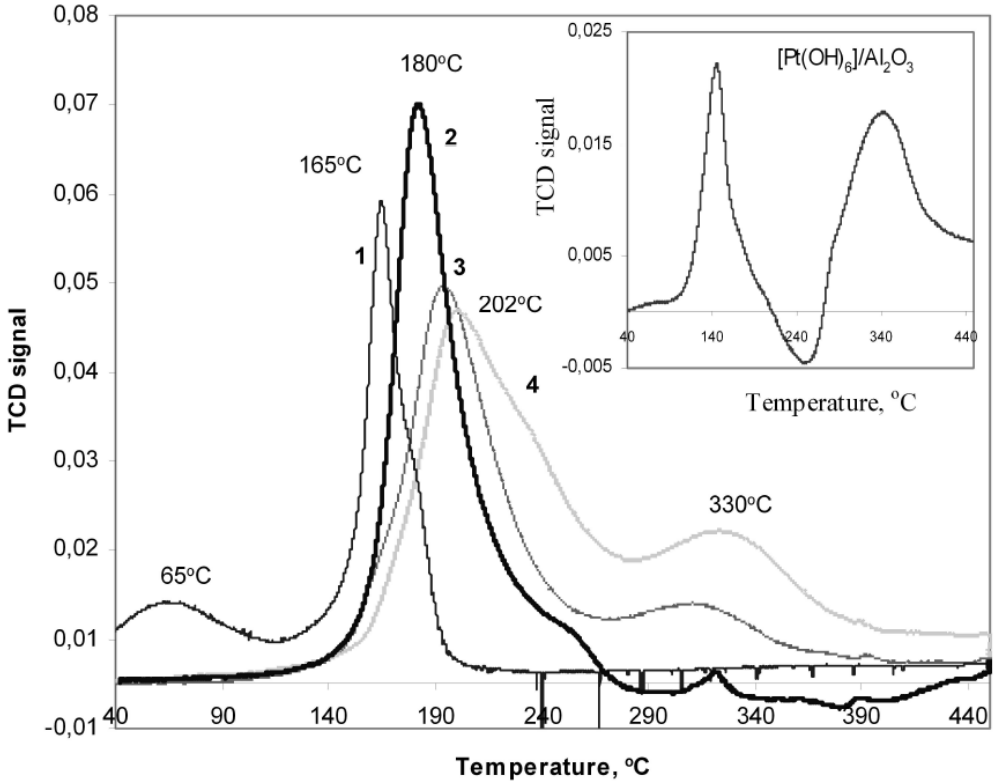

Figure 13. TPR profiles of the samples: 1) $[PtCl_6]/SiO_2$ (minimum interaction of the metal complex with support); 2–4) $[PtCl_6]/Al_2O_3$ initial, dried at 25°C for 48 h (2), and subjected to thermal hydrolysis at 120 (3) and 150°C (4) for 6 h. Insert: TPR profile of the $[Pt(OH)_6]/Al_2O_3$ sample. In each sample, platinum content was 2 wt.% [132].

As the extent of chloro complexes hydrolysis increased and their coordinative interaction with the surface hydroxo groups of alumina became more strong, the maximum in hydrogen adsorption curves shifted monotonically to the high-temperature region with simultaneous increase in the fraction of metal complexes which reduction requires temperatures above 300°C [132]. The contribution of these high-temperature species is even more pronounced in the case of complete chloroplatinate hydrolysis product, platinum(IV) hydroxo complex $H_2[Pt(OH)_6]$ adsorbed on the alumina surface (Figure 13, an insert). However, platinum species reducible at a lower temperature are also present here; hence, essential is not only the chemical composition of adsorbed precursor, but also the nature of its interaction with the support.

To assess the effect of thermal hydrolysis of adsorbed complexes on the size of supported platinum particles in the finished catalyst, platinum dispersity (the fraction of surface atoms in

platinum particles) was investigated [104]. Dispersity was measured by selective chemisorption of H_2 and CO gases [133-136]. Prior to chemisorption measurements, samples of supported complexes were carefully dried (25°C, 48 h) and reduced in flowing hydrogen at 450°C. At the platinum concentration ranging from 0.5 to 2.0 wt.%, dispersity of platinum was close to the limiting value and retained this value in hydrothermal treatment under mild conditions (100–150°C, 3–6 h). However, when the temperature rose to 190°C and/or the treatment time increased to 12 h, a decrease in dispersity from 0.92–0.97 to 0.57–0.75 was observed [104]. Probably, more coarse platinum particles form due to reduction of polynuclear complexes, which formation upon hydrothermal treatment was suggested in our earlier works.

Indeed, even at close values of supported platinum concentration and dispersity, active sites that formed from the chloride and hydrolyzed coordinatively bound precursors differ in their adsorption and catalytic properties. In particular, the reduced platinum species obtained from a hydrolyzed precursor are characterized by a stronger adsorption of hydrogen molecules [104]. In the spectra of temperature-programmed desorption of hydrogen, a desorption maximum shifted to higher temperatures, 90–150°C.

Upon reduction in hydrogen at 450°C, the Pt/Al_2O_3 catalysts synthesized from chloride and hydrolyzed precursors were tested in a series of hydrocarbon transformation reactions. As a model reaction we used benzene hydrogenation (50–100°C), which runs only on the catalyst metal sites to yield cyclohexane as a single product without noticeable carbonization of the surface. It was found that in the both type catalysts (differing in the nature of metal complex – support interaction), active sites involved in hydrogenation reaction were of the same nature. At the identical form of kinetic curves over the entire range of conversion, zero order reaction with respect to benzene was observed in the region of high partial pressures, and all studied samples had close E_{act} values equal to 14-16 kcal/mol. At the same time, a comparison of specific catalytic activities revealed that amount of platinum atoms involved in benzene hydrogenation is much smaller for the samples prepared from hydrolyzed forms of precursor [104]. Thus, the fraction of surface atoms active toward hydrogenation decreased to 40 and 20% for the samples with platinum content 1.0 and 0.5%, respectively.

Therefore, when hydrolyzed platinum complexes capable of coordinative interaction with the oxide support are used as the active metal precursors, this leads not only to platinum sites having the hydrogenation activity, but also to specific platinum species which are inactive in this low-temperature reaction, but accessible to CO and H_2 adsorption.

Meanwhile, catalysts prepared from coordinatively bound metal complexes demonstrate considerable advantages (over conventional catalysts obtained from precursor with a less uniform composition) in the high-temperature reactions of hydrocarbon transformation. They have a higher selectivity in alkane dehydrocyclization and a greater activity toward cyclohexane dehydrogenation accompanied by a decreased activity in hydrogenolysis of C–C bonds [39, 137]. As an example, Figure 14 shows the results of comparative testing of such catalysts in the transformation of n-heptane at 400–520°C. At a close aromatization activity (Figure 14a), selectivity for this target reaction (Figure 14b) is noticeably higher on the sample prepared with hydrolyzed platinum complexes as precursors.

Studies of platinum catalysts performed at the IHP SB RAS [138-143] demonstrate that the indicated features are typical of the catalysts where a considerable part of supported platinum is present as ionic species.

According to [144-146], the low-percentage alumina–platinum catalysts may comprise platinum in the state different from that of metallic Pt^o.

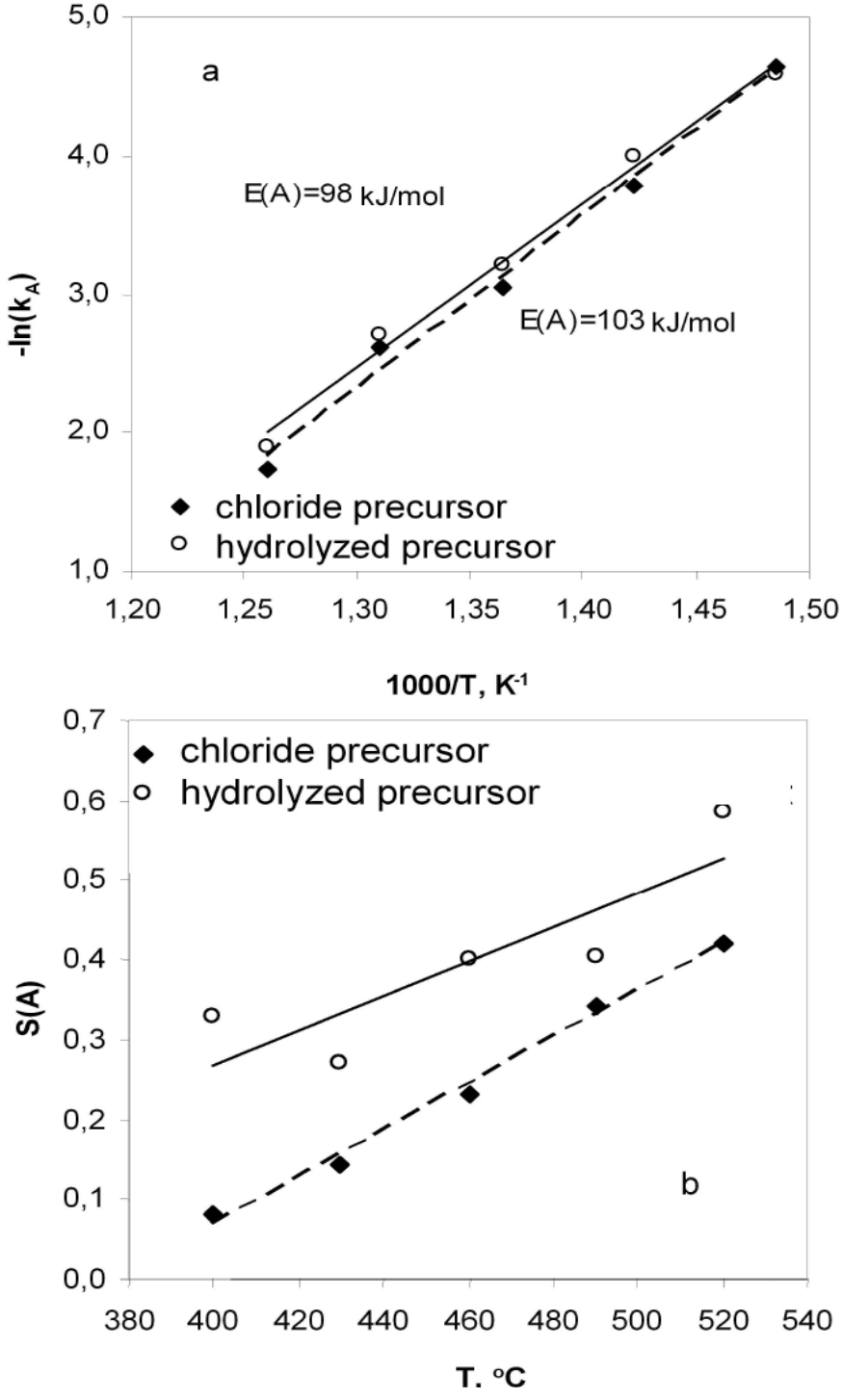

Figure 14. The 1.0%Pt/Al_2O_3 samples, initial and after HTT at 150°C for 6 h, in dehydrocyclization of n-heptane: a) aromatization constant versus the reaction temperature; b) aromatization selectivity versus the reaction temperature. Pretreatment conditions: T_{H2} = 450°C, 3 h; reaction conditions: 10 atm, mass feed rate of n-heptane 15 h^{-1}, molar ratio H_2/C_7 = 5.

Later, in the development and investigation of catalysts for gasoline reforming [138-143, 147], it was found that ionic platinum species (Pt^{σ}), which are inactive in low-temperature hydrogenation, provide catalyst resistance to coke and sulfur deactivation in the reaction medium of high-temperature reforming as well as selective occurrence of the target reaction — dehydrocyclization of paraffin hydrocarbons. In recent decades, the development of catalysts for gasoline reforming was aimed mainly on devising such synthesis techniques that would increase the fraction of highly dispersed platinum retaining its ionic state under high-temperature pretreatments and reactions.

To investigate the electronic state of supported platinum obtained from coordinatively fixed precursor, photoelectronic spectra ($Pt3d_{5/2}$, Ag L_{α}) of the samples synthesized by conventional scheme and using the thermal hydrolysis stage were compared [104]. Indeed, for the sample synthesized from hydrolyzed precursor (120°C, 3 h), the platinum line shifted toward higher energies (Figure 15). Deconvolution of photoelectronic spectra allowed identifying in 1%Pt/Al_2O_3 samples reduced in hydrogen at 450°C both platinum, which valent state is close to that of metallic Pt^o (E_b = 2121.8 eV), and charged metal species with E_b = 2123.5 and 2124.4 eV [148]. It should be noted that the fraction of platinum in the oxidized state close to Pt^{2+} is much greater in the sample obtained from hydrolyzed and coordinatively bound precursor as compared to the sample prepared without thermal hydrolysis stage. This effect may be due to partially retained binding of platinum with the surface groups of support.

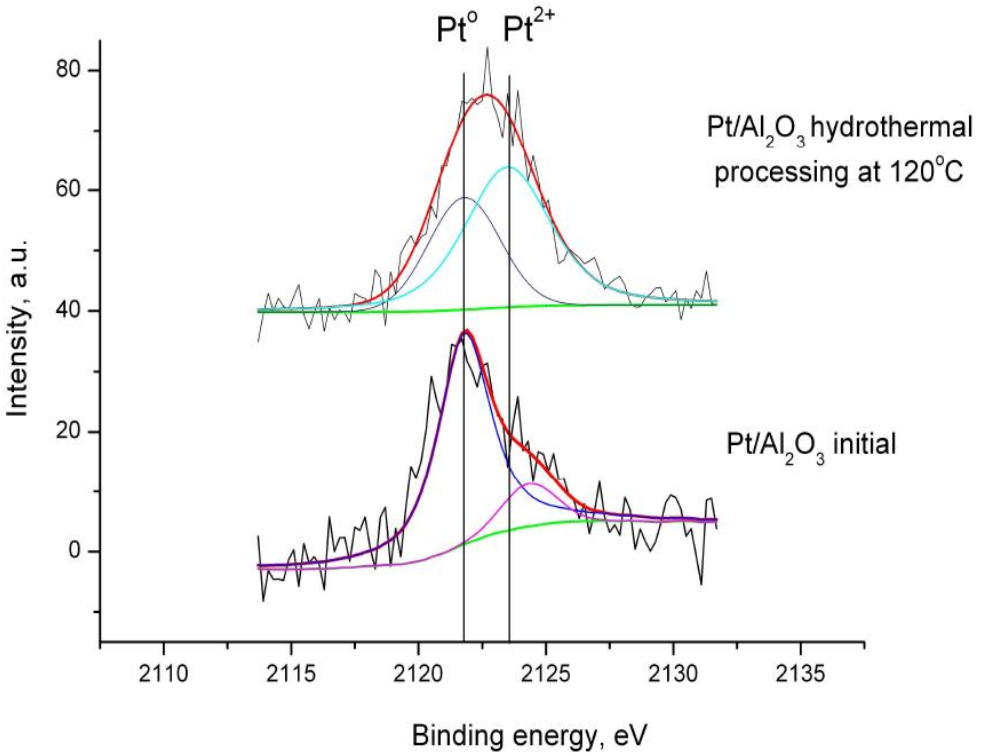

Figure 15. Effect of the extent of hydrolysis of adsorbed platinum(IV) chloro complex on the state of platinum in reduced Pt/Al_2O_3 samples. C(Pt) = 1 wt.%. T_{H2} = 450°C (2 h) [104].

Therefore, changes in the nature of metal complex – support interaction at the stage of precursor adsorption can affect the electronic state of supported platinum in Pt/Al_2O_3 catalyst. Specifically, a transition to coordinative fixation with the formation of inner-sphere platinum complexes can increase the fraction of ionic platinum species Pt^{2+} in the finished catalyst. This approach is promising for the development of highly selective catalysts for dehydrocyclization of n-alkanes without additional modification of support and introduction of polymetallic compositions.

CONCLUSION

This review presents an analysis of studies developing the ideology of molecular design, with the synthesis of alumina-based platinum systems used as an example. The studies were aimed at revealing the regularities that could provide a deep insight into the processes of active complex formation, with special emphasis on the transformation of metal complex precursor at the early stages of synthesis.

Thus, changes in the ligand environment of platinum can be controlled in a homogeneous medium by exposure to light, temperature, introduction of Pd(II) complex as a catalytic additive to produce precursor of a specified composition prior to its adsorption. A convenient tool for studying the interaction of adsorbed metal complexes with the support is represented by simple desorption techniques that use the competitive sorption of specially chosen anions or variation in pH of the oxide surface for quantitative differentiation between the adsorbed species according to the nature of their binding with the support surface.

Study of the composition and amount of metal complexes in eluate solutions and on the alumina surface before and after desorption showed that two mechanisms of the metal complex – support interaction can occur simultaneously: electrostatic adsorption with platinum fixation as outer-sphere complexes and coordination binding with the formation of inner-sphere platinum complexes (Figure 16).

At least three forms of precursors differing in the composition of metal coordination sphere and strength of their binding to the support can be distinguished:

1) readily desorbable ion-exchanged species with a general formula $[PtCl_5(OH)]^{2-}$, which are held on the support by electrostatic forces;
2) strongly bound desorbable species characterized by a greater extent of hydrolysis, probably, of composition $[PtCl_4(OH)_2]^{2-}$;
3) nondesorbable deeply hydrolyzed complexes with a general formula $[PtCl_2(OH)_4]^{2-}$, which are tightly held on the support by several coordination bonds.

In the process of catalyst formation, the transformation of metal complexes consists mainly in increasing the extent of their hydrolysis according to the scheme: from ion-exchanged complexes (1) to coordinatively bound ones (3) via the intermediate species. However, hydrolysis by itself is a necessary but insufficient condition for understanding a real scheme of chloroplatinate transformation. It is of key importance that the hydrolysis involves

not only the outer-sphere molecules of water, but also the structural OH groups of alumina, which should be considered here as a reagent. Hence, electrostatic interaction at the impregnation and especially drying stages is replaced mainly by coordinative binding with OH groups of the support. The tendency of precursors to form, probably, a thermodynamically favorable coordinatively bound chelate structures is the driving force of their transformation. The process terminates at specific sites of the support with the formation of surface species $[PtCl_2(OH)_4]$ via substitution of the metal complex ligands by four OH groups of the support**.** Full usage of such sites is provided by introducing more than 1 wt.% platinum into the catalyst. In this case, the limiting value for coordinatively fixed platinum is 0.6 wt.%, and dependence of its content on the total concentration of supported metal obeys the Langmuir isotherm equation.

The catalyst drying, which is conventionally regarded as a physical process of water removal, actually stimulates the substitution reactions of inner-sphere ligands by the surface OH groups of support with the formation of tightly bound hydrolyzed precursor species and, probably, their subsequent polycondensation. These hidden processes are uncontrollable at the drying stage; nevertheless, they are more essential for the formation of active surface than the process of free water removal indicated in the name of this stage.

I. 'Electrostatic' adsorption (platinum fixation as 'outer-sphere' complexes)

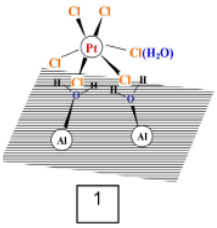

Composition of complexes on the surface: $[PtCl_5(H_2O)]^-$ and/or $[PtCl_5(OH)]^{2-}$

Adsorption: fixation is accompanied by increasing pH and a minor increase in the concentration of free chloride ions in the impregnating solution

Properties of the fixed complexes: can be removed from the surface upon competitive sorption of anions and 'recharging' of the surface; platinum reduction at 25–100°C, which is typical of the reduction of bulky complexes; formation of low dispersed platinum particles

Hydrolysis of complexes on the surface under the action of light and temperature (aging, drying, HTT)

II. Coordinative binding (platinum fixation as 'inner-sphere' complexes)

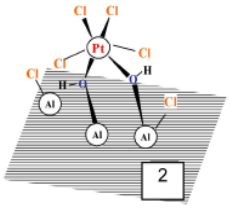

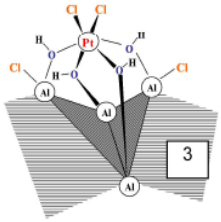

Composition of complexes on the surface: deeply hydrolyzed species with the oxygen coordination number up to 5

Adsorption: fixation during the ligand exchange with OH groups of the surface

Properties of the fixed complexes: desorption from the support surface at competitive sorption of anions and 'recharging' of the surface is hindered or absent; platinum reduction at T_{max} = 200°C (2) and T_{max} = 350°C for multisite adsorption (3); formation of highly dispersed platinum particles and ionic platinum species

Figure 16. Composition and properties of adsorbed platinum(IV) chloro complexes in the synthesis of Pt/Al_2O_3 catalyst.

It can be stated with confidence that, in contrast to commonly accepted ideas, the drying stage has the rich chemical contents for the catalysts obtained from metal complexes.

An efficient way for increasing the concentration of coordinatively bound complexes is the use of thermal hydrolysis of the adsorbed chloride precursor in the temperature range of 100–150°C: this may not only accelerate the hydrolysis of chloro complexes, but also activate the additional amount of OH groups of the support. Besides, along with increasing contribution of coordinative fixation of the metal complexes at a growing extent of their hydrolysis, the polycondensation process becomes possible, which causes the formation of polynuclear structures with the oxygen coordination number close to 5. The basic possibility of Pt-O(OH)-Pt bond formation was revealed when studying the model platinum(IV) hydroxo complexes upon hydrothermal treatment. Variation of the formation conditions of such oxide-like structures should be considered as a possibility of controlling the dispersed state of supported metal even at the stage of precursor fixation.

The predominant content of coordinatively fixed platinum species in the samples can be provided by introducing the procedure of hydrothermal treatment of adsorbed complexes and by desorption of less tightly bound species from the support surface. Catalysts for hydrocarbon transformation synthesized from such precursors have some specific catalytic properties distinguishing them from conventional catalysts obtained from precursors with a less uniform composition: high selectivity for dehydrocyclization of alkanes, an increased activity toward alkanes aromatization and cyclohexane dehydrogenation, and a decreased activity toward benzene hydrogenation and hydrogenolysis of C–C bonds. These features may be provided by a substantially greater fraction of ionic platinum species in the catalyst.

The revealed quantitative ratios of different precursor species at the early stages of catalyst preparation, the regularities of the active component formation depending on the type of precursor binding to the support, chemical composition and molecular structure of precursor can be used for deliberate formation of the fundamental characteristics of the active surface: dispersity, state of the metal and strength of the interaction with support. Therefore, generalizations presented in this work are a new step from empirical approach to catalyst development toward the ideology of chemical design based on deep understanding of the structure of supported metal complex systems and the production technologies for a wide spectrum of hydrocarbon transformations.

REFERENCES

[1] Silva, R. P. *Oil and Gas J*. 2004, *102*, 58.
[2] Shiju, N.R.; Guliants, V.V. *Appl. Catal. A: General.* 2009, *356*, 1–17.
[3] Bukhtiyarov, V. I.; Slin'ko, M. G. *Russian Chem. Rev.* 2001, *70*, 147–159.
[4] Wilson, O. M.; Knecht, M. R.; Garcia-Martinez, J. C.; Crooks, R. M. *J. Am. Chem. Soc*. 2006, *128*, 4510–4511.
[5] Miolati, A.; Pendini, U. *Z. anorg. Chem*. 1903, *33*, 251–263.
[6] Schlesinger, H. I.; Palmateer, R. E. *J. Am. Chem. Soc.* 1930, *52*, 4316–4331.
[7] Pshenitsyn, N. K.; Ginzburg, S. I., *Izv. Sekts. Platiny Dr. Blagor. Met.* 1954, 214–228.

[8] Grinberg, A. A.; Shagisultanova, G. A. *Zh. Neorg. Khim*. 1960, *5*, 280–282.
[9] Grinberg, A. A.; Kukushkin, Yu. N. *Zh. Neorg. Khim*. 1961, *6*, 306–308.
[10] Grinberg, A. A.; Kukushkin, Yu. N. *Zh. Neorg. Khim*. 1961, *6*, 1084–1097.
[11] Kukushkin, Yu. N. *Zh. Neorg. Khim*. 1962, *7*, 7–10.
[12] Nikolaeva, N. M.; Ptitsyn, B. V.; Gorbacheva, I. I. *Zh. Neorg. Khim*. 1965, *10*, 1051–1057.
[13] Nikolaeva, N. M.; Ptitsyn, B. V.; Pastukhova, E. D. *Zh. Neorg. Khim*. 1965, *10*, 1058–1061.
[14] Shul'man, V. M.; Dubinskii, V. I. *Izv. Sib. Otd. Akad. Nauk, Ser. Khim*. 1966, *1*, 25–31.
[15] Nabivanets, B. I.; Kalabina, L. V.; Kudritskaya, L. N. *Zh. Neorg. Khim*. 1971, *16*, 3281–3284.
[16] Kalabina, L. V. *Ukr. Khim. Zh*. 1983, *4*, 342–345.
[17] Kukushkin, Yu. N. *Koord. Khim*. 1977, *3*, 1876–1884.
[18] Gröning, Ö.; Elding, L. I. *Inorg. Chem*. 1989, *28*, 3366–3372.
[19] Sillen, L. G.; Martell, A. E. *Stability Constants of Metal Ion Complexes:* Burlington House: London, 1971.
[20] Drougge, L.; Elding, L. I.; Gustafson, L. *Acta Chemica Scandinavica*. 1967, *21*, 1647–1658.
[21] Elding, L. I. *Inorg. Chim. Acta*. 1976, *20*, 65–69.
[22] Elding, L. I.; Olsson, L. F. *J. Phys. Chem*. 1978, *82*, 69–74.
[23] Appleton, T. G.; Berry, R. D.; Davis, C. A.; Yall, J. R.; Kimlin, H. A. *Inorg. Chem*. 1984, *23*, 3514–3521.
[24] Appleton, T. G.; Hall, J. R.; Ralph, S. P.; Thompson, C. S. M. *Inorg. Chem.* 1984, *23*, 3521–3525.
[25] Rich, R. L.; Taube, H. *J. Am. Chem. Soc.* 1954, *76*, 2608–2611.
[26] Dreyer, R.; Dreyer, I.; Rettig, D. *Zeitschrift für physikalische Chemie*. 1963, *224*, 199–206.
[27] Davidson, C. M.; Jameson, R. F. *Trans. Farafay Soc*. 1965, *61*, 2462–2467.
[28] Balashev, K. P.; Blinov, I. I.; Shagisultanova, G. A. *Zh. Neorg. Khim*. 1987, *32*, 2470–2474.
[29] Kovalenko, N. L.; Kozhukhovskaya, G. A.; Mal'chikov, G. D.; Grelovskaya, N. A. *Zh. Neorg. Khim*. 1981, *26*, 2172–2177.
[30] Swihart, D. L.; Mason, W. R. *Inorg. Chem*. 1970, *9*, 1749–1757.
[31] Cox, L. E.; Peters, D. G. *Inorg. Chem*. 1970, *9*, 1927–1930.
[32] Cox, L. E.; Peters, D. G.; Wehry, E. L. *J. Inorg. Nucl. Chem*. 1972, *34*, 297–305.
[33] Carr, C.; Goggin, P. L.; Goodfellow, R. J. *Inorg. Chimica Acta* 1984, *81*, L25–L26.
[34] Spieker, W. A.; Liy, J.; Miller, J. T.; Krop, A. J.; Regalbuto, J. R. *Appl. Catal. A* 2002, *232*, 219–235.
[35] Mang, T.; Breitscheidel, B.; Polanek, P.; Knozinger, H. *Appl. Catal. A*. 1993, *106*, 239–258.
[36] Shelimov, B.; Lambert, J.-F.; Che, M.; Didillon, B. *J. Am. Chem. Soc.* 1999, *121*, 545–556.
[37] Zolotov, Yu. A., Varshal, G. M., Ivanov, V. M., *Analiticheskaya khimiya metallov platinovoi gruppy (Analytical Chemistry of the Platinum Group)*: KomKniga: Moscow, 2005.

[38] Bel'skaya, O. B.; Karymova, R. Kh.; Kochubei, D. I.; Duplyakin, V. K. *Kinet. Katal*. 2008, *49*, 754–763 [*Kinet. Catal. (Engl. Transl.) 49*, 720].
[39] Bel'skaya, O. B.; Duplyakin, V. K. Ross. Khim. Zh. 2007, LI, 29–37.
[40] Buslaeva, T. M.; Umreiko, D. S.; Novitskii, G. G. *Khimiya i spektroskopiya galogenidov platinovykh metallov (Chemistry and Spectroscopy of Platinum MetalHalides)*: Universitetskoe: Minsk, 1990.
[41] Bel'skaya, O. B.; Karymova, R. Kh.; Kochubei, D. I.; Duplyakin, V. K. Kinet. Katal. 2008, 49, 764–772 [Kinet. Catal. (Engl. Transl.) 49, 720].
[42] Bel'skaya, O. B.; Gulyaeva, T. I.; Arbuzov, A. B.; Duplyakin, V. K.; Likholobov, V. A. Kinet. Katal. 2010, 51, 114–122 [Kinet. Catal. (Engl. Transl.) 51, 105–112].
[43] Shchukarev, S. A.; Lobaneva, O. A.; Ivanova, M. A.; Kononova, M. A. Vestn. Leningr. Gos. Univ., Fiz. Khim. 1961, 10, 152.
[44] Do, D. D. *Chem. Engin. Sci*. 1985, *40*, 1871–1880.
[45] Chu, P.; Peterson, E. E.; Radke, C. J. *J. Catal*. 1989, *117*, 52–70.
[46] Heise, F. J.; Schwarz, J. A. *J. Colloid Interface Sci*. 1985, *107*, 237–243.
[47] Heise, F. J.; Schwarz, J. A. *J. Colloid Interface Sci*. 1986, *113*, 55–61.
[48] Heise, F. J.; Schwarz, J. A. *J. Colloid Interface Sci*. 1988, *123*, 51–58.
[49] Brunelle, J.P. *Pure and Applied Chemistry* 1978, *50*, 1211–1229.
[50] Hao, X.; Spieker, W. A.; Regalbuto, J. R. *J. Colloid Interface Sci*. 2003, *267*, 259–264.
[51] Spieker, W. A.; Liu, J; Hao, X.; Miller, J. T.; Krop, A. J.; Regalbuto, J. R. *Appl. Catal. A*. 2003, *243*, 53–66.
[52] Regalbuto, J. R.; Schreier, M.; Hao, X.; Spieker, W. A.; Kim, J.-G.; Miller, J. T.; Kropf, A. J. *Stud. Sur. Sci. Catal*. 2002, *143*, 45–53.
[53] Spieker, W. A.; Regalbuto, J. R. *Chem. Eng. Sci*. 2001, *56*, 3491–3504.
[54] Spieker, W.; Regalbuto, J.; Rende, D.; Bricker, M.; Chen, Q. *Stud. Surf. Sci. Catal*. 2000, *130A*, 203–208.
[55] Regalbuto, J. R.; Navada, A;. Shadid, S.; Bricker, M. L.; Chen, Q. *J. Catal*. 1999, *184*, 335–348.
[56] Regalbuto, J. R.; Agashe, K.; Navada, A.; Bricker, M. L.; Chen, Q. *Stud. Surf. Sci. Catal.* 1998, *118*, 147–156.
[57] Agashe, K.; Regalbuto, J. R. *J. Colloid Interface Sci*. 1997, *185*, 174–189.
[58] Santhanam, N.; Conforti, T. A.; Spieker, W.; Regalbuto, J. R. *Catal. Today* 1994, *21*, 141–156.
[59] Shah, A.; Regalbuto, J. R. *Langmuir* 1994, *10*, 500–504.
[60] Hao, X.; Quach, L.; Korah, J.; Spieker, W. A.; Regalbuto, J. R. *J. Molec. Catal. A: Chemica.* 2004, *219*, 97–107.
[61] Regalbuto, J. R.; Schreier, M.; Hao, X.; Spieker, W. A.; Kim, J.-G.; Miller, J. T.; Kropf, A. J. *Stud. Surf. Sci. Catal*. 2002, *143*, 45–53.
[62] Bourikas, K.; Kordulis, C.; Lycourghiotis, A. *Catal. Rev*. 2006, *48*, 363–444.
[63] Mang, T.; Knözinger, H. *Appl. Catal*. 1993, *106*, 239–258.
[64] Boitiaux, J. P.; Deves, J. M. *Catalytic Naphtha Reforminng: Science and Technology / Ed. by G.J. Antos et. al*.; Marcel Dekker Inc.: New York, 1995; p. 79-111.
[65] Shelimov, B. N.; Lambert, J.-F.; Che, M.; Didillon, B. *J. Catal*. 1999, *185*, 462–478.
[66] Shelimov, B. N.; Lambert, J.-F.; Didillon, B. *J. Molec. Catal.: Chemical* 2000, *158*, 91–99.
[67] Boujday, S.; Lambert, J. F.; Che, M. *Topics in Catal*. 2003, *24*, 37–42.

[68] Boujday, S.; Lehman, J.; Lambert, J. F.; Che, M. *Catal. Lett*. 2003, *88*, 23–30.
[69] Santacesaria, E.; Carra, S.; Adami, J. *Industrial Engineering Chemistry and Production Research Development* 1977, *16*, 41–47.
[70] Maatman, R. W.; Mahaffy, P.; Hoekstra, Ph.; Addink, C. *J. Catal*. 1971, *23*, 105–118.
[71] Tsymbal, T. V.; Doronin, V. P.; Al't, L. Ya.; Duplyakin, V. K. *Sb. dokl. V Mezhd. simp. po svyazi mezhdu gomogennym i geterogennym katalizom (Proc. V Int. Symp. on the Relationship between Homogeneous and Heterogeneous Catalysis)*, Novosibirsk, 1986, vol. 2, p. 108–117.
[72] Kireeva, T. V.; Doronin, V. P.; Alt, L. Ya.; Dupluakin, V. K. *React. Kinet. Catal. Lett*. 1987, *34*, 261–266.
[73] Duplyakin, V. K. Doctoral (Chem.) Thesis, Novosibirsk, 1990.
[74] Bel'skaya, O. B.; Maevskaya, O. V.; Arbuzov, A. B.; Kireeva, T. V; Duplyakin, V. K.; Likholobov, V. A. *Kinet. Katal*. 2010, *51*, 106–113 [*Kinet. Catal. (Engl. Transl.*). *51*, 98–104].
[75] Trokhimets, A. I. IR spectra of the hydroxyl coating of γ-Al_2O_3. In: Trokhimets A. I.; Mardilovich, P. P.; Lysenko, G. N. *Jhurnal Prikladnoi Spektroskopii* 1979, *30(5)*, 873–877.
[76] Contescu, C.; Jagiello, J.; Schwarz, J. A. *Langmuir* 1993, *9*, 1754–1765.
[77] Hiemstra, T.; Venema, P.; Van Riemsdijk, W. H. *J. Colloid Interface Sci*. 1996, *184*, 680–692.
[78] Bourikas, K.; Kordulis, Ch.; Lycourghiotis, A. *J. Colloid Interface Sci*. 2006, *296*, 389–395.
[79] Digne, M.; Sautet, P.; Raybaud, P.; Euzen, P.; Toulhoat, H. *J. Catal*. 2002, *211*, 1–5.
[80] Morterra, C.; Magnacca, G. *Catal. Today*. 1996, *27*, 497–532.
[81] Liu, X.; Truitt, R. E. *J. Am. Chem. Soc*. 1997, *119*, 9856–9860.
[82] Chukin G. D. *Zh. Strukt. Khim*. 1976. *17*, 122–128.
[83] Kul'ko, E. V.; Ivanova, A. S.; Budneva, A. A.; Paukshtis, E. A. *Kinet. Katal*. 2005, *46*, 141–146 [Kinet. Catal. (Engl. Transl.) *46*, 132].
[84] Paukshtis, E. A. *Infrakrasnaya spektroskopiya v geterogennom kislotnoosnovnom katalize (Infrared Spectroscopy in Heterogeneous Acid–Base Catalysis)*: Nauka: Novosibirsk, 1992.
[85] Lygin, V. I. Zh. Phys. Khim. 2004, *78*, 1469–1474.
[86] Chen, F. R.; Davis, J. G.; Fripiat, J. J. *J. Catal*. 1992, *133*, 263–278.
[87] Rinaldi, R.; Fujiwara, F. Y.; Schuchardt, U. *Appl. Catal. A: General* 2006, *315*, 44–51.
[88] Sohlberg, K.; Pantelides, S. T.; Pennycook, S. J. *J. Am. Chem. Soc*. 2001, *123*, 26–29.
[89] Fitzgerald, J. J.; Piedra, G.; Dec, S. F.; Seger, M.; Maciel, G. E. *J. Am. Chem. Soc*. 1997, *119*, 7832–7842.
[90] Pecharroman, C.; Sobrados, I.; Iglesias, J. E.; Gonzalez-Carreno, T.; Sanz, J. *J. Phys. Chem. B*. 1999, *103*, 6160–6170.
[91] Bel'skaya, O. B.; Drozdov, V. A.; Gulyaeva, T. I.; Arbuzov, A. B.; Moroz, E. M.; Zyuzin, D. A.; Paukshtis, E. A.; Larina, T. V.; Duplyakin, V. K. *Kinet. Katal*. 2009, *50*, 916–921 [*Kinet. Catal. (Engl. Transl.*) *50*, 880–885].
[92] Oudenhuijzen, M. K.; Kooyman, P. J.; Tappel, B.; van Bokhoven, J. A.; Koningsberger, D. C. *J. Catal*. 2002, *205*, 135–146.
[93] Radivojevic, D.; Seshan, K.; Lefferts, L. *Stud. Surf. Sci. Catal*. 2006, *162*, 529–536.
[94] Prestvik, R.; Moljord, K.; Grande, K.; Holmen, A. *J. Catal*. 1998, *74*, 119–129.

[95] Ronning, M.; Gjervan, T.; Prestvik, R.; Nicholson, D. G.; Holmen, A. *J. Catal*. 2001, *204*, 292–304.
[96] Hwang, C.-P.; Yeh, C-T. *J. Molec. Catal. A: Chemical* 1996, *112*, 295–302.
[97] Lieske, H.; Lietz, G.; Spindler, H.; Völter, J. *J. Catal.* 1983, *81*, 8–16.
[98] Lietz, G.; Spindler, H.; Lieske, H.; Hanke, W.; Völter, J. *J. Catal*. 1983, *81*, 17–25.
[99] Huizinga, T.; Drondelle, J. V.; Prins, R. *Appl. Catal. A: General.* 1984, *10*, 199–213.
[100] Foger, K. *Catalysis: Science and Technology. Dispersed Metal Catalysts*. 1984, *6*, 227–307.
[101] Butt, J. B. *Appl. Catal. A: General*. 1985, *15*, 161–173.
[102] Campanati, M.; Fornasari, G.; Vaccari, A. *Catal. Today*. 2003, *77*, 299–314.
[103] Lambert, J. F.; Marceau, E.; Shelimov, B. N.; Lehman, J.; Le Bel de Penguilly, V.; Carrier, X.; Boujday, S.; Pernot, H.; Che, M. *Stud. Surf. Sci. Catal*. 2000, *130 B*, 1043–1048.
[104] Bel'skaya, O. B. Unpublished results.
[105] Kobozev, N. I. *Zh. Phis. Khim.* 1939, *13*, 1–9.
[106] Boreskov, G. K. *Heterogeneous Catalysis in Chemical Industry;* Goskhimizdat: Moscow, 1955.
[107] Chesalova, V. C.; Boreskov, G. K. *Zh. Phis. Khim*. 1956, *30*, 2560–2568.
[108] Boudart, M.; Aldag, A.; Benson, J. E.; Dougharty, N. A.; Girvin, C. *J. Catal*. 1966, *6*, 92–98.
[109] Boudart, M. *Adv. Catal*. 1969, *20*, 153–169.
[110] Van Hardeveld, R.; Hartog, F. *Adv. Catal.* 1972, *22*, 75–84.
[111] Bond, G. C. *Surf. Sci*. 1985, *156*, 966–978.
[112] Hamilton, J. F.; Baetzold, R. C. *Science* 1979, *205*, 1213–1223.
[113] Ponec, V. *Adv. Catal*. 1983, *32*, 149.
[114] Mallat, T.; Frauchiger, S.; Kooyman, P. J.; Schürch, M.; Baiker, A. *Catal. Lett*. 1999, *63*, 121.
[115] Feller, A.; Claeys, M.; van Steen, E. *J. Catal*. 1999, *185*, 120.
[116] Denton, P.; Giroir-Fendler, A.; Praliaud, H.; Primet, M. *J. Catal*. 2000, *189*, 410.
[117] Lane, G. C.; Madica, F. S.; Miller, J. T. *J. Catal*. 1991, *129*, 145.
[118] Mielczarski, E.; Hong, S. B.; Davis, R. J.; Davis, M. E. *J. Catal*. 1992, *134*, 359.
[119] Hayashi, T.; Tanaka, K.; Haruta, M. *J. Catal*. 1998, *178*, 566.
[120] Naito, S.; Tanimoto, M. *J. Chem. Soc., Chem Commun*. 1988, 832.
[121] Gubitosa, G;. Berton, A.; Camia, M.; Pernicone, N. *Stud. Surf. Sci. Catal.* 1983, *16*, 431–440.
[122] Matsuhashi, H.; Nishiyama, S.; Miura, H.; Eguchi, K.; Hasegawa, K.; Iizuka, Y.; Igarashi, A.; Katada, N.; Kobayashi, J.; Kubota, T.; Mori, T.; Nakai, K.; Okazaki, N.; Sugioka, M.; Umeki, T.; Yazawa, Y.; Lu, D. *Appl. Catal. A.* 2004, *272*, 329–338.
[123] Gonzalez, R. D.; Miura, H. *Catal. Rev.-Sci. Eng.* 1994, *36*, 145–177.
[124] Jianguo, W.; Jiayu, Z.; Li, P. *Stud. Surf. Sci. Catal*. 1983, *16*, 57–67.
[125] Machek, V.; Hanika, J.; Sporka, K.; Ruazcička, V.; Kunz, J.; Janáček, L. *Scientific Bases for the Preparation of Heterogeneous Catalysts*. 1983, *16*, 69–80.
[126] Fountzoula, C.; Spanos, N.; Matralis, H. K.; Kordulis, C. *Appl. Catal. B.* 2002, *35*, 295–304.
[127] Bourikas, K.; Hiemstra, T.; Van Riemsdijk, W. H. *J. Phys. Chem.* 2001, *105*, 2393–2403.

[128] Simonov, P. A.; Troitskii, S. Yu.; Likholobov, V. A. *Kinet. Katal*. 2000, *41*, 281–297 [*Kinet. Catal. (Engl. Transl.)*, *41*, 255].
[129] Troitskii, S. Yu.; Chuvilin, A. L.; Bogdanov, S. V.; Moroz, E. M.; Likholobov, V. A. *Izv. Akad. Nauk, Ser. Khim.* 1996, *6*, 1366–1371.
[130] Vakros, J.; Bourikas, K.; Kordulis, C.; Lycourghiotis, A. *J. Phys. Chem. B.* 2003, *107*, 1804–1813.
[131] Carrier, X.; Lambert, J.-F.; Che, M. *J. Am. Chem. Soc*. 1997, *119*, 10137–10146.
[132] Belskaya, O. B.; Duplyakin, V. K.; Karymova, R. Kh.; Nizovsky, A. I.; Larina, T. V.; Maevskaya, O.V. III International Conference "Catalysis: Fundamentals and Applications"; Novosibirsk, 2007.
[133] Boudart, M.; Spenadel, L. *J. Phys. Chem*. 1960, *64*, 204–207.
[134] Gruber, H. L. *J. Phys. Chem*. 1962, *66*, 48–54.
[135] Boronin, V. S.; Poltorak, O. M.; Tarakulova, A. O. *Zh. Phis. Khim.* 1974, *58*, 258–264.
[136] Karnauhov, A. P. *Kinet. Katal*. 1971, *2*, 51520–1532.
[137] Bel'skaya, O. B.; Karymova, R. H.; Nizovskii, A. I. *Abstracts of Papers, II Rossiiskaya konferentsiya Aktual'nye problemy neftekhimii (II Russian Cong. Actual Problems of Petrochemistry)*, Ufa, 2005, p. 77.
[138] Bogomolova, O. B.; Ostrovskii, N. M.; Smolikov, M. D.; Belyi, A. S.; Duplyakin, V. K. *React. Kinet. Catal. Lett*. 1989, *40*, 131–136.
[139] Belyi, A. S; Smolikov, M. D.; Ostrovskii, N. M.; Kolomytsev, Yu. N.; Duplyakin, V. K. *React. Kinet. Catal. Lett.* 1988, *37*, 457–462.
[140] Ostrovskii, N. M.; Belyi, A. S; Kolomytsev, Yu. N.; Duplyakin, V. K *Chemistry and Technology of Fuels and Oils* 1986, *22*, 526–530.
[141] Ostrovskii, N. M.; Chalganov, E. M.; Demanov, Yu. K.; Kolomytsev, Yu. N.; Bogomolova, O. B. *React. Kinet. Catal. Lett*. 1990, *41*, 277–282.
[142] Belyi, A. S. *Kinet. Katal*. 2008, *49*, 587–591 [*Kinet. Catal. (Engl. Transl.*). *49*, 562–567].
[143] Belyi, A. S; Smolikov, M. D.; Kiryanov, D. I.; Udras I. E. Ross. Khim. Zh. 2007, LI, 38–47.
[144] McHenry, K. W.; Bertolachini, R. J.; Brennan, H. M.; Wilson, J. L. *II Int. Congr. Catalysis. Paris*. 1961, *2*, 2296–2311.
[145] Bursian, N. R.; Kogan, S. B.; Davydova, Z. A. *Kinet. Katal*. 1967, *8*, 1283–1289.
[146] Ponec, V. *Stud. Surf. Sci. Catal.* 1982, *11*, 63–77.
[147] Belskaya O. B.; Duplyakin V. K. *VII Conference "Mechanisms of Catalytic Reactions"* St. Petersburg, 2006.
[148] Kalinkin, A. V., Smirnov, M. Yu.; Nizovskii, A. I.; Bukhtiyarov, V. I. *Journal of Electron Spectroscopy and Related Phenomena.* 2009, *177*, 15–18.

Smart Nanocomposites
Volume 1, Issue 2
ISSN: 1949-4823

PHOTOSENSITIVITY AND SHIFT OF CURRENT OSCILLATIONS AT ROOM TEMPERATURE IN SILICON RICH OXIDES UNDER UV/VIS LIGHT

Ragnar Kiebach[1]*, Zhenrui Yu[a], Karim Monfil[1], Jesus Carrillo[2] and Mariano Aceves-Mijares[1]

[1] INAOE, Departments of Electronics,
Apdo. 51, Puebla, Pue. 72000, México
[2] CIDS-ICUAP, Universidad Autónoma de Puebla, México

ABSTRACT

Periodical negative differential conductivities (NDC) in samples with an AL/SRO/Si MOS-like structure were investigated. The SRO (silicon rich oxide) layer was synthesized by Low Pressure Chemical Vapor Deposition (LPCVD). Despite the fact that the NDC already occur at room temperature, a shift towards lower voltage of up to 40% under VIS- and UV-light is observed. Additionally under substrate inversion a photocurrent/dark current ratio of > 100 is found, indicating a high photosensitivity.

INTRODUCTION

Currently, the research on materials containing silicon on a nanoscale level is attracting much interest. Potential applications for these materials are single electron devices [1,2], photonic-crystal-based devises [3], single electron memories [4] or quantum dot transistors [5]. For future applications NDC [or current oscillations] are an interesting phenomenon and several approaches to obtain periodical NDC in semiconductor quantum systems have been reported [6-9]. Recently we published [10] that periodical NDC can be found in SRO at room temperature. SRO is obtained by LPCVD and the fabrication process is completely compatible with the large scale integration technologies.

Here, we report about the photosensitivity of current abnormalities (spikelike NDC and sudden jumps) found in SRO. NDC as well as current jumps shift up to 40 % to lower voltages under VIS- and UV-light compared to ones observed in dark. To our knowledge the

* Corresponding author: woki@risoe.dtu.dk, Tel: +45 4677-5624, Fax:+ 45 4677-5688, Risø National Laboratory, DTU, Fuel Cells and Solid State Chemistry Department, Frederiksborgvej 399 P.O. Box 49, 4000 Roskilde, Denmark

interaction of NDC and light has not been reported so far, and applications of this material property in the field of optoelectronic devices is an interesting possibility.

EXPERIMENTS

The structure studied is an Al/SRO/Si MOS-like capacitor. The SRO layer with a thickness of 150 nm (thickness measured by ellipsometry using a Gärtner L117 ellipsometer with incident laser wavelength of 632.8 nm) was deposited on *n*-type *c*-Si wafers with a (100) orientation and a resistivity of 2-5 Ù.

A silane (SiH_4) and nitrous oxide (N_2O) mixture at 700 °C with a partial pressures ratio Ro = 10 ($SiO_{1.18}$) was used, where Ro is defined as:

$$Ro = p(N_2O)/p(SiH_4).$$

After deposition, SRO films were thermally annealed at 1100 ºC for 180 minutes in N_2 atmosphere. Front Al gate electrodes (area $A = 9.5\times10^{-3}cm^{-2}$, thickness 600 nm) and Al back contact (1000 nm) were evaporated on the annealed sample. *I-V* measurements were performed with a Keithley 6517 electrometer at room temperature and under illumination and dark conditions. A UVGL-55 lamp (254 nm) and a PHILIPS Master TL5 C 800 were used as UV-light and Vis-light sources, respectively. The incident intensities of white- and UV-light are 3.0 mW/cm^2 and 4.3 mW/cm^2, respectively.

RESULTS

Figure 1 shows the typical I-V curves of the samples measured at different voltage sweep directions in dark. First, the I-V curves show a large hysteresis produced by the charge-trapping effect in SRO layer [11]. Also, significant current oscillations and jumps appear in both sides of polarities as marked in the figure.

The oscillations are sensitive to the sweep speed and finally become a current step at slow (3 s) sweep speed.

The phenomena can be explained with a “field domain” in the conduction path, which is considered as a series of Si quantum dots weakly coupled nano capacitors. A more detailed description of the mechanism can be found in ref. [10] where we reported and explained comparable results.

However, in Figure 2, an interesting new phenomenon is observed: The current value and oscillations strongly depend on the illumination condition. Under light, the current is greatly increased. The photocurrent/dark current ratio can be larger than 100 under substrate surface inversion condition.

It has to be noted that this photo response was observed in spite of the opaque gate electrodes. Furthermore, for both polarities, the current oscillations show significant shift to lower voltage values when illuminated. The UV light produces larger shifts than white light illumination.

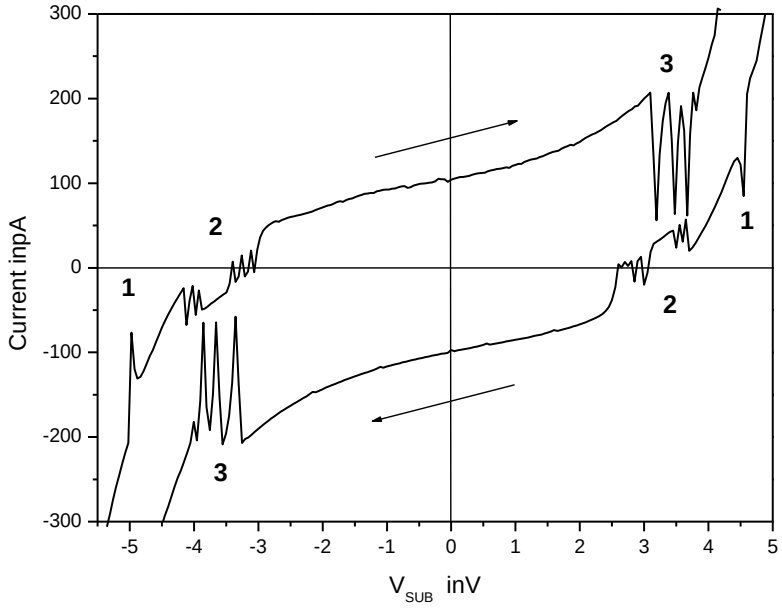

Figure 1. Typical I-V curves of the SRO capacitors measured on both voltage sweep directions with a sweep speed of 100 mV/s.

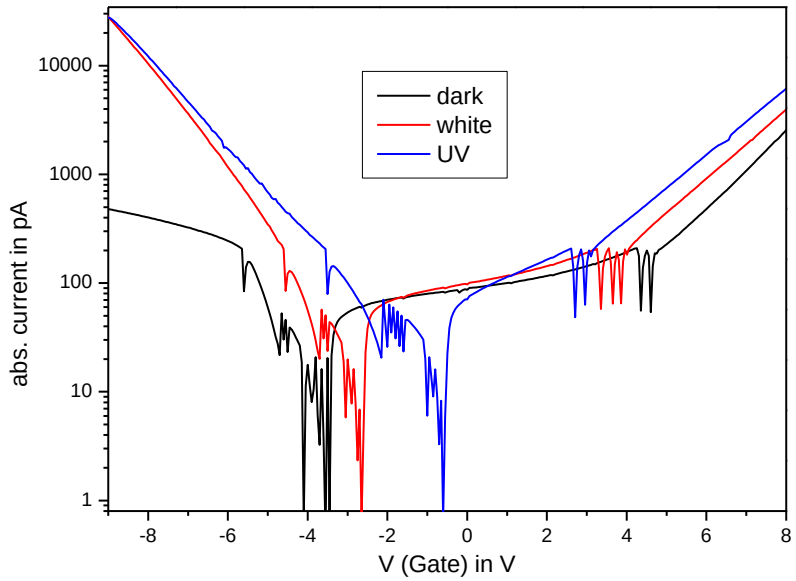

Figure 2. I-V curves for different illumination condition. (black:dark; red: white light; blue UV-light.)

DISCUSSION

At first sight the photosensitivity is unexpected, because the complete conductions path is located under an Al contact in a dark region (DARK region figure 3).

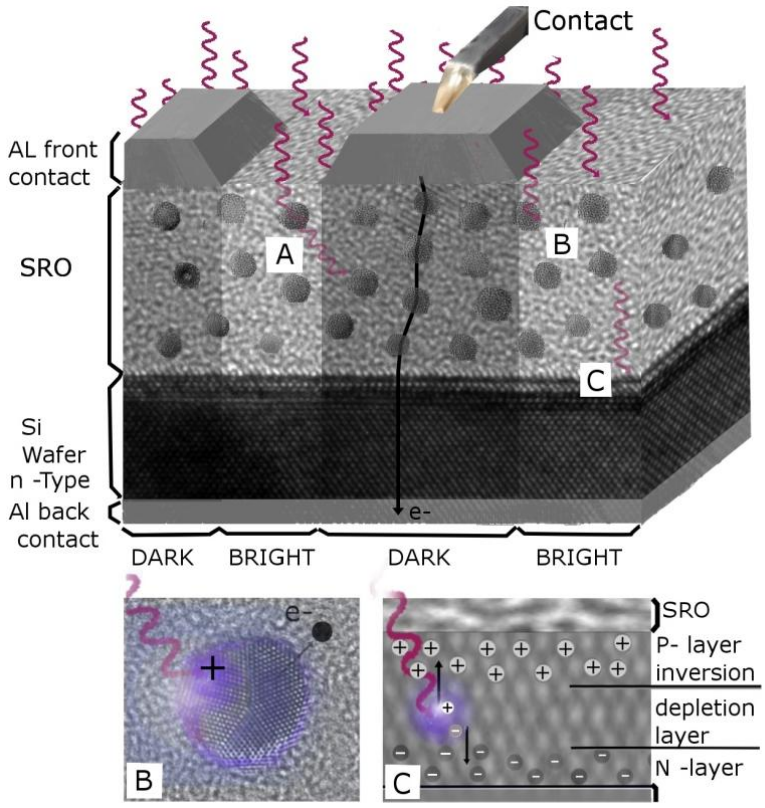

Figure 3. Schematic illustration of the conduction path and light-matter interactions in the nearby region.

Neither UV- nor Vis-light should interact with the Si nano structures contributing to the conduction path. To explain the photosensitivity, light-matter-interactions in the nearby bright regions (BRIGHT region in figure 3) must be considered. The first contribution results from scattered photons (A in figure 3), which reach the current path and interact with the tunneling electrons and/or have influence on the charge/discharge transaction of the silicon nanocrystals (Si nCs). These photons can excite the carriers in the conduction path, shifting the current oscillations to lower voltages. The higher energy of the UV photons explains the larger shift under UV illumination compared to VIS-light. Another possibility is that Si nCs near the dark zone (B in figure 3) absorb photons and form electron-hole pairs.

We reported [12] that samples with a high Si content ($SiO_{1.18}$) show almost no photoluminescence under UV illumination, due to the presence of electron-hole pairs as non-radiant recombination channels for the absorbed energy in the crystals and/or their surrounding matrix. These charges, the electron as well as the hole, can influence the conduction paths in cascade like manner. The created charges can influence the conduction paths under the Al electrodes in two ways: Firstly by changes in the nearby potential and thus in the electrical field distribution within the conduction paths due to the screening effect as mentioned in ref [10] and secondly, the photon excited charges in region B possess a high energy, which can be high enough that their eigenfunction will extend outside the nanodot and interact with nearby ones. This means that the high energy charges will be delocalized

from Si nanodtos and these delocalized charges can move laterally and interact with the conduction paths under the Al gate.

The third possibility is the creation of electron-hole pairs in the substrate. Taking the thickness and the stoichiometry into consideration and based on published results [13,14], a significant amount (> 25 %) of the photons reach the Si substrate. Due to the much higher conductivity of the n-type Si substrate compared with the one of SRO, the charge carriers produced by the photons are less spatial hindered and can contribute easier to the conductivity. A strong hind for this theory can be found in the I-V curves in figure 2. While for high positive values of $V_{(gate)}$ almost the same currents for different illumination conditions are found, the measured current for negative $V_{(gate)}$ values (< -7) under UV/Vis light is more than 100 times higher than the ones found under dark conditions (C in figure 3). Due to the external electric field (negative Voltage at the Al front gate, positive one at the back contact) a p-inversion layer and a wider depletion layer near the boundary of the SRO/substrate is found. A creation of additional charge carries in this area can enable the electrons an easier tunneling from Si nCs near the substrate into the Si wafer. In consequence the current and therewith the photosensitivity increases.

In conclusion, the interaction of all three effects leads to the unique optoelectronic properties found in this material. The bottleneck and rate limiting step in the conduction path is the tunneling process between the different Si nC [10]. The interactions of photons with the SRO in regions near the conduction path are crucial for the shift of the NDC and the photosensitivity at room temperature. While scattered photons and absorption processes in the Si nCs (A and B in figure 3) are responsible for the voltage shift of the NDC, the increase of photocurrent under surface inversion can be explained by absorption processes in the substrate (C in figure 3).

REFERENCES

[1] H. Grabert, M.H. Devoret, *Single Charge Tunneling* (Plenum, New York, 1992).

[2] C.S. Lent, P.D. Tougaw, *J. Appl. Phys*. 74, 6227 (1993).

[3] J.D. Joannopoulos, R.D. Meade, J.N. Winn, *Photonic Crystals* (Princeton University Press, Princeton, N.J, 1995).

[4] K. Yano, T. Ishii, T. Haschimoto, T. Kobayashi, F. Murai, K. Seki, *IEEE Trans. Electron Devices* 41, 1628 (1994).

[5] L. Zhuang, L. Guo and S.Y Chou, *Appl. Phys. Lett*. 72, 1205 (1998).

[6] T. Schmidt, A. G. M. Jansen, R. J. Haug, K. V. Klitzing, K. Eberl, *Phys. Rev. Lett.* 81, 3928 (1998).

[7] J. Wang, B. Sun, X. Wang, Y. Wang, W. Ge, H. Wang, *Appl. Phys. Lett*. 75, 2620 (1999).

[8] J. Chen, J. J. Lu, W. Pan, K. Zhang, X. Y. Chen, W. Z. Shen, *Nanotechnology* 18, 015203 (2007).

[9] Y. Ishikawa, T. Ishihara, M. Iwasaki, M. Tabe, *Electron. Lett*. 37, 1200 (2001).

[10] Z. Yu, M. Aceves-Mijares, K. Monfil, R. Lopez-Estopier, J. Carillo, *J. Appl. Phys*. 103, 063706 (2008).

[11] Z. Yu, M. Aceves-Mijares, J. Carrillo, F. Flores, *Superficies y Vacío* 16, 25 (2003).

[12] F. Flores Gracia, M. Aceves, J. Carrillo, C. Domínguez, C. Falcony, *Superficies y Vacío* 18, 7 (2005).
[13] R. Kiebach, A. Morales, K. Monfil, Z. Yu, E. Quiroga, M. Aceves-Mijares, *Smart Nanocomposites* 1,41 (2010).
[14] A. Luna-López, M. Aceves-Mijares, O. Malik, *Eurosensors 11-14*, MP49 (2005).

Smart Nanocomposites
Volume 1, Issue 2
ISSN: 1949-4823

SPECTROSCOPIC CHARACTERIZATION AND BIOLOGICAL ACTIVITY OF METAL COMPLEXES OF N'-(DIBENZOYLACETONE -2-YLMETHYLENE) 2(4- METHYLPHENYLAMINO)ACETOHYDRAZIDE

Fathy A. El-Saied*, Mohamed I. Ayad, Osama Yousef and Reham W. Farid
Chemistry Department, Faculty of Science,
El-Menoufia University, Shebin El- Kom, Egypt

ABSTRACT

A new series of mono and binuclear Mn(II), Co(II), Ni(II), Cu(II), Zn(II), Fe(III), Ru(III), ZrO(II), Zr(IV) and Hf(IV) complexes of 4-methylphenylaminomono-benzoylacetone hydrazone (H_2L) have been synthesized and characterized by elemental analyses, IR, electronic and ^1H N.M.R spectra, magnetic moments, molar conductivities, thermal analyses (DTA and TGA) and electron spin resonance (ESR). Mononuclear and binuclear complexes are obtained. The ligand behaves as monobasic tridentate one, coordinating through either, azomethine nitrogen atom, carbonyl oxygen atom of the diketone moiety and the enolic oxygen atom of the hydrazone moiety i.e. the ligand reacted in its keto-enol hydrazo form, or through the azomethine nitrogen atom, the carbonyl oxygen atom of the hydrazone moiety and the enolic oxygen atom of the diketone moiety i.e. the ligand reacted in its enol-keto hydrazone form. The ligand also behaves as monobasic and neutral bidentate, coordinating via the azomethine nitrogen atom and the enolic oxygen of the hydrazone moiety or the carbonyl oxygen atom of the diketone moiety. Moreover, the ligand behaved as a dibasic tridentate, coordinating via the azomethine nitrogen atom, the two enolic oxygen atoms of both the hydrazone moiety and the diketone moiety.

The different anions in all complexes are directly attached to the metal ion. The geometrical shapes of the metal complexes are identified by electronic spectra, magnetic moments and ESR measurements. The type of water molecules in the complexes , whether coordinated or hydrated one as well as the thermal behavior of the solid complexes are clarified by the thermal studies (TGA and DTA). The biological activity of the ligand and some of its complexes against the 2nd larval instars of ***S. littoralis*** are also studied.

* Corresponding author E-mail: Fathi_Elsaied@yahoo.com

Keywords: Diketone hydrazone, metal complexes; spectral measurements, thermal analyses and biological activity.

1. INTRODUCTION

The interests in the synthesis and characterization of transition metal complexes of hydrazones lie in their biological and catalytic activity in many reactions [1,2]. The heterocyclic hydrazones constitute an important class of biologically active drug molecules which have attracted attention of medicinal chemists due to their wide ranging pharmacological properties including iron scavenging and antitubercular activities [3,4]. Hydrazide-hydrazones have been demonstrated to possess antibacterial [5], antifungal activity and as antiviral drugs. Besides some hydrazones have been applied as iron chelator drugs in the therapy of anemia and genetic disorders such as β-thalassemia [6-8]. Chelation therapy is the most successful means of treatment of heavy metal poisoning [9]. Coordination compounds of aryl hydrazones were reported as enzyme inhibitors [10] and had useful pharmacological applications [11-13]. Some aryl hydrazones have been used as analytical reagents for the colorimetric and fluorimetric determination of some metal ions [14, 15] and frequently used as catalysts for various chemical reactions [16 ,17] . Metal complexes of isonicotinoyl hydrazones have been used as antitumor agents [18-20]. Extensive investigations of this kind of complexes have been undertaken recently [21- 28]. In the present work, Mn(II), Co(II), Ni(II), Zn(II) Cu(II), Fe(III), Ru(III), ZrO(II) , Zr(IV) and Hf(IV) complexes of 4-methylphenylamino monobenzoylacetone hydrazone have been prepared and characterized. Analytical, spectral, magnetic, molar conductivity and thermal measurements were used to investigate the chemical structure of the ligand and its metal complexes.

2. EXPERIMENTAL

2.1. Instrumentation and Measurements

Reagent grade chemicals were used without further purification. Elemental Micro analyses [C, H, N] were determined in the Micro analytical unit of Cairo University of Egypt. The IR spectra were measured using KBr discs on FT-IR 1650 Perkin-Elmer spectrophotometer. Electronic spectra in N,N'-dimethylformamid (DMF) solutions were recorded using Perkin-Elmer 550. The conductance measurements of complexes in ($1x10^{-3}$M) DMF solution were measured at 25°C with a Bibby conductimeter type MCl. The ^{1}H NMR spectra in DMSO-d6 were recorded using a 300 MHZ Varian NMR spectrophotometer. The solid ESR spectra of complexes were recorded with an ELEXSYS E500 Bruker spectrometer in 3-mm Pyrex Tubes at 298°K. Diphenylpicrylhydrazide (DPPH) used as a g-marker for calibration of the spectra. The thermal analyses (DTA and TGA) were carried out in air using a Shimazu DT-30 thermal analyzer from 27 to 800°C at heating rate of 10°C per minute. Magnetic susceptibilities were measured at 27°C using the modified Gouy method with a

Johnson matthey balance. Magnetic moments were calculated using equation:- $\mu_{eff} = 2.84\sqrt{\chi_M^{corr}.T}$.

2.2. Preparation of the Ligand

2.2.1. Preparation of ethyl 2-(4-methylphenylamino)acetate

4-methylbenzenamine (1.23 g, 1 mmol in 5 mL EtOH) was added to a solution of ethylchloroacetate (1.22 g, 1 mmol in 10 mL of EtOH). Sodium acetate trihydrate (1.36 g, 1 mmol) dissolved in 15 mL distilled water was added to the mixture, then, it was refluxed with stirring for 6 hrs. The product was poured on crushed ice, and the solid precipitate which is formed was filtered off, washed several times with distilled water and dried over anhydrous $CaCl_2$.

2.2.2. Preparation of 2-(4-methylphenylamino)acetohydrazide:

Hydrazine hydrate (2.5 g, 5 mmol) was added drop wise to a solution of ethyl 2-(4-methylphenylamino)acetate (2.09 g, 1mmol) in 30 mL EtOH. The mixture was refluxed with stirring for 3 hrs, and then left to cool at room temperature. The formed precipitate was filtered off, washed several times with EtOH and dried over anhydrous $CaCl_2$.

2.2.3. Preparation of the hydrazone ligand 2-(4-methylphenylamino)-N'-monobenzoyl acetone 2-yl-methylene) acetohydrazide (H_2L)

The hydrazone ligand, 2-(4-methylphenylamino)-N'-(monobenzoylacetone-2-yl-methylene) acetohyd-razide was prepared by mixing 2-(4-methylphenyl amino acetoh-ydrazide (1mmol, 1.95 g dissolved in 20 mL of ethanol) with monobenzoylacetone (1 mmol. 0.162 g, dissolved in 20 mL of ethanol). The mixture was refluxed while stirring for an hour. The formed solid product was filtered off, washed several times with cold ethanol and finally dried under vacuum in presence of anhydrous $CaCl_2$

2.3.Preparation of Metal Complexe

The metal complexes were prepared by adding a hot ethanolic solution of ligand (H_2L) to an equimolar amount or two fold amount of the appropriate metal salt. The reaction mixture was heated with stirring for 3hrs. The separated complex was filtered off, washed several times with ethanol, and dried under vacuum in presence of anhydrous $CaCl_2$.

2.4. Biological Activity

The biological activity of H_2L and some of its complexes was carried out to evaluate its effects on the 2nd larval instar of the Egyptian cotton leafworm *Spodoptera littoralis* (Boisd). The following experimental technique was adopted to determine the above mentioned criterion. Four concentrations for each compound were prepared (0.05, 0.1, 0.2 and 0.4%). Tests were done by dipping the castor learn leaves *Ricinus communis* in each of the tested

concentrations for 30 seconds, then the leaves were left to dry at room temperature. Three replicates were made, 10 larvae for each replicate, the same number of replicates and larvae were considered as control and their larvae were offered castor bean leaves immersed in distilled water. After feeding period of 48 hours on treated leaves, the percentage of larval mortality was recorded and the survival larvae were transferred to another clean jars (0.25 kg cc.) covered with muslin cloth, and supplied with untreated leaves. The percentage of larval mortality was determined at 9^{th} day and then the percentage of total larval mortality was calculated. The percentages of pupation and adult emergence were calculated and different malformation post treatment were also observed. All experisments were carried out at constant conditions of temperature ($27 \pm 2^{o}C$) and relative humidity ($65 \pm 5\%$ R.H.). Percent pupation in relation to the initial number of treated larvae was determined and the appointment of the percentage of adult emergence in relation to the initial number of treated larvae through different concentrations was determined.

3. RESULTS AND DISCUSSION

The reaction of 4-methylphenylamino acetohydrazide with monobenzoylacetone in EtOH 1:1 molar ratio, produced the ligand 4-methylphenylamino monobenzoylacetone hydrazone (H_2L) [Figure 1].

The most important infrared spectral bands of the ligand H_2L are depicted in Table 2. The spectrum of the ligand displays bands at 3410, 3375, 1659 , 1621 and 1578 cm^{-1} , assigned to υ(OH) , υ(N-H), υ(C=O) of the diketone moiety , υ(C=N) and υ(O-C=N), respectively. The appearance of the bands corresponding to the stretching vibrations of the OH and O-C=N and the absence of a band ascribed to the carbonyl group of the hydrazone moiety, indicate that the ligand exists entirely in the keto- enolhydrazo form, as shown in Figure 1.

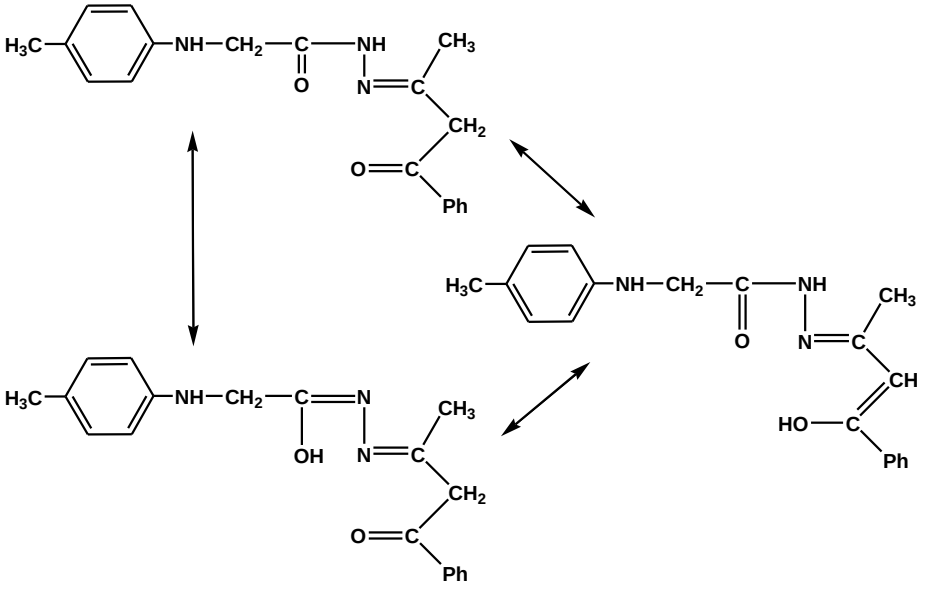

Figure 1. Structural representation of ligand H2L.

The ^{1}H-N.M.R spectrum of the ligand H_2L in DMSO-d_6 shows signals which are compatible with the proposed structure . The singlet signals observed at 12.18 and 10.47 ppm are assignable to δ(-N=C-OH) and δ(-NH-CH_2-) , respectively, can also be taken as a supporting evidence for the proposed keto- enolhydrazo form. The spectrum also exhibits triplet and doublet signals at 3.15 and 4.15 ppm.

These signals are assigned to methylene and methyl groups protons, respectively. Multiple signals appear in the range 6.5 – 7.39 ppm, assigned to aromatic protons.The ^{1}H N.M.R spectrum of complex [Zn(H_2L)(OH)Cl] (14) reveals that, the signal at 12.18 ppm which was ascribed to δ(-N=C-OH) disappeared in the spectrum of the Zn(II) complex, whereas the signals corresponding to δ(-NH-) appeared at 10.051 and 9.801, indicating that the ligand reacted in its keto-form as a neutral ligand. Moreover, a new signal appeared at 13.128 ppm, ascribed to coordinated hydroxo group.

The elemental analyses (Table 1), infrared spectral bands (Table 2) and ^{1}H.N.M.R data are consistent with the structure of the ligand shown in Figure 1.

The reactions of the ligand H_2L with different metal salts ; Cu(II), Co(II), Ni(II), Mn(II), Zn(II), ZrO(II), Fe(III), Ru(III), Hf(IV) and Zr(IV) ions, in 1:1 and 2:1 (M:L) molar ratios, in ethanol led to the formation of mononuclear and binuclear metal complexes as shown in Figure 2.

The obtained metal complexes are air stable, non-hygroscopic, partially soluble in water and most organic solvents except, in N,N`- dimethylformamide (DMF) and dimethylsulphoxide (DMSO), are freely soluble .The values of molar conductivities in DMF (10^{-3} M) solutions, lie within the range 12-20 ohm^{-1} cm^{2} mol^{-1}, indicate that all metal complexes are non-electrolytes[29, 30], evidencing that all anions in metal complexes are directly attached to the metal ion.

The bonding mode of the ligand in the metal complexes has been deduced by comparing the infrared spectra of metal complexes with that of the ligand . The most diagnostic infrared spectral bands of the ligand and its metal complexes are listed in Table 2. Table 2 shows that the infrared spectra of metal complexes 3, 5, 6, 7, 10, 11, 12, 18, 20, 21, 22, 23, 24, and 25, display the bands corresponding to υ(C=O) of the diketone moiety and υ(C=N) at lower frequencies compared to that of the free ligand. Moreover, the band corresponding to the carbonyl group of the hydrazone moiety disappears in the spectra of complexes and instead a new band appears at 1570 cm^{-1}, assigned to υ(C=N -O) .These observations indicate that the ligand reacts with the metal ions in the enol-hydrazo form as a monobasic tridentate and coordinating via the diketone carbonyl oxygen atom, the azomethine nitrogen atom and the enolic-hydrazo oxygen atom.

Table 2 also shows that the infrared spectra of complexes 1, 4, 13, 14, 16, and 17, display the band corresponding to υ(C=O) of the diketone at the same position as that of the free ligand. The spectra of complexes show also that the υ(C=N) and υ(C=O) of the hydrazone moiety reveal a shift to lower frequencies compared to that of the free ligand, this indicates that the carbonyl group of the diketone moiety does not participate in coordination , whereas the azomethine nitrogen atom and the carbonyl oxygen atom of the hydrazone moiety are participated in coordination.

The above observations indicate that the ligand behaves as a neutral bidentate and coordinating via the azomethine nitrogen atom and the carbonyl oxygen of hydrazone moiety. The infrared spectra of complexes 2, 8, and 15 show that the band corresponding to the carbonyl group of the diketone moiety appears at the same position as that of the free ligand.

However, the band corresponding to the carbonyl group of the hydrazone moiety disappears in the infrared spectra of the complexes, and a new band appears at 1560 cm^{-1} , assignable to υ(C=N-O) .Whereas, the band corresponding to υ(C=N) shifts to a lower frequency compared to that of the free ligand.

The above observations indicate that the ligand reacts in the enol-hydrazo form behaving as a monobasic bidentate and coordinating through the azomethine nitrogen atom and the hydrazo-enolic oxygen atom.

Table 1. Elemental analysis, color and molar conductivity for ligand and its metal complexes

No.	Compounds	Color	Salt & molar ratio	Elemental analysis		
				C	H	N
	H_2L	Pale Yellow	-	70.2 (70.3)	7.1 (7.0)	12.8 (12.9)
1	$Cu(H_2L)Cl_2(H_2O)_2]. 1.5H_2O$	Brown	$CuCl_2$ (1:1)	44.3	4.9 (5.6)	7.6 (8.1)
2	$Cu_2 (HL)_2(OAc)_2].2H_2O$	Olive-	$Cu(OAc)_2$ (	55.0	5.6 (5.5)	9.0 (9.3)
3	$Cu(HL)(NO_3)].3.5H_2O$	Dark	$Cu(NO_3)_2$ (1	43.7	5.2(5.5)	11.2
4	$[Cu(H_2L)Br_2(H_2O)_2]$	Dark	$CuBr_2$ (1:1)	39.7	4.2 (4.5)	6.7 (7.2)
5	$[Co(HL)Cl].2.5H_2O$	Dark	$CoCl_2$ (1 :1)	49.3	5.8 (5.6)	8.7 (9.1)
6	$[Co(HL)Br].1.5H_2O$	Dark	$CoBr_2$ (1 :1)	47.0	5.5 (4.9)	8.0 (8.6)
7	$[Co(HL)(OAc)(H_2O)_2].1.5H_2O$	Dark	$Co(OAc)_2$ (	49.5	5.7 (6.2)	7.7 (8.3)
8	$[Co(HL)(NO_3)(H_2O)_3].6H_2O$	Reddish	$Co(NO_3)_2$ (1	36.9	5.7 (6.4)	10.0 (9.2)
9	$[Ni(H_2L)Cl_2].5H_2O$	Dark	$NiCl_2$ (1:1)	41.9	5.7 (5.9)	7.4 (7.7)
10	$[Ni(HL)(OAc)(H_2O)_2]$	Reddish	$Ni(OAc)_2$ (1	53.8	5.7 (5.9)	9.0 (8.8)
11	$[Mn(HL)Cl(H_2O)_2].8.5H_2O$	Brown	$MnCl_2$ (1:1)	38.0	6.0 (6.5)	6.4 (7.0)
12	$[Mn(HL)(OAc)(H_2O)_2].3H_2O$	Dark	$Mn(OAc)_2$ (	48.8	6.0 (6.5)	7.2 (8.0)
13	$[Zn(H_2L)(OAc)(OH)].2H_2O$	Yellow	$Zn(OAc)_2$ (	50.3	5.8 (6.0)	7.4 (8.4)
14	$[Zn(H_2L)Cl(OH)]$	Pale	$ZnCl_2$ (1:1)	51.1	5.4 (4.5)	9.3 (9.5)
15	$[Fe(HL)Cl_2(H_2O)_2].H_2O$	Dark	$FeCl_3$ (1:1)	45.3	4.7 (5.4)	7.7 (8.3)
16	$[Hf(H_2L)Cl_4].H_2O$	Reddish	$HfCl_4$ (1:1)	34.6	4.0 (3.6)	6.2 (6.3)
17	$[ZrO(H_2L)Cl_2(H_2O)_2].3H_2O$	Brown	$ZrOCl_2$ (1:1)	40.1	4.8 (5.2)	7.2 (7.3)
18	$[Zr(HL)(OH)Cl_2]$	Brown	$ZrCl_4$ (1: 1)	46.0	5.0 (4.4)	8.3 (8.4)
19	$[Cu_2(L)Cl_2(H_2O)_5]$	Brown	$CuCl_2$ (2:1)	38.0	4.7 (5.0)	6.6 (7.0)
20	$[Co_2(HL)(OH)Cl_2].3H_2O$	Dark	$CoCl_2$ (2:1)	38.8	5.5 (4.8)	6.9 (7.2)
21	$[Ni_2(HL)Cl_3(H_2O)_4]. 6H_2O$	Dark	$NiCl_2$ (2: 1)	31.3	6.2 (5.6)	5.7 (5.8)
22	$[Mn_2(HL)Cl_3(H_2O)_4].10H_2O$	Brown	$MnCl_2$ (2:1)	27.8	6.1 (6.2)	4.9 (5.3)
23	$[Hf_2(HL)Cl_7].3H_2O$	Reddish	$HfCl_4$ (2:1)	23.0	3.2 (2.7)	4.2 (4.3)
24	$[(ZrO)_2(HL)Cl_3(H_2O)_2].9H_2O$	Reddish	$ZrOCl_2$ (2:1)	26.7	5.0 (5.1)	4.9 (5.0)
25	$[(Zr_2(HL)Cl_7].4H_2O$	Faint	$ZrCl_4$ (2:1)	27.3	4.0 (3.5)	4.7 (5.1)
26	$[Ru_2 (HL)_2Cl_4].2H_2O$	Dark	$RuCl_3$ (1:1)	44.2	4.6 (4.5)	8.0 (8.2)

Table 2. Infrared Spectral Bands For Ligands And Its Metal Complexes

No	υ(H_2O) /(OH)[d]	υ (N-H)/ (OH)[c]	υ (C=O)[a]	υ (C=O)[b]	υ (C=N)	υ (OAc)	υ (NO_3)	υ (M-O)	V (M-N)
H_2L	3410 [d] (vs)	3375 (sh)	-	1659	1621, 1578	-	-	-	-
(1)	3440	3423, 3350, 3290, 3180	1626	1653	1597	-	-	556	423
(2)	3450	3421, 3275, 3380	-	1654	1595, 1560(sh)	1559, 1418	-	519	417
(3)	3440	3422, 3180	-	1582	1582, 1570	-	1383, 1321	553	450
(4)	3440	3421, 3350, 3290, 3136	1625	1656	1591	-	-	553	440
(5)	3450	3371, 3270, 3140	-	1617	1595, 1560	-	-	535	440
(6)	3450	3369, 3155, 3230	-	1615	1595, 1560	-	-	535	425
(7)	3400	3344, 3380	-	1703	1593, 1555	1570, 1330	-	520	425
(8)	3433	3360, 3225	-	1658	1601, 1570	-	1385, 1340	550	430
(9)	3385	3350, 3250	1677	1621	1580	-	-	550	420
(10)	3420	3350, 3250	-	1619	1590, 1570	1565, 1409	-	520	420
(11)	3395	3210	-	1621	1600, 1570	-	-	520	430
(12)	3394	3320, 3220	-	1610	1590, 1570	1567, 1390	-	510	420
(13)	3450	3411[C](Vs), 3150, 3104	1621	1659	1561	1590 , 1405	-	506	449
(14)	3440(sh)	3410[c]	1615	1658	1570	-	-	507	464
(15)	3395	3219, 3136	-	1652	1616, 1595	-	-	490	460
(16)	3421	3390, 3135	1621	1652	1600	-	-	491	464
(17)	3350(br)	3200, 3100	1613	1655	1600	-	-	491	464
(18)	-	3383[c](s), 3230(sh)	-	1613	1595, 1564	-	-	490	464
(19)	3370	3300, 3190	-	-	1610, 1598	-	-	510	470
(20)	3530	3401[c] (vs)	-	1619	1600, 1562	-	-	490	465
(21)	3417(v.b)	3235	-	1619	1590, 1570	-	-	520	460
(22)	3380(v.b)	Obscured	-	1625	1600, 1570	-	-	514	460
(23)	3378 (s, br)	3210	-	1624	1598, 1565	-	-	552	464
(24)	3378(v,br)	3220	-	1635	1597, 1565	-	-	490	461
(25)	3367(v,br)	3250, 3120	-	1615	1595, 1560	-	-	490	462
(26)	3384	3230, 3120	1738	-	1595[d], 1570	-	-	540	487

[a]= hydrazonic, [b] = ketonic, [c]= hydroxo (OH), [d]= enolic –OH.

The infrared spectrum of complex 9 reveals that, the band corresponding to the carbonyl group of the hydrazone moiety does not show a shift relative to that of the free ligand, whereas the bands assigned to the υ(C=O) of the diketone moiety and υ(C=N) reveal a shift to lower frequencies , indicating that the ligand coordinates to the metal ion through the azomethine nitrogen atom and the carbonyl oxygen atom of the diketone moiety i.e. the ligand behaves as a neutral bidentate one.

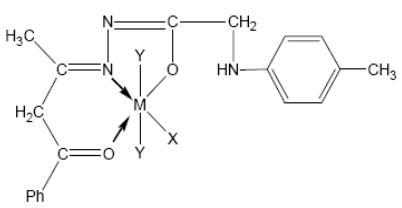

$[M(HL)XY_2].nH_2O$

M=Cu(II),X=NO_3, Y=0, n=3.5	(3)
M=Co(II),X= Cl, Y=0, n=2.5	(5)
M=Co(II),X= Br, Y=0,n=1.5	(6)
M=Co(II),X=OAc, Y=H_2O, n=1.5	(7)
M=Ni(II), X=OAc, Y=H_2O, n=0	(10)
M=Mn(II),X=Cl, Y=H_2O, n= 8.5	(11)
M=Mn(II),X= OAc, Y=H_2O,n =3	(12)
M=Zr(IV), X= OH, Y= Cl, n= 0	(18)

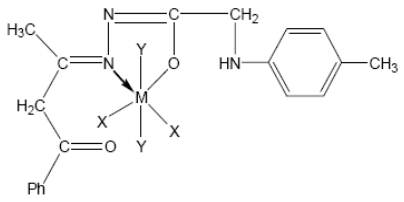

$[M(H_2L)X_2Y_2].nH_2O$

M=Cu(II), X=Cl, Y=H_2O, n=1.5	(1)
M=Cu(II),X=Br, Y=H_2O, n=0	(4)
M=Zn(II), X= OAc & OH, Y=0, n=2	(13)
M=Zn(II), X=Cl, & OH, Y=0, n=0	(14)
M=Hf(IV), X=Y=Cl, n=1	(16)
M=ZrO(II), X=Cl, Y=H_2O, n=3	(17)

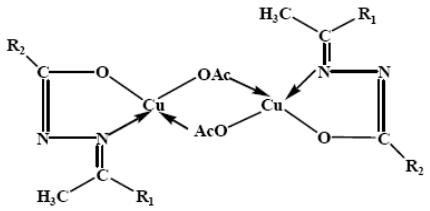

R_1 = $-CH_2-CO-Ph$, R_2 = $-CH_2-NH-C_6H_4-CH_3$

$Cu_2(HL)_2(OAc)_2].2H_2O$

(2)

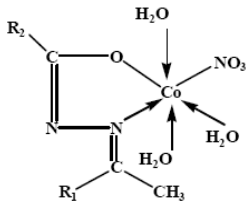

$[Co(HL)(NO_3)(H_2O)_3].6H_2O$

(8)

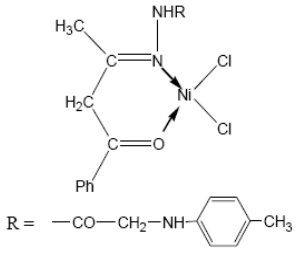

R = $-CO-CH_2-NH-C_6H_4-CH_3$

$[Ni(H_2L)Cl_2].5H_2O$

(9)

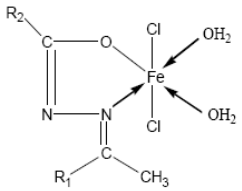

$[Fe(HL)Cl_2(H_2O)_2].H_2O$

(15)

Figure 2 continued on next page

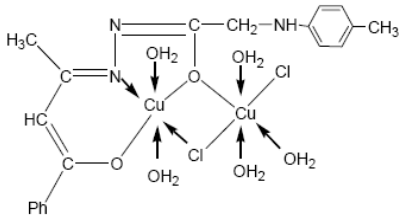

$[Cu_2LCl_2(H_2O)_5]$

(19)

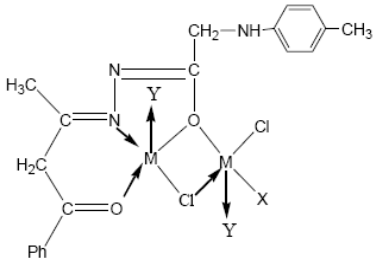

$[M_2(HL)Cl_2XY_2].nH_2O$

M=Co(II), X=OH, Y=0, n=3 (20)

M=ZrO(II), X=Cl, Y=H_2O, n=9 (24)

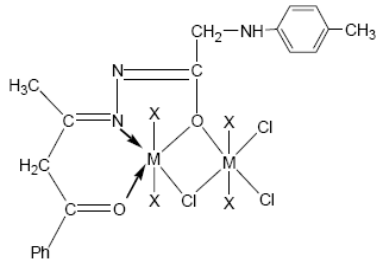

$[M_2(HL)Cl_3X_4].nH_2O$

M=Ni(II), X=H_2O, n=6 (21)

M=Mn(II), X=H_2O, n=10 (22)

M=Hf(IV), X=Cl, n=3 (23)

M=Zr(IV), X=Cl, n=4 (25)

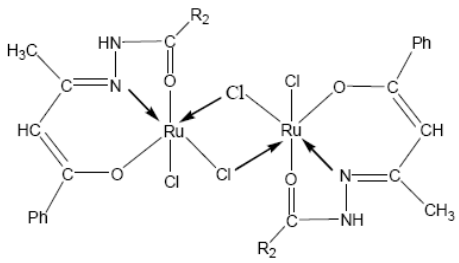

R_2=-CH_2-NH- ph-CH_3

$[Ru_2(HL)Cl_4].H_2O$

(26)

Figure 2. Representation of the chemical formulas of metal complexes.

The infrared spectrum of complex 19, shows that the bands characteristic to the two carbonyl groups are disappeared and two new bands appeared at 1610 and 1598 cm^{-1}, assigned to υ(C=C) and υ(C=N-O) respectively, this indicates that the two carbonyl groups are changed to the enol forms. The spectrum also shows that the band corresponding to υ(C=N) , shifted to lower frequency compared to that of the free ligand. The above observations suggested that the ligand reacted with copper(II) ions in this complex in the enol form and behaves as a dibasic tridentate one, coordinating via the azomethine nitrogen atom and the two enolic oxygen atoms . The ligand behaved again as a monobasic tridentate one , as in case of complex 26 , but in a coordinating manner different from the first manner. The infrared spectrum of complex 26 displays bands at 1738, 1595, and 1570 cm^{-1} , assigned to the stretching vibrations of uncoordinated carbonyl group of the hydrazone moiety , υ(C=C) and coordinated azomethine group respectively. This suggestion is also supported by the disappearance of the band corresponding to υ(C=O) of the diketone moiety.The infrared spectra of the hydroxo complexes (13, 14, 18, and 20) show strong bands at 3411, 3410, 3383 and 3401 cm^{-1}, respectively, assigned to terminal coordinated OH group[32].Infrared

spectral studies reported on the acetate complexes [27, 32], indicate that , the acetato ligand may coordinate to the metal centre in either a monodentate , bidentate or bridging manner. The $\upsilon_a(CO_2)$ and $\upsilon_s(CO_2)$ bands of the free acetate ions appear at 1560 and 1416 cm^{-1}, respectively. In monodentate coordination υ(C=O) is found at higher energy than that of $\upsilon_a(CO_2)$ and υ(C-O) is found at lower energy than that of $\upsilon_s(CO_2)$. As a result, the separation between the two $\upsilon_a(CO_2)$ and $\upsilon_s(CO_2)$ bands is much larger in monodentate complexes, then, the infrared spectrum of the ion found in complex 2 displays the $\upsilon_a(CO_2)$ at 1559 cm^{-1} and the $\upsilon_s(CO_2)$ one at 1418 cm^{-1}, consistent with a bridging acetate ligand binds two copper(II) ions to form binuclear compound . Whereas, the infrared spectra of complexes 7, 10, 12 and 13 display the $\upsilon_a(CO_2)$ at 1570, 1565, 1567 and 1590 cm^{-1} and the $\upsilon_s(CO_2)$ at 1330, 1409, 1390 and 1405 cm^{-1} , respectively, which is compatible with a monodentate coordination mode for acetate group .The infrared spectra of the complexes 3 and 8, containing nitrate ligand show bands at 1340- 1321 cm^{-1} and 1385- 1383 cm^{-1}, assigned to υ_1 and υ_4 modes of nitrate group, indicating that the nitrate group is terminally bonded as a monodentate nitrate group [33] .The presence of water molecules within the coordinated sphere in the hydrated complexes 1, 3, 7, 8, 10, 11, 12, 15, 19, 21, 22, and 26 is supported by the appearance of infrared spectral bands in the ranges 3450- 3350 cm^{-1}, 885 – 827 cm^{-1}, and 695 – 640 cm^{-1}, assigned to OH stretching , H_2O rocking and H_2O wagging, respectively. {34]. The absence of the latter two bands in the spectra of the rest complexes 2, 4, 5, 6, 9, 16, 17, 20, 23, 24 and 25, indicating that the water in these complexes is lattice rather than coordinated. The spectra of metal complexes display two new bands at 556 – 490 and 487 – 417 cm^{-1}, assigned to υ(M-O) and υ(M-N), respectively [27].

3.1. Magnetic Moments and Electronic Spectral Data for Metal Complexes

The electronic absorption spectral bands as well as the room temperature magnetic moments (μ_{eff} B.M.) per a metal atom of the metal complexes are listed in Table 3.

The magnetic moments for the copper(II) complexes 1, 2, 3, 4 and 19 are 1.72, 1.6, 1.8, 1.69 and 1.2 B.M. respectively. The moments of complexes 1, 3 and 4 correspond to one unpaired electron [35] .The moments of complexes 2 and 19 are well bellow the spin only value (1.73 B.M.), indicating spin –exchange interactions between the copper(II) ions in a square planar or octahedral geometry [36].

The spin exchange interactions between copper(II) ions may be explained on the basis of a bridging by acetate ligand as in complex 2 or a chloride and an oxygen bridges as in complex 19. The electronic spectra of copper(II) complexes 1, 4 and 19 exhibit two bands at 600 nm and 580 nm, assigned to $^2B_1 \rightarrow {}^2E$ and $^2B_1 \rightarrow {}^2B_2$ transitions, respectively, indicating , a distorted tetragonal structure[37, 38]. The electronic spectra of copper(II) complexes 2 and 3 show a broad structured band at 640 and 700 , respectively , which suggesting a square planar geometry around the copper(II) ion[39].

Octahedral, tetrahedral and square planar cobalt(II) complexes show magnetic moment values between 4.7–5.2, 4.2–4.8 and 2.2–2.9 B.M., respectively [29, 40-42]. The room temperature magnetic moment values for cobalt (II) complexes 5–8 are 4.3, 4.25, 5.2 and 4.9 B.M. respectively.

Table 3. Magnetic moment values and electronic spectral bands for metal complex

No.	Complexes	μ_{eff} (B.M.) per a metal atom	d –d transitions (nm)
1	$[Cu(H_2L)Cl_2(H_2O)_2]. 1.5H_2O$	1.72	600, 580
2	$[Cu_2(HL)_2(OAc)_2]. 2 H_2O$	1.60	640(br)
3	$[Cu(HL)(NO_3)]. 3.5H_2O$	1.80	700(br)
4	$[Cu(H_2L)Br_2(H_2O)_2]$	1.69	600, 580
5	$[Co(HL)Cl]. 2.5H_2O$	4.30	685, 660, 640, 610
6	$[Co(HL)Br]. 1.5H_2O$	4.25	700, 635, 615
7	$[Co(HL)(OAc)(H_2O)_2].1.5H_2O$	5.20	690(w), 640(w)
8	$[Co(HL)(NO_3)(H_2O)_3]. 6H_2O$	4.90	630(sh), 600(sh)
9	$[Ni(H_2L)Cl_2].5H_2O$	4.00	785 w), 590
10	$[Ni(HL)(OAc)(H_2O)_2]$	3.01	700(w), 550
11	$[Mn(HL)Cl(H_2O)_2].8.5H_2O$	5.22	590(w, sh), 580
12	$[Mn(HL)(OAc)(H_2O)_2].3H_2O$	5.30	590, 575
15	$[Fe(HL)Cl_2(H_2O)_2].H_2O$	5.40	700(w), 600(sh)
19	$[Cu_2LCl_2(H_2O)_5]$.	1.2	610, 585
20	$[Co_2(HL)(OH)Cl_2].3H_2O$	2.55	670, 655, 600
21	$[[Ni_2(HL)Cl_3(H_2O)_4].6H_2O$	2.01	700 (w), 640
22	$[Mn_2(HL)Cl_3(H_2O)_4].10H_2O$	2.80	590(w,sh), 575
26	$[Ru_2(HL)_2Cl_4].2H_2O$	1.20	800

The first two values, are consistent with a tetrahedral arrangement around the cobalt(II) ion in complexes 5 and 6. Whereas, the last two values are indicative for an octahedral geometry around the cobalt(II) ion in complexes 7 and 8. The considerably high values ruled out any spin- spin interactions between cobalt(II) ions. The electronic spectra of cobalt(II) complexes 5 and 6 show a strong multi split band (700 – 685, 660 – 635, 615 – 610 nm) , attributed to the $^4A_{2g} \rightarrow {}^4T_{1g}$ (P) (υ_3) transition in a tetrahedral arrangement around cobalt(II) [43, 44]. However, cobalt(II) complexes 7 and 8 display two weak bands at 690 – 630 and 640 -600 nm which may be assigned to $^4A_{2g} \rightarrow {}^4T_{1g}$ (P) (υ_3) and $^4T_{1g} \rightarrow {}^4A_{2g}$ (υ_2), respectively, which is indicative for octahedral cobalt(II) geometry [45].

The nickel(II) complexes were found to be paramagnetic which excludes the possibility of a square planar configuration. The room temperature magnetic moment values of nickel(II) complexes 9, 10 and 21 are 4.0, 3.01 and 2.01 B.M. respectively. The value corresponding to complex 9 is indicative of a tetrahedral geometry around the nickel(II) ion, whereas, the values corresponding to complexes 10 and 21 are compatible with an octahedral arrangement around the nickel(II) ion. Moreover, the low magnetic moment value of complex 21 indicates spin exchange interactions tack place between the nickel(II) ions through an oxygen bridge

and a chloride bridge. The electronic spectra of nickel(II) complexes 10 and 21 show two bands at 700 and 600- 550 nm, assigned to $^3A_{2g}(F) \rightarrow {}^3T_{1g}(F)$ (υ_2) and $^3A_{2g}(F) \rightarrow {}^3T_{1g}(P)$ (υ_3) transitions, respectively in pseudo- octahedral complexes [46] . Whereas, the nicke(II) complex 9 has an electronic absorption spectrum typical of a tetrahedral geometry [47]. The spectrum shows two bands at 785 and 590 nm, which may be assigned to the transitions $^3T_1(F) \rightarrow {}^3A_2(\upsilon_2)$ and $^3T_1(F) \rightarrow {}^3T_1((P)$ (υ_3), respectively.

The magnetic moment values of manganese(II) complexes 11 and 12 are 5.22 and 5.3 B.M. respectively. These values are close to the expected value for a high – spin $3d^5$ octahedral system. Whereas, the magnetic moment value of complex 22 is 2.8 B.M. suggesting octahedral geometry around manganese(II) [48]. The low moment value may be ascribed to super-exchange interaction which may takes place between manganese(II) ion through a bridging enolic- oxygen atom and a bridging chloride atom bind two Mn(II) ions forming a binuclear manganese complex 22. The electronic spectra of manganese(II) complexes display two weak bands at 590 and 575 nm. These bands are both lapport and spin-forbidden . However, due to instantaneous distortion of the octahedral structure around Mn(II) ion, weak bands sometimes do appear [48, 49].

The iron(III) complex has a magnetic moment value equals 5.4 B.M. , indicating high spin octahedral iron(III) [50]. The electronic spectrum of iron complex 15 shows two bands at 700 and 600 nm, which are compatible with a tetragonally distorted octahedral geometry around the iron(III) ion [51].

Ruthenium(III) complex 26 gave a magnetic moment value of 1.2 B.M. , well below the spin only value , indicating spin-exchange interactions between ruthenium(III) ions through two chloride bridges also, indicating low- spin Ru(III) complex . The electronic spectrum of complex 26 shows one band at 800 nm . By taking in consideration that the ligand in case of Ru(III) is considered as a strong ligand , one can assume that this intense band may be ascribed to $^2T_{2g} \rightarrow {}^2A_{2g}$ transition [52] in an octahedral geometry.

3.2. Electron Spin Resonance (ESR)

The ESR spectra of the copper(II) complexes **(1, 2, 3** and **4)** were recorded in polycrystalline state at room temperature. The ESR spectra of the copper(II) complexes exhibited anisotropic signals with $g_{\|}$= 2.278. 2.171, 2.242 and 2.249; $g_{\perp}$= 2.044, 2.055, 2.044 and 2.044; g_{iso}= 2.122, 2.094, 2.109 and 2.112 respectively, which are characteristic for a d^9 system with an axial symmetry type of d_{x2-y2} ground state. The g values for the copper(II) complexes denote square planar and octahedral geometries around copper(II) ions [53]. Since $g_{\|} > g_{\perp}$ indicating a tetragonal distortion around the copper(II) ions corresponding to elongation along the four fold symmetry Z-axis. The trend $g_{\|} > g_{\perp} > g_e$ (2.0023) shows that the unpaired electron is localized in the d_{x2-y2} orbital [54-55]. In addition exchange coupling interaction between two copper(II) ions explained by Hathaway expression $G = (g_{\|}-2)/(g_{\perp}-2)$. If G > 4.0, the exchange interaction is negligible which is typically the case for complexes **1, 3** and **4** (G= 6.38, 5.52 and 5.71). When the value of G < 4.0, a considerable exchange coupling is present in solid complex, which is typically the case for complex **2** (G = 3.077). Kivelson and Neiman noted that for an ionic environment, $g_{\|}$ is normally 2.3 or larger but for

covalent environment, $g_{\|}$ is less than 2.3. The $g_{\|}$ value for copper(II) complexes were lower than 2.3 (2.117-2.78) consequentially the environment is essentially covalent [54-55].

3.3. Thermal Analyses (TG and DTA)

The TG-DTA results for some of solid metal complexes are depicted in Table 4. The results are in good agreement with the structural formulae shown in Figure 2

Table 4 concluded that, there is a general pattern for the thermal behaviour of solid metal complexes, whereby, the complexes show mostly four main stages. The first stage is the loss of hydrated water molecules at 28-140 ˚C, followed in a second decomposition stage by the loss of the coordinated water at 85- 275 ˚C , then a third stage occurred which is the loss of coordinated anions (Cl, Br, NO_3 and CH_3COO) at 130 – 320˚C. The last stage is the loss of the ligand and formation of metal oxide within the temperature range 107 -675 ˚C.

Table 4. TGA and DTA data for some metal complexes

Complex	Temp (˚C)	Weight loss % Found(calcd)	Species removed	DTA peaks (˚C)
$[Cu(H_2L)Cl_2(H_2O)_2].1.5H_2O$	33-117 117-177 177-341 341-675 675	5.3 (5.4) 7.2 (6.9) 14.4(13.6)	-1.5 H_2O - 2 coordinated H_2O -2 coordinated Cl loss of ligand formation of metal oxide	58, 100 136 311 391
$[Cu(HL)(NO_3)]3.5H_2O$	28 – 140 140-500 500	12 (12.3)	-3.5 H_2O loss of ligand formation of metal oxide	79, 120 192, 244, 384, 493, 612
$[Co(HL)Br].1.5H_2O$	28-107 107-680 680	5.1 (5.5)	-1.5 H_2O loss of ligand formation of metal oxide	50, 73 110, 145, 360, 371,447,647, 701
$[Co(HL)(OAc)(H_2O)_2].1.5H_2O$	30-85 85-189 189-265 265-435 435	5.1(5.4) 6.7(7.1) 11.6(11.7)	-1.5 H_2O -2 coordinated H_2O - OAc loss of ligand formation of metal oxide	77 96, 110 230 291,408
$[Co(HL)(NO_3)(H_2O)_3].6H_2O$	32-135 135-163 163-245 245-441 441	17.2(17.8) 8.2(8.9) 11.0(10.2)	-6H_2O -3 coordinated H_2O - coordinated NO_3 loss of ligand formation of metal oxide	80, 110 150 242 350, 400 470
$[Ni(H_2L)Cl_2].5H_2O$	34-140 140-270 270-600 600	16.6(16.6) 13.3(13.1)	-5H_2O -2 coordinated Cl loss of ligand formation of metal oxide	70, 124 394, 459, 548 712

Continued on next page

Table 4. (Continued)

Complex	Temp (˚C)	Weight loss % Found(calcd)	Species removed	DTA peaks (˚C)
$[Mn(HL)Cl(H_2O)_2].8.5H_2O$	33-131 133-275 275-635 635	26.2(25.4) 11.7(11.9)	-8.5H_2O -2 coordinated H_2O+ 1 Cl loss of ligand formation of metal oxide	64, 111 199 481, 564
$[Mn(HL)(OAc)(H_2O)_2].3H_2O$	31-73 73-140 140-240 240-486 486	9.6(10.2) 5.9(6.8) 11.8(11.2)	-3H_2O -2 coordinated H_2O - 1 OAc loss of ligand formation of metal oxide	69 120 158 292 503
$[Zn(H_2L)(OAc)(OH)].2H_2O$	53-108 110-130 130-217 217-540 540	7.1(7.2) 4.2(3.4) 12.2(11.8)	-2H_2O -1 coordinated OH - OAc loss of ligand formation of metal oxide	80, 100 123 189 275, 360, 53
$[(ZrO)_2(HL)Cl_3(H_2O)_2].9H_2O$	26-135 135-175 182-320 320-536 536	15.5(15.0) 8.3(8.6) 13.0(12.7)	-7H_2O -2H_2O+ 2 coordinated H_2O -3 coordinated Cl loss of ligand formation of metal oxide	70, 100 153, 168 365,527

3.4. Biological Activity

Table (5): summarized the efficicay of ligand H_2L and its complexes at different concentrations against 2nd larval instar of *S. littoralis*. It is quite clear from our results that the different concentrations of the tested complexes (0.05, 0.1, 0.2, and 0.4%) clearly affected the percentage of larval mortality, increasing gradually with an increase in concentration [56, 57]. For example, in case of 1, the total mortality (%) was 66.7, 80.0, 86.7 and 100, respectively. On the other hand, the corresponding figures for 9, 17 and 5 were 26.7, 46.7, 90.0 and 93.3; 26.7, 40.0, 70.0 and 93.3%, respectively. The data tabulated in Table (5) revealed that the most potent complexes at the three different concentrations (0.05, 0.1 and 0.2%) was 3, 10, 23, 14 and 22. However, at concentration of 0.4% all applied complexes induced 100% mortality 48h post treatment except complexes of 1, 2, 4, 9, 17, 18, 20, 24 and 26.

From the obtained results, one can say that the biological activity of the tested complexes was increased gradually with an increase in the applied concentrations. On the other hand, data presented in Table (5) clearly indicated that the maximum biological activity was observed with ligand [58], where the total of tarval mortality after 48 h was 100% even at lower concentration (0.05%). The total percentage of larval mortality in the check experimental was 6.7.

Table 5. Effect of ligand and some of its metal complexes at different concentrations on the percentage of larval mortality of the cotton leaform *Spodoptera littoralis* (Boisd) treated as 2nd larval instar at 48 hrs and 9th day post- treatment

Compound		Concentration (%)											
		0.05			0.1			0.2			0.4		
		48 h	9 days	Total Mortality%	48 h	9 days	Total Mortality%	48 h	9 days	Total Mortality%	48 h	9 days	Total Mortality%
check		0	6.7	6.7	0	6.7	6.7	0	6.7	6.7	0	6.7	6.7
H_2L		100	-	100	100	-	100	100	-	100	100	-	100
1	$CuCl_2$	56.7	10.0	66.7	63.3	16.7	80	80	6.7	86.7	96.7	3.3	100
2	$Cu(OAc)_2$	20.0	6.7	26.7	40.0	6.7	46.7	66.7	16.7	83.3	96.7	3.3	100
3	$Cu(NO_3)_2$	33.3	6.7	40	73.3	0	73.3	93.3	6.7	100	100	-	100
4	$CuBr_2$	26.7	13.3	40	46.7	13.3	60	73.3	10.0	83.3	90.0	6.7	96.7
5	$CoCl_2$	40.0	13.3	53.3	60.0	6.7	66.7	80.0	10.0	90	100	-	100
7	$Co(OAc)_2$	33.3	13.3	46.7	46.7	0	46.7	76.7	13.3	90	100	-	100
9	$NiCl_2$	13.3	13.3	26.7	40.0	6.7	46.7	76.7	13.3	90	93.3	0	93.3
10	$Ni(OAc)_2$	40.0	6.7	46.7	80.0	0	80	96.7	3.3	100	100	0	100
11	$MnCl_2$	26.7	33.3	60	53.3	6.7	60	86.7	6.7	93.3	100	0	100
13	$Zn(OAc)_2$	53.3	6.7	60	66.7	0	66.7	93.3	3.3	96.7	100	0	100
15	$FeCl_3$	33.7	6.7	40	66.7	0	66.7	86.7	3.3	90	100	0	100
23	$HfCl_4$	60.0	0	60	80.0	0	80	100	0	100	100	0	100
14	$ZnCl_2$	66.7	6.7	73.3	86.7	0	86.7	96.7	3.3	100	100	0	100
17	$ZrOCl_2$	20.0	6.7	26.7	33.3	6.7	40	56.7	13.3	70	83.3	10.0	93.3
18	$ZrCl_4$	40.0	0	40	53.3	0	53.3	76.7	13.3	90	93.3	6.7	100
20	$CoCl_2$ (2:1)	33.3	6.7	40	40	6.7	46.7	90	3.3	93.3	80	16.7	96.7
22	$MnCl_2$ (2:1)	53.3	0	53.3	73.3	0	73.3	96.7	3.3	100	100	0	100
24	$ZrOCl_2$ (2:1)	26.7	6.7	33.3	40.0	6.7	46.7	66.7	16.7	83.3	90.0	6.7	96.7
26	$RuCl_3$	20.0	13.3	33.3	46.7	6.7	53.3	90.0	3.3	93.3	96.7	3.3	100

Table 6. Effect of ligand and some of its complexes at different concentrations on the percentages of pupation and adult emergence of the cotton leafworm *Spodoptera littoralis* (Boisd) treated as 2nd larval instar

Complex No.	Concentration (%)							
	0.05		0.1		0.2		0.4	
	Pupation (%)	Adult Emergence (%)	Pupation (%)	Adult Emergence (%)	Pupation (%)	Adult Emergence (%)	Pupation (%)	Adult Emergence (%)
Check	93.3	93.3	93.3	93.3	93.3	93.3	93.3	93.3
Ligand	0	0	0	0	0	0	0	0
1	26.7	23.3	200	20.0	13.3	6.7	0	0
2	73.3	66.7	53.3	53.3	16.7	6.7	0	0
3	60.0	53.3	26.7	20.0	0	0	0	0
4	60.0	53.3	40.0	33.3	16.7	16.7	3.3	0
5	46.7	46.7	33.3	33.3	10.0	10.0	0	0
7	53.3	40.0	53.3	46.7	70.0	3.3	0	0
9	73.3	66.7	53.3	46.7	70.0	10.0	6.7	0
10	53.3	40.0	20.0	13.3	0	0	0	0
11	66.7	60.0	40.0	33.3	6.7	6.7	0	0
13	40.0	33.3	33.3	33.3	3.3	3.3	0	0
15	60.0	46.7	33.3	33.3	10.0	6.7	0	0
23	40.0	40.0	20.0	20.0	0	0	0	0
14	26.7	20.0	13.3	13.3	0	0	0	0
17	73.3	60.0	60.0	53.3	30.0	30.0	6.7	0
18	60.0	46.7	46.7	40.0	10.0	10.0	0	0
20	60.0	53.3	46.7	46.7	3.3	6.7	3.3	3.3
22	46.7	40.0	26.7	26.7	0	0	0	0
24	66.7	53.3	53.3	46.7	16.7	13.3	3.3	0
26	66.7	66.7	46.7	40.0	6.7	6.7	0	0

The percentage of pupation was greatly affected by all tested concentrations of different complexes as shown in Table (6). There was an inverse relationship between the concentration and the pupation percentages. For example, in case of treated second larval instar of *S. littoralis* with complex 5, this criterion was 60.0, 46.7, 6.7 and 3.3% at concentrations of 0.05, 0.1, 0.2 and 0.4%, respectively, compared to 93.3% in check experiment. The same effects were detected in all of other tested complexes.

Results in Table (6) indicated that there were reduction in the percentage of adult emergence with all tested complexes compared to control (check group). The percentage of adult emergence was decreased with an increase in the applied concentration. For example in case of treated larval with 18, this biological parameter was 66.7, 53.3, 6.7 and zero% at concentrations of 0.05, 0.1, 0.2 and 0.4%, respectively, compared to 93.3% in untreated larval (check experiment). On the other hand, it is interesting to say that the adult moths of this pest failed to emerge from pupation (pupal skin) in case of larval treated with different complexes at 0.4%, except those treated with 20, where the percentage of adult emergence was 3.3%.

It is evident from our results and observations that there was severe effect induced by the tested complexes. Different external features of mortality due to feeding 2nd larval instars of *S. littoralis* on castor bean leaves treated with different concentrations: larval became inactive and gradually stopped feeding, became completely paralyzed, appeared to be wet and dark colors spread all over the body and larval is being shrieked (Figure 3) compared to normal healthy larval (Figure 4). Some treated larvae failed to pupate, however, severe deformations were observed post larval treatment such as: larval pupal intermediates (larval with pupal head, larval mouth parts attached to pupal cuticle); pupal larval intermediates (pupal with larval head and pupae with head and thoracic legs and pupal abdomen) (Figure 5).

Figure 3. Different deformations of *S. Littoralis* larvae post treatment.

Figure 4. Dorsal and ventral views of the normal untreated larvae of *S. Littoralis.*

Figure 5. Larval- pupal intermediates as side effect of treated 2nd larval instar of *S. Littoralis* with different complexes.

Pupal deformations resulting from larval treatment includes (small sized pupae cannot escape from their larval exuvia and dead pupae) (Figures 6, 7) compared to normal well developed pupae (Figure 8).

Figure 6. Pupal deformations of *S. Littoralis* resulted from treated 2nd larval instar with different complexes.

Figure 7. Deformations of *S. Littoralis* Pupae (pupal- larval intermediates) as side effect of larval treatments.

Figure 8. Normal pupae of *S. Littoralis*.

Figure 9. Different malformations of the emerged adults treated with different complexes as 2nd larval instar.

Figure 10. Normal emerged moths of *S. Littoralis.*

Malformalions of adult moths emerged from treated larvae included: partial emergence of adults adults with pupal abdomen; adult with malformed wings ranged from slight, moderate and severe; adults with poorly developed crumpled twisted wings and the wings were folded and extremely reduced in size; malformed antennae and legs (Figure 9).

The emerged adults from treated larvae appeared unable to fly, all of these malformations compared to normal moths emerged from untreated larvae (check experiment, Figure 10).

REFERENCES

[1] A.M. El-Hendawy, A.H. Alkubasi, K. El-Ghany, M.M. Shanab, *Polyhedron*, 12 (1993) 2343.
[2] P.K. Battacharya, *Proc. Indian. Acad. Sci. (Chem. Sci,),* 102 (1990) 247.
[3] D. Sriram, P. Yogeeswari, K. Madhu, *Bioorg. Med. Chem. Lett.*, 16, (2006) 876.
[4] D. Sriram, P. Yogeeswari, K. Madhu, *Bioorg. Med. Chem. Lett.*, 15 (2005) 4502.
[5] M.C. R-Arguelles , M.B. Ferrarii, F. Bisceglie, C. Pelizzi, G. Pelosi, S. Pineli, M. Sassi, *J. Inorg. Biochem*, 98 (2004) 313.
[6] T.B. Chaston, D.R. Richardson, *American J. Hematology*, 73 (2003) 200.
[7] P.V. Bernhard, P. Chin, P.C. Sharpe, J-Y.C. Wang , D.R.J. Richondson, *J. Biol. Inorg.*, 10 (2005) 76.
[8] C. Wang, M. Zhao, J. Yang, X. Li, S. Peng, *Toxicol. Appl. Pharm.*, 200 (2004) 229.
[9] O. Anderson, *Chem. Rev.*, 99 (1999) 2683.

[10] J.C. Craliz, J.C .Rub, D. Willis, J. Edger, *Nature*, 34 (1955) 176.
[11] J.R.D. Mechant, S. Clothia, *J. Med. Chem.*, 13 (1970) 333.
[12] V. Balasubramanian, N.S. Dixit, C.C. Patel, *Transition. Met. Chem.*, 5, 152 (1980).
[13] J. R. Dilworth, *Coord. Chem. Rev.*, 21 (1974) 29.
[14] L. Sommer, W.P.M. Gyee, D. Ryan, *Ser. Fac. Sci. Nature, Unin. Purk Ynianae, Burn*, 2 (1972) 115.
[15] M. Lever, *Anal. Chim. Act*a, 65 (1973) 311.
[16] Calvin, *Rev. Pure Appl. Chem.*, 15 (1965) 1.
[17] S.R. Cooper, M. Calvin, *Science*, 185 (1974) 376.
[18] D.K Jhnson, T.B. Murphy, N.J. Rose, W.H. Goodwin, L Pickart, *Inorg. Chem. Acta*, 67 (1982) 159.
[19] P. Vicini, M. Incerti, I. A. Doytvhinova, P. L. Colla, *Eur. J. Med. Chem.*, 41 (2006) 624.
[20] M. T. Cocco., C. Congiv, V. Lilliu,, V. Onnis, , *Bioorg. Med. Chem.*, 14 (2006) 366.
[21] S. M. Emam, F. A. El-Saied, S. A. Abou El-Enein and H. A. El-Shater, *Spectrochim. Acta Part A*, 72 (2008) 291.
[22] S. Abou El-Enein, F. A. El-Saied, S. M. Emam and M. A. El-Salamony, *Spectrochim. Acta Part A*, 71 (2008) 421.
[23] S. El-Tabl, F. A. El-Saied, W. Plass and A.N. El-Hakimi, *Spectrichim. Acta A*, 71 (2008).
[24] M. F. R. Fouda, M. M. E. Abd_Elzaher, M. M. Shakdofa. F. A. El- Saied, M. I. Ayad and A. S. El Tabl, *Transition Met. Chem.*, 33 (2008) 219.
[25] S. El-Tabl, F. A. El-Saied and A. N. Al-Hakimi, *J. Coord. Chem.*, 61 (2008) 2380.
[26] M. F. R. Fouda, M. M .Abd-Elzaher, M. M. Shakdofa, F. A. El- Saied, M. I. Ayad and A. S. El-Tabl, *J. Coord. Chem.*, 61 (2008) 1983.
[27] S. El-Tabl, F. A. El-Saied and A. N. Al-Hakimi, *Transition Met. Chem.*, 32 (2007) 689.
[28] S. A. Abou El-Enein, F. A. El-Saied, T. I. Kasher and A. H. El-Wardany, *Specrochim. Acta*, 67 (2007)737.
[29] S. El-Tabl, S. A. El-Enein, *J. Coord. Chem.* 57 (4) (2004) 281.
[30] H. M. El-Tabl, F. A. El-Saied, M. I. Ayad, *Synth. React. Inorg. Met. Org.* 32 (7) (2002) 1247.
[31] K. Nakamoto "Infrared and Raman Spectra of Inorganic and Coordination Compounds" 4th Edn. Wiley Interscience, New York (1986).
[32] K. Nakamoto "Infrared and Raman Spectra of Inorganic and Coordination Compounds" 3rd Edn. John Wileyand Sons, New York, (1970) 232-233.
[33] H. M. El-Tabl, F. A. El-Saied, *Synth. React. Inorg. Met-Org. Nano-Met. Chem*. 35 (2005) 243.
[34] M. Teotia, J.N. Gurthu, V.B. Rama, *J. Inorg. Nucl. Chem.* 42 (1980) 821.
[35] K. B. Gudasi, S. A. Patel, R. S. Vadvavi, R. V. Shenoy, M. Nethaji, *Trans. Met. Chem.*, 586 (2006) 31.
[36] El-Motaleb, M. Ramada, W. Sawodny, H.F. El-Baradie, M. Gaber, *Trans. Met. Chem.*, 211 (1997) 22.
[37] E.W. Einscough, A.M. Brodie, A.J. Dobbs, J. D. Ranford, J.M. Water, *Inorg. Chim. Acta*, 267 (1998) 27- 38.
[38] G. Ertem, D. X. west, J. P. Scovill, *Trans. Met. Chem.* 10 (1985) 131- 134.

[39] B. P. Lever, Inorganic Electronic Spectroscopy, Second edition, Elsevier Science Publishing Company, Amsterdam, 1984.
[40] Labadi, L. Horvath, G. Liptay, *J. Therm. Anal. Cal.* 83, (1) (2006) 247.
[41] Cukurovali, I. Yilmaz, *Trans. Met. Chem.* 31 (2006) 207.
[42] D.X. West, L.K. Pannell, *Trans. Met. Chem.* 14 (1989) 457.
[43] H.A. El-Boraey, *J. Therm. Anal. Cal*. 81 (2005) 339.
[44] D.X. West, A.K. El-Sawaf , G.A. Bain, *Trans. Met. Chem.* 23 (1998) 1.
[45] P.K. Singh, D.N. Kumar, *Spectrochim. Acta, Part A* 64 (2006) 853.
[46] S.A. Sallam, A.S.Orabi, B.A. El-Shetary , A. Lentz , *Trans. Met. Chem.* 27 (2002) 447-453.
[47] S. Yamada, *Coord. Chem. Rev*., 1 (1966) 415.
[48] B. N Figgs,. Introduction to ligand Field; Wiley: New York, 1966; (b) A.B.P. Lever, Inorganic Electronic Spectroscopy; 2nd Ed; Elsevier: Amsterdam, (1984).
[49] U. Casellato, D. Fregona, S Sitran, S. Tamburini, P. A. Vigato, *Inorg. Chim. Acta,* 95, (1984) 306.
[50] B.Murukan, K. Mohanan, *Trans. Met. Chem.,* 31 (2006) 441.
[51] G.M. Abu El-Reash, K.M. Ibrahim, M.M. bekheit, *Trans. Met. Chem.,* 15 (1990) 148.
[52] G. Venkatachalam, R. Ramesh , *Sectrochim. Acta Part A,* 61 (2005) 2081.
[53] S. El-Tabl, *Trans. Met. Chem.* 22, 166 (2002).
[54] S. Chandra, L. K. Gupta, *Spectrochim. Acta, Part A,* 60 (2004) 2411.
[55] S. Chandra, L. K. Gupta, *Spectrochim. Acta, Part A,* 62 (2005) 1102).
[56] Z.H. Abd El-Wahab, M.R. El-Sarrage, Spectrochim. Acta part A, 60 (2004) 217.
[57] V.P. Singh, A. Katiyar, Pesticide, Biochemistry and physiology ,92 (2008) 8.
[58] S.K. Sengupta, O.P. Pandey, A Rai, A. Sinha, Spectrochim. Acta Part A, 65 (2006) 139.

Smart Nanocomposites
Volume 1, Issue 2
ISSN: 1949-4823

COALESCENCE OF CARBON CLUSTERS IN A CATALYTIC NANODROPLET AND FORMATION OF CARBON NANOFIBRE

Sergey P. Fisenko*, Vladimir V. Martynenko, Stanislav I. Shabunya and Sergey A. Zhdanok
A.V. Luikov Heat and Mass Transfer Institute of the
National Academy of Science of Belarus,
15, P. Brovka St., Minsk, 220072, Belarus

ABSTRACT

Coalescence of carbon clusters, important stage of "vapor-liquid-solid" route of carbon nanofibre formation, was numerically simulated. Numerical simulation of diffusion equation of carbon atoms was made by means of finite elements method. For relatively large nanodroplet it was shown that due to coalescence the nanofibre diameter practically coincides with diameter of the catalytic nanodroplet. Also coalescence obligatory leads to the formation of the tubular nanofibre. It was established that the characteristic time of coalescence in finite volume of nanodroplet is about characteristic diffusion time. For relatively small nanodroplet cluster coalescence does not work effectively; therefore it gives explanation of the experimental observation of the absence of nanofibre formation for such nanodroplets.

Keywords: carbon diffusion, Kelvin effect, supersaturation, curvature radius, nanodroplet radius.
PACS: 64.70Dv, 68.70+w

1. INTRODUCTION

The fundamentals of the formation of carbon nanofibres via "vapor – liquid – solid" (VLS) route are relatively well established already [1-5]. Qualitatively these fundamentals can be described as follows. Gas flow supplies molecules of any hydrocarbon vapor to the surface of the catalytic nanodroplet, which has characteristic radius about ten nanometers.

* Corresponding author; email: fsp@hmti.ac.by

Typically, catalytic nanodroplets are situated on the solid surface of a substrate. Material of catalytic nanodroplets is Ni or Fe. Hydrocarbon molecules are decomposed on the catalytic surface, and carbon atoms diffuse through the catalytic nanodroplet. Under given temperature the saturated solid solution of carbon is obtained in the catalytic nanodroplet; let us denote the equilibrium solubility of carbon in the nanodroplet material as n_l. In particular, for Ni at temperature of 873 K $n_l = 1.9\ 10^{26}$ atoms/m^3. The characteristic time of the development of equilibrium solid solution τ_d [6] can be estimated as:

$$\tau_d \approx H^2/D,$$

where H is the height of the nanodroplet, D is the diffusion coefficient of carbon atoms in nanodroplet, exponentially depending on the temperature T. In the case nickel nanodroplet with H ~ 10 nm and at 800°C we estimated that $\tau_d \sim 10^{-5}$ s.

After some cooling of the substrate and nanodroplet, at least by 50- 100°C, a supersaturated solid solution appears in the catalytic nanodroplet. If supersaturation *S* of this solution is high enough a number of carbon clusters arise on the interfacial surface between catalytic nanodroplet and the substrate [1-5]. We determine *S* as

$$S = n / n_l(T),$$

where *n* is the actual number density of carbon atoms.

To note that substrate's properties substantially affects the nucleation of carbon clusters in nanodroplet [4-5]. Carbon clusters start to grow, supersaturation drops and in some time the coalescence of these clusters occurs [7]. During coalescence some smaller clusters and their groups vanish, other groups of clusters continue to grow and finally form a nanofibre, which grows out from the catalytic nanodroplet. Thus coalescence controls the final thickness of tubular nanofibre and its position relatively to the catalytic nanodroplet. The growth of a tubular carbon nanofibre was theoretically investigated within framework of the Stefan problem [4-5]. The cross- section of a tubular nanofibre is shown schematically in Figure 1.

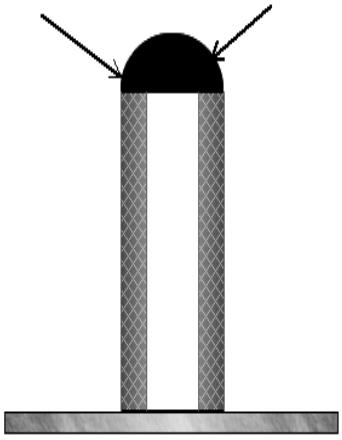

Figure 1. Sketch of a tubular nanowhisker.

Below the root regime of nanofibre growth is only considered because it is more often realized in experiments. It is worthy to emphasize that outer diameter of the nanofibre is practically equal to the diameter of relatively large catalytic nanodroplet. This circumstance is well established in many experimental researches, in particular in [1-3]. What are physical reasons of this experimental fact?

The aim of this paper is to answer this simple question. For this aim we investigate the contribution of coalescence of carbon clusters in catalytic nanodroplet into the formation carbon nanofibres.

The paper is organized as follows: at first we discuss features of carbon diffusion during development of saturated solid solution in a catalytic nanodroplet. In other words we consider the very first stage of formation of nanofibre; the development of the saturated solid solution into nanodroplet. Next, we present simulation results of the final stage of the coalescence of carbon clusters and groups of clusters. In last chapter we summarize our results. The theoretical consideration of nucleation rate of clusters was given earlier in [4, 5].

2. SIMULATION OF DIFFUSION PROCESS IN THE CATALYTIC NANODROPLET

Diffusion of carbon atoms in catalytic nanodroplet is the basic process for formation carbon nanofibre. Let us consider the axis-symmetric catalytic nanodroplet (Figure 2) and calculate the diffusion of carbon atoms in this nanodroplet. Thus we will consider very important first stage of nanofibre formation, namely, the development of the saturated solid solution of carbon.

To note also that the assumption about the axial symmetry is often valid for the vast majority of nanodroplets used in many experiments; it permits one to reduce the three-dimensional problem to the formally two-dimensional diffusion problem. In this case, the diffusion equation [6] looks like:

$$\frac{\partial n(r,z)}{\partial t} = D\left[\frac{\partial^2 n}{\partial z^2} + \frac{1}{r}\frac{\partial}{\partial r}\left(r\frac{\partial n}{\partial r}\right)\right]. \qquad (1)$$

It is useful to make transition to dimensionless spatial variables in Eq. (1):

$$\hat{z} = z/H \text{ and } \hat{r} = r/H,$$

and, correspondingly, to a new time variable $\hat{t} = tD/H^2$. Numerically, τ_d is approximately equal to 0.025. Additionally, for the number density of carbon, we use a new normalized variable: $\hat{n} = n/n_1$.

Thus for the diffusion problem the range of the variable $\hat{n}$ is between 1 and 0, for the variable $\hat{z}$ the range is between 1 and 0, while the variable $\hat{r}$ varies from 0 to d/2H. Using new variables we have a convenient form of the diffusion equation. Also, bearing in mind the meaning of new variables, we omit the sign ”roof” over these variables:

$$\frac{\partial n(r,z)}{\partial t} = \left[\frac{\partial^2 n}{\partial z^2} + \frac{1}{r}\frac{\partial}{\partial r}\left(r\frac{\partial n}{\partial r} \right) \right] \quad (2)$$

For the problem under investigation the boundary conditions for Eq. (2) are written below. For the curve 1 in Figure 2, which represents the surface of the catalytic nanodroplet adjacent to the gas phase, the boundary condition is:

$$n = 1. \quad (3)$$

For curve 2 in Figure 2, which represents the surface of the catalytic nanodroplet adjacent to the substrate, where the condition for non-permittivity of the interface boundary is:

$$\frac{\partial n(r,0)}{\partial z} = 0 . \quad (4)$$

For r=0 the symmetry condition is fulfilled:

$$\frac{\partial n(0,z)}{\partial r} = 0 \quad (5)$$

For different shapes of catalytic nanodroplets the transient diffusion problem was solved by the Finite Elements Method (FEM) [8, 9], which belongs to the family of variational methods of mathematical physics. In such methods unknown functions are represented as a sum of basis functions. Expansion coefficients of an unknown function relatively to the basis functions are calculated by minimizing the specific functional [8].

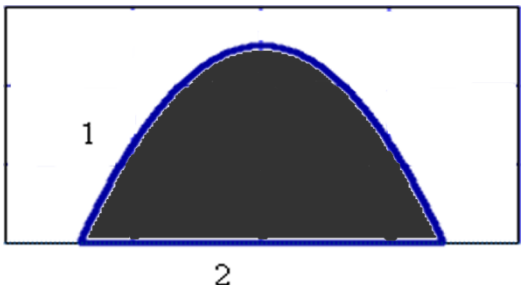

Figure 2. Nanodroplet shape.

For the ratio d/H = 2 the level line n = 0.9 is shown at different instant moments in Figure 3. We see the symmetrical pattern of carbon propagation in all directions. The reason for this is in the perfect symmetrical shape of the nanodroplet. The characteristic dimensionless diffusion time is about 0.4. The diffusion flux has its the maximal value at very first time instant of the process. Obviously if there is diffusion sink in the vicinity of the outer surface of nanodroplet, due to huge gradient the diffusion flux goes to it. This simple observation is important for understanding of physics of formation of carbon nanofibre. Carbon clusters play a role of diffusion sinks.

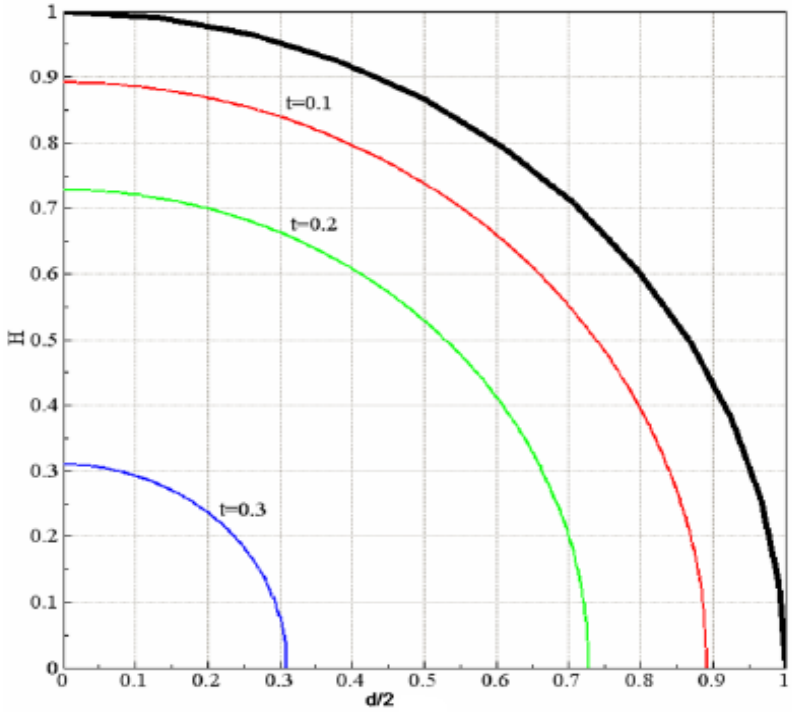

Figure 3. Establishment of equilibrium carbon distribution in semispherical nanodroplet.

Simulation of diffusion problem for different shape of catalytic nanodroplets did not discover unusual features. Practically characteristic dimensionless diffusion time has the same value. Thus the first stage of carbon nanofibre is quite simple one. The final stage of carbon nanofibre formation is nonlinear one, and it is considered in the next chapter.

3. Simulation of Final Stage of Coalescence of Carbon Clusters

After ending the diffusion saturation process and substrate cooling of the supersaturated solid solution appears in the catalytic nanodroplet. Nucleation creates carbon clusters on the interfacial surface between the nanodroplet and the substrate. The characteristic radius of these initial clusters is about one nanometer [4]. As it was mentioned above diffusion flow is not uniform one in the nanodroplet! The clusters which are closer to outer shell of the nanodroplet (right corner in Figure3) grow faster than the clusters near central part of the interface. The diffusion interaction between clusters and the Kelvin effect make another contribution to carbon nanofibre formation. To remind that equilibrium number density of carbon atoms over the carbon cluster n_e with two curvature radii R_1 and R_2 is described by the formula [10]:

$$n_e = n_1 \exp\left[\frac{\sigma v_a}{kT}\left(1/R_1 + 1/R_2\right)\right], \qquad (6)$$

where σ is the surface tension between carbon and material of catalytic nanodroplet, k is Boltzmann's constant and v_a is the volume per carbon atom in condensed matter, $v_a \approx 10^{-29}$ m^3. In particular, the effective flux of carbon atoms J on a cluster is directly proportional to the densities difference

$$J \sim D(n - n_e).$$

If the number density of carbon atoms n is smaller than n_e the cluster begins dissolve and $J<0$.

There are currently numerous difficulties in solving 3D diffusion problem for arbitrary positions of the number of growing carbon clusters. In order to avoid these computational troubles and nevertheless to reach some insight in this paper we limit by ourselves to the consideration of cylindrically symmetrical case when we can consider already formed carbon semi-tores. Grown clusters gave the origin of these non-perfect semi-tores. The sketch of a single semi-tore is shown in Figure 4.

For every such semi-tore the radius-vector of central line of the semi-tore on the interface R_2 can approximately play the role of the second curvature radius. Then it immediately follows from expression (6) that at any given supersaturation S the semi-tore with larger R_2 has larger growth rate because the value of n_e decreased.

Assumption about semi-tores formation and the expression (6) gives the simple explanation of the experimental fact that nanofibre diameter practically coincides with nanodroplet diameter. Indeed, for such position we have the most favorable condition of the semi-tore growth. In turn, internal radius of nanofibre is also limited by the Kelvin effect, described by the expression (6). For given value of number density of carbon atoms we have the condition that flux is equal to zero on internal part of the semi-tore. Thus changing the number density of carbon atoms in the same catalytic nanodroplet we can exert control over important geometrical parameters of nanofibre.

Aiming to illustrate how the coalescence works for nanofibre formation here we present the simulation of the scenario with two carbon semi-tores inside catalytic nanodroplet. The equation governing the change of radius vector R_2 based on the law of mass conversation of carbon and in accepted approximation is:

$$\frac{dR_1}{dt} = \frac{Dm}{2\pi R_1^2 \rho_c} \iint_{\Sigma} \nabla n \vec{k} ds, \qquad (7)$$

where m is the mass of carbon atom, ρ_c is the mass density of carbon in the cluster, $\vec{k}$ is normal vector to the surface of the cluster, Σ is the surface of the cluster. It can be seen from right hand side of the Eq. (7) that distribution of carbon in whole nanodroplet affects the semi-tore growth. Actually Eq. (7) is averaged form of the Stefan problem for the semi-tore growth [6].

The radius vector R_2 of the first semi-tore is equal to 7.1 nm, the smaller semi-tore has radius- vector R_2 equal to 3.1nm. For the sake of simplicity the initial curvature of R_1 of both semi-tores are equal to each other, R_1 = 0.8 nm while $D = 10^{-14}$ m^2/s. To note that in this chapter we don't use dimensionless variables, except for the number density of carbon atoms.

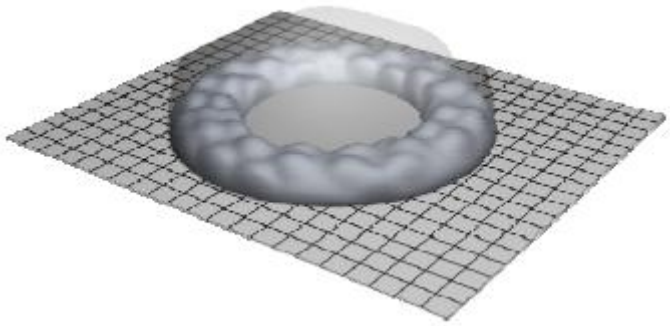

Figure 4. Sketch of the single semi-tore formed by grown carbon clusters.

The evolution of parameter R_1 for these two semi-tores in the catalytic nanodroplet is shown in Figure 5. It was obtained as solution of the diffusion equation (1) by means of FEM with corresponding boundary conditions. Additionally we assume that semispherical shape of semi-tores is conserving all the time, see Eq. (7). This assumption permits drastically to reduce the computation time, but camouflages some important details. Our simulation is under progress without this assumption.

It is obvious from curves in Figure 5 that semi-tore with larger R_2 the curvature R_1 steadily grows, but in the case for the tore with smaller R_2 curvature R_1 slowly decreases, up to time instant when it totally disappears at t = 0.045 s. No doubts that at coalescence stage the additional consideration of some clusters at the central part interface does not change our main result. From physical point of view the decreasing the curvature R_2 means also that a new source of free carbon atoms appear in catalytic nanodroplet.

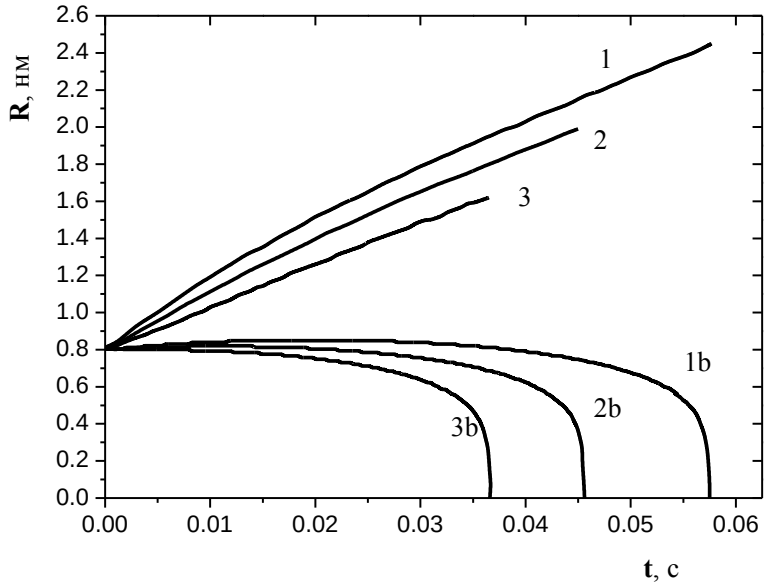

Figure 5. Parameter R_1 versus time. Curve 1 for R_1 = 3.1 nm, curve 2 for R_1 = 7.1 nm.

Curves 1 and 1b for S = 1.45, curve 2 for S = 1.4, curve 3 for S = 1.35.

For the same case the snapshot of dimensionless number density of carbon is shown in Figure 6.

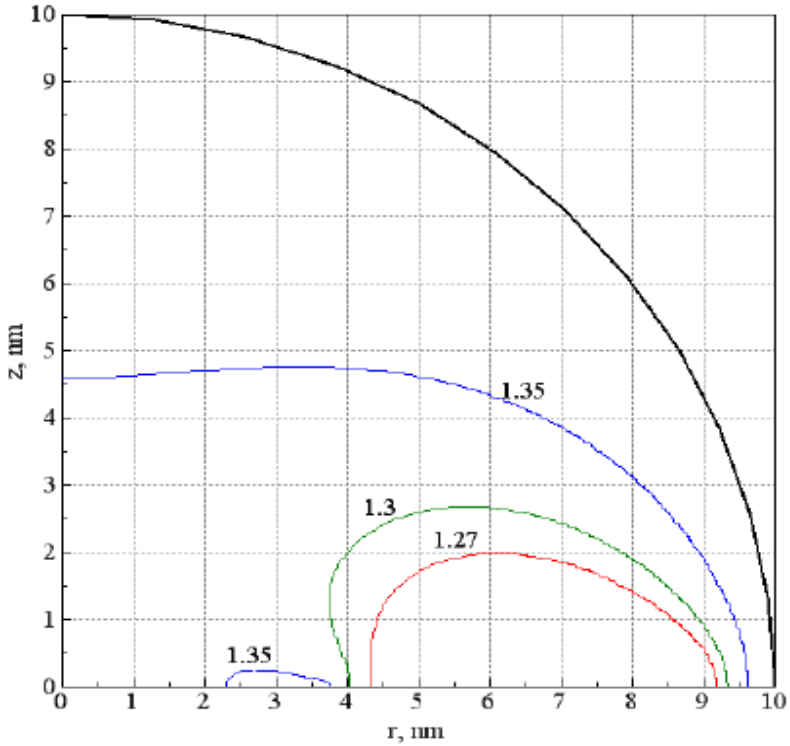

Figure 6a. Spatial distribution of carbon at nanodroplet. t = 37 ms.

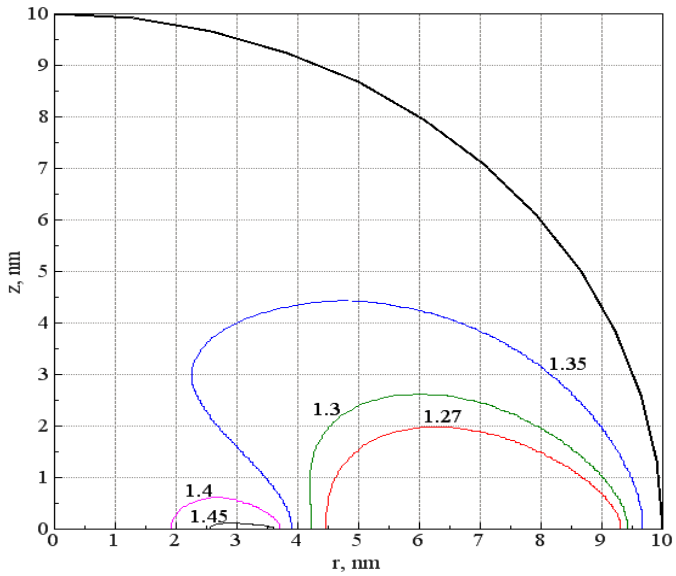

Figure 6b. Spatial distribution of carbon at nanodroplet . t = 43 ms.

To note that on the outer shell of catalytic nanodroplet the number density is constant and it is equal to 1.4, therefore S = 1.4. It is obviously that semi-tores growth leads to decreasing

of the number density of carbon atoms in nanodroplet. Correspondingly, dissolving semi-tore increases locally the number density of carbon atoms. At t = 37 ms level lines of the distribution of carbon atoms are shown in Figure 6a. It can be seen that the growth of larger semi-tore creates the gradient of carbon number density in catalytic nanodroplet. Remind that at this time instant R_2 is about 1.75 nm. At later time instant, t = 43ms several the level lines of the carbon distribution are shown in Figure 6b. It is clearly seen the sharpening of gradients and dissolving of the smaller semi-tore. The growth of the larger semi-tore is feed by carbon atoms from whole nanodroplet but mainly from outer shell. In the case that the number density of carbon is equal to 1.4 on outer shell of nanodroplet; nanodroplet radius is equal to 10 nm.

It is important to emphasize again that dissolving central semi-tore is the source of free carbon atoms in the nanodroplet. The rate of dissolving is controlled by diffusion of carbon atoms. Characteristic time τ of dissolving of the smaller semi-tore in the finite volume of nanodroplet we can estimate on the basis of our calculations as following [7]: $\tau \approx \tau_d$.

CONCLUSION

We performed simulation of carbon atoms diffusion in catalytic nanodroplet using the Finite Element Method (FEM). It was established that the most intensive diffusion processes take place near the edge of the outer shell of the nanodroplet with the substrate. Thus this place is most favorable for nucleation and growth of carbon clusters, which are formed after formation of supersaturated solid solution in catalytic nanodroplet [2, 4, 5].

It was shown also that the Kelvin effect [10], expression (6), and diffusion interaction between clusters and their groups suppress the growth of clusters and their group in the central part of the interface separating of catalytic nanodroplet and substrate. Only the semi-tore formed by clusters in a vicinity of the nanodroplet shell has the fastest growth rate. Another clusters and even semi- tores dissolve. Thus through the Kelvin effect the coalescence is responsible for experimental fact that the diameter of carbon nanofibre practically coincides with the nanodroplet diameter [1-3]. It is worthy to emphasize that coalescence and, correspondingly, dissolving a semi-tore and clusters in central part of nanodroplet obligatory leads to formation of a tubular nanofibre. In addition it is worth to note that dissolving clusters in the central part of nanodroplet is a substantial source of free carbon atoms for nanofibre growth.

To mention also that the Kelvin effect is the reason why small nanodroplets do not create carbon nanofibre, see figures in [1]. The small curvature of whole nanodroplet means that supersaturation S in nanodroplet should be high enough in order to create a semi-tore as the origin of a nanofibre. If the supersaturation is not so high the formation of the semi-tore via coalescence does not take place!

Characteristic time of dissolving clusters and their groups in the central part of the nanodroplet is about τ.

Therefore, we can say coalescence leads to the development of single the semi-tore from carbon clusters. It is an essential step in formation of nanofibre because it determines its geometrical structure, diameter and the width of nanofibre wall.

REFERENCES

[1] Verissimo, C.; Aguiar, M. R.; Moshkalev S. A. *J. Nanoscience and Nanotechnology*. 2009, *vol. 9*, 4459-4466..
[2] Moshkalev, S.; Verissimo, C. *J. App. Phys*. 2007, *vol.102*, (044303).
[3] Merkulov, I. A.; Klein K. L.; Simpson, M. L. *J. App. Phys.* 2009, *vol.105*, (064305).
[4] Fisenko, S. P.; Borovik, F. N. *Tech. Phys*., 2009, *vol.45*, 246 - 252.
[5] Borovik, F. N.; Fisenko S. P. *Tech. Phys. Lett*., 2007, *vol*. *33*, 151–153.
[6] Morse, P. M. C.; Feshbach, H. *Methods of Theoretical Physics*, McGraw- Hill Science: New York, 1999.
[7] Lifshitz, E. M.; Pitaevskii, L. P. *Physical Kinetics*, Pergamon: Oxford, 1981.
[8] Fletcher, C. A. J. *Computational Galerkin Method*. Springer: New York, 1984.
[9] Sewell, G. *Analysis of Finite Element Method: PDE/Protran*, Springer: New York, 1985.
[10] Landau, L. D.; E. M. Lifshitz. *Statistical Physics*, Pergamon: Oxford, 1980.

Smart Nanocomposites
Volume 1, Issue 2
ISSN: 1949-4823

AN IMPROVED CNTFET GALOIS CIRCUIT DESIGN AS A BASIC MVL FIELD

***Peiman Keshavarzian*[*1, 2] *and Keivan Navi*[2]**
[1]Computer and Mechatronic Engineering Department,
Science and Research Branch, Islamic Azad University, Tehran, Iran
[2]Nanoelectronic and Quantum Computing Laboratory,
Shahid Beheshti University, GC, Tehran, Iran

ABSTRACT

Carbon nanotube field effect transistors (CNTFETs) are being studied extensively as a possible successors to silicon MOSFETs. Implementable CNTFET circuits have operational characteristics to benefit from the advantage of using MVL in voltage mode. Ternary-valued logic (TVL) Galois field has two basic operators (addition and multiplication) which have been used to implement all the ternary logical functions. In this paper we use CNTFET transistors to implement an improved Galois filed basic operators. In This design we control all the three stable voltage values on the output node by controlling all the appropriate carbon nanotube field effect transistors. Consequently, the simulations in the novel Galois field circuit design, result in an improvement in the Galois filed circuit parameters such as delay, power and power delay product.

Keywords: Galois Field, CNTFET, TVL, MVL circuit design.

1. INTRODUCTION

In an era of nanotechnology, molecular devices are becoming promising alternatives to silicon technology, Nanotechnology is a novel field of research that cuts across many fields – electronics, chemistry, physics and biology which analyzes and synthesizes structures in the nano scale (10^{-9} m) such as nano particles, nanowires, Nanotubes, etc. Carbon Nano Tube (CNT) has attracted attention in recent years not only for its relatively small dimensions and unique morphologies, but also for its potential for implementation in many emerging technologies.

* Address correspondence to keshavarzian.p@srbiau.ac.ir, navi@sbu.ac.ir

CNT is one of the several cutting-edge emerging technologies within nanotechnology with high efficiency and a wide range of applications in many different streams of science and technology [1]. Nano-circuits based on CNTs such as CNT Field Effect Transistors (CNTFETs) show big potential for consuming less power and be much faster than available silicon based FETs [2, 3, 4, 5].

The geometry dependant threshold voltage of carbon nanotube FETs (CNTFETs) has been often used to design ternary logic family [6, 4]. MVL circuits can reduce the number of operations necessary to implement a particular mathematical function and further, have an advantage in terms of reduced area. In comparison to the fastest binary counterpart, Chip area and power dissipation have been shown to be reduced using efficient MVL implementation [6, 8, 9]. The outline of this paper is as follows. In section 2, Galois filed outlines are described, in section 3 CNT field effect transistor (CNTFET) are inspected, in section 4 the latest CNTFET Galois Field circuit design as the state of the art design are introduced. In section 5 an improved Galois Field circuit design, its implementation and its result are presented. Conclusions are presented in section 6.

2. GALOIS FIELD

Various fields with their unique characteristics and operators are described in MVL logics such as Literal, Galois, LukaSiewicz, Godel, Kleene-Bochvar. Each field consists of a number of functions and basic operators such as addition and multiplication operators in the Galois field. The MVL functions should be implemented by a combination of the basic operators in the unique field area [7, 8].

While Binary Galois field circuits have been investigated by many researchers not much work has been done on MVL versions of such circuits. CNTFET is primarily concerned with circuits operating over three elements such as ternary Galois field (GF3) [8].

A Galois field (F, +, *) is a set with two operations that are closed with respect to that set. We will call them addition and multiplication [8, 9]. A certain number of axioms ensure the existence of neutral (zero for the addition operation and one for multiplication) and inverse elements with respect to both operations as well as commutativity and distributivity of multiplication with respect to addition, define the structure of the field. The operations "+" and "*" together with the set F are said to form groups (F, +) and (F- {0},*), where the group is defined as a set with the operation that is closed with respect to that set. The axioms of a group guarantee that there is a unique neutral element, as well as the inverse element for each member of the group.

All fields such as Galois fields contain a finite number of elements. In the case of a field with a prime number of elements, both operations are defined as usual modulo addition and multiplication. In other cases, the operations are more complex. They are defined with respect to irreducible polynomials over a simpler field. This means that if we have a field with p^n elements, then the operations are defined using some irreducible polynomial of degree n over the field with p elements. The TVL Galois field multiplier and adder have been introduced as they are inspected in table 1.

For each combination of inputs, unique and appropriate stable output should appear in the output node to define the Galois field multiplier and adder.

Table 1. Galois field multiplier (a) Galois field adder (b)

(a)

*	0	1	2
0	0	0	0
1	0	1	2
2	0	2	1

(b)

+	0	1	2
0	0	1	2
1	1	2	0
2	2	0	1

3. CARBON NANOTUBE FIELD EFFECT TRANSISTORS

The first carbon-nanotube field-effect transistor (CNTFET) was reported in 1998 [10]. At that time, it was not clear how these devices worked, but subsequent progress has been rapid.

Today, sophisticated transistor structures demonstrating the potential for high performance are appearing and sophisticated modeling techniques are being used to understand their physics. A CNT was positioned so as to bridge two gold or platinum electrodes [11, 12], which acted as the source and drain of the FET (Figure 1).

Carbon nanotube field effect transistors (CNT-FET) present a large potential as building blocks for specific applications in the area of nanoelectronics, carbon nano-electronics which may be faster than conventional Si, SiGe, GaAs, or InP semiconductor technologies that are predicted to have a cut off frequency of 80 GHz/L, where L is the gate length in microns, opening up the possibility of a ballistic THz nanotube transistor [13]. Field effect transistor devices with carbon nanotube conducting channels have been developed and used for biosensing and biodetection [14] and have exhibited strong memory effects [15, 16].

Applications in the biosensing field are illustrated with three examples: the investigation of the interaction between devices and biomolecules, the electronic monitoring of biomolecular processes and attempts to integrate cell membranes with active electronic devices [14]. The contact between metal and CNT can be of Ohmic or Schottky type [17, 18, 12] and the CNT used in the transistor was a semiconducting single wall CNT that can be switched from metallic to insulating state by modulation of the gate voltage.

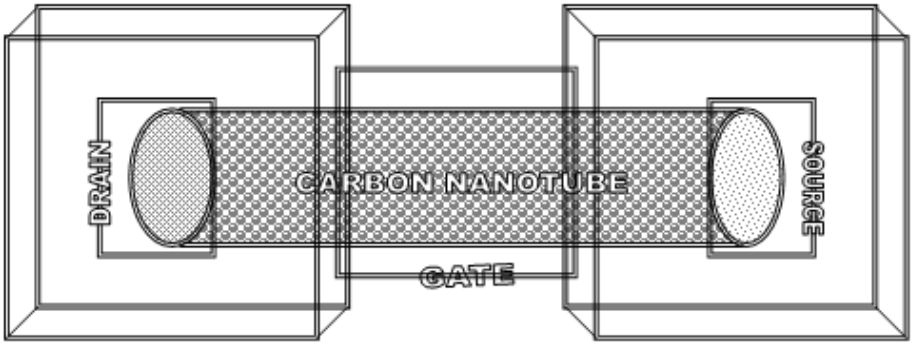

Figure 1. CNTFET.

There are two types of carbon-nanotube transistors that are being extensively studied. One is a tunneling device (Figure 2 (a)) that works on the principle of direct tunneling through a Schottky barrier at the source–channel junction.

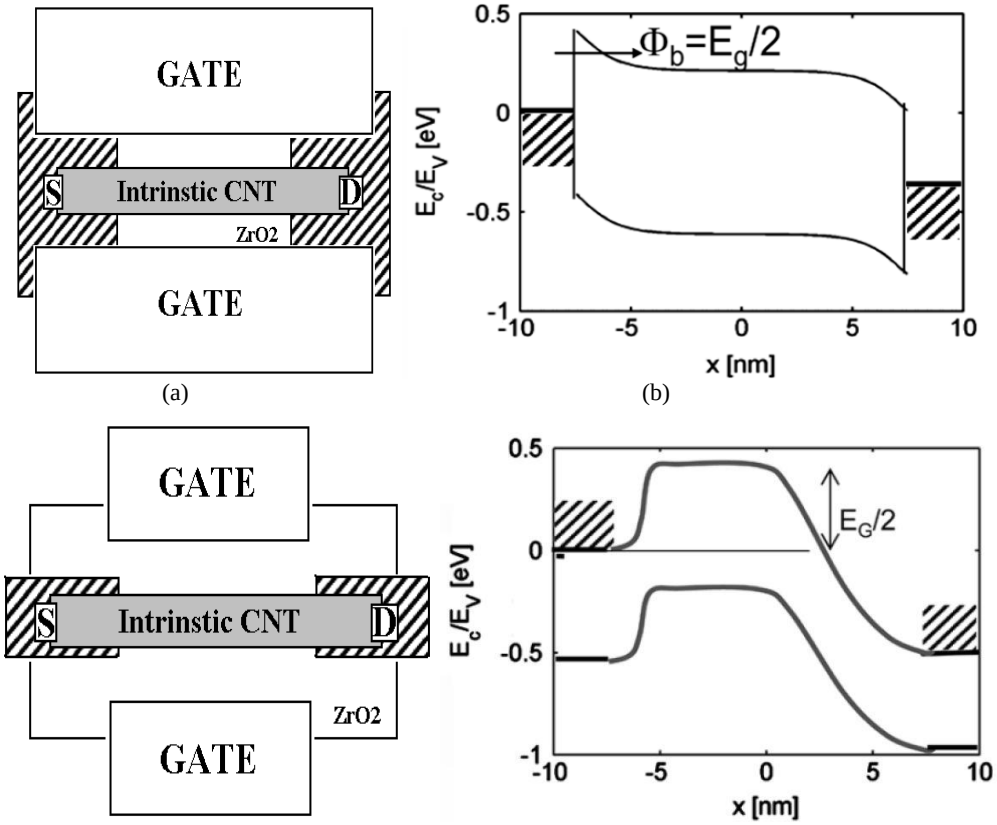

Figure 2. Two types of single wall CNTFETs.

The barrier width is modulated by application of the gate voltage so that transcend-uctance of the device is dependent on the gate voltage.

Two important characteristics of these nanotube transistors are worth mentioning: energy barrier and Schottky-barrier. CNTFETs exhibit strong ambipolar characteristics and this constrains the use of these transistors in conventional CMOS logic families.

To overcome these disadvantages associated with Schottky barrier CNTFETs, there have been attempts to develop CNTFETs which would behave like normal MOSFETs. These attempts have met significant success so far with an enormous potential. The MOSFET-like CNTFET (Figure 2 (b)) operates on the principle of barrier height modulation by application of the gate potential.

More recently, Guo et al. have presented numerical studies on such MOSFET-like CNTFETs [18] and it is evident that: 1) unlike Schottky-barrier field-effect transistors (FETs) the MOSFET-like CNTFETs have unipolar characteristics; 2) absence of the Schottky barrier reduces OFF leakage current; 3) they have more scalability compared to their Schottky-barrier counterparts; and 4) in the ON state the source-to-channel junction has no Schottky barrier and thus a significantly higher ON current. Further, it can be assumed that

transportation through these CNTFETs is ballistic. In this paper, we will consider the non-Schottky-barrier MOSFET-like unipolar CNTFET with ballistic transport as our device of interest. Hereafter in this paper the abbreviation CNTFET will be used to denote such a MOSFET-like device unless otherwise stated (Figure 2 (b) shows the band diagram of this device).

The source Fermi level for a degenerately doped source can be derived from the conduction band edge. Inside the intrinsic channel, the Fermi level is in the middle of the bandgap. An important property of these CNTFETs is that the bandgap is inversely proportional to the diameter of nanotube as (eq.1) [1, 19].

$$E_G = \frac{0.84}{d(nm)} ev. \qquad (eq1)$$

Thus, for the conduction to start, the barrier at the source channel junction that has to be surmounted is. $EG/2\,(e.g.,=\Delta 1)$

As the barrier height determines the threshold potential of a FET, the threshold voltage of the CNTFETs can be expressed as (eq.2)

$$V_{TH} = \frac{0.42}{d(nm)} ev. \qquad (eq2)$$

This geometry-dependent threshold voltage has been exploited in this study to obtain CNTFETs that turn on at different voltages depending on their diameters. It is worth mentioning that the circuit realization of the ternary logic family involves dual- transistors. CNTFETs provide an opportunity to obtain two functional behaviors by using two different tube diameters. CNTFETs provide the unique opportunity of being controlled by changing the carbon-nanotube diameter. Therefore, in this paper, we have used a dual-diameter CNTFET-based design for the ternary logic implementation to present TVL Galois field circuit design.

4. STATE OF THE ART CNTFET GALOIS FIELD CIRCUIT DESIGN

Since many multiple-valued circuits over ternary Galois field can be synthesized using addition and multiplication operations in the Galois field that were described before, thus these basic operators can be used in multiple-valued implementations whenever they are applied.

In simpler word, the MVL functions should be demonstrated by a combination of the basic operators in the Galois field.

In the latest Galois field circuit design (Figure 3) for the ternary logic implementation we use CNTFET transistors with resistive pull-ups [8]. The Vdd voltage in the state of the art Galois field design is 0.9 volt and consequently our nanotube transistors have two different diameters with two different threshold voltages.

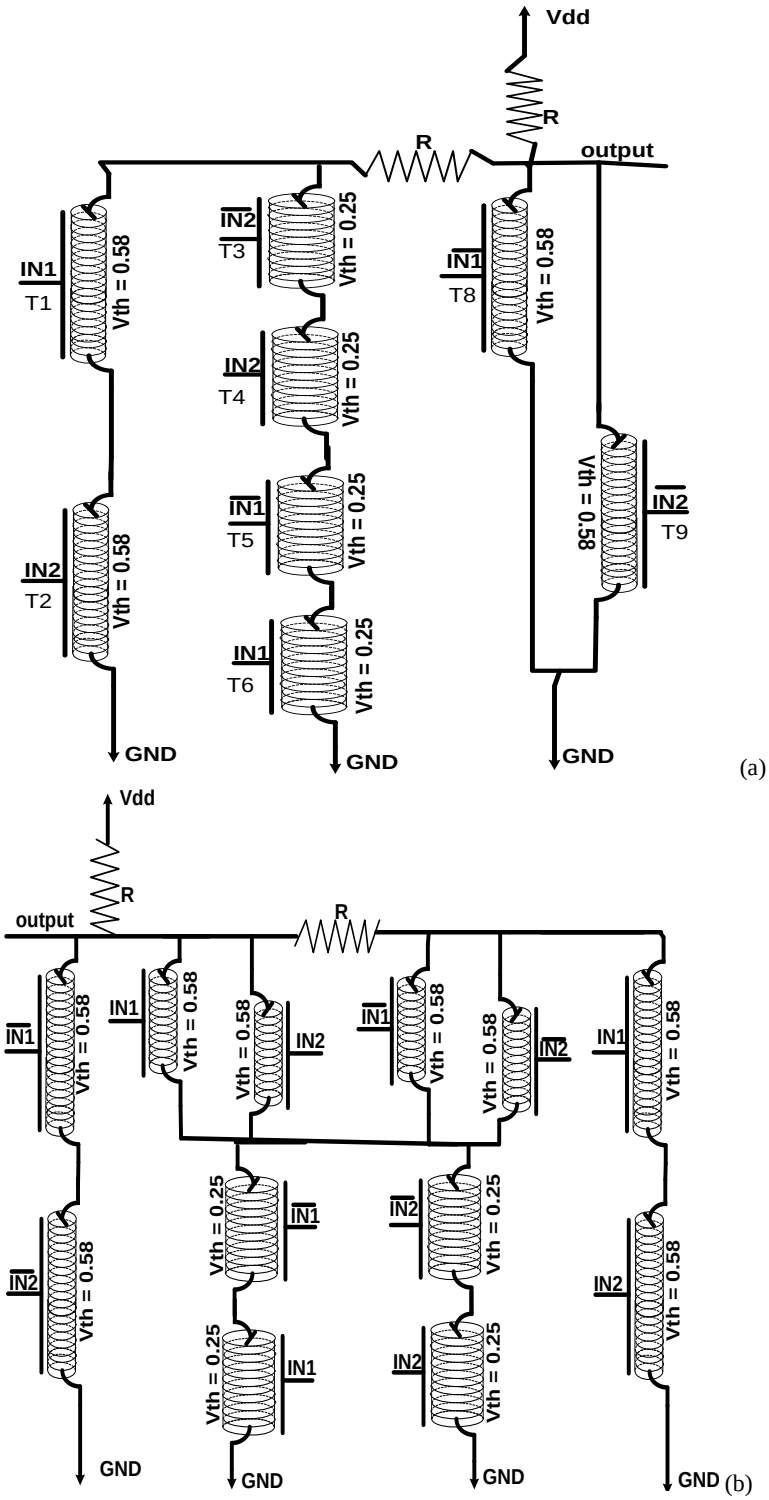

Figure 3**.** Efficient Galois field circuit design. a) Galois field Multiplier. b) Galois field Adder. (CNTFETs contains its Threshold voltage).

According to the input voltage level and two different threshold voltages as $V_{th1}=0.25^{V}$ and $V_{th2}=0.58^{V}$, we will have three different states. If $V_{input} < V_{th1}=0.25^{V}$, both transistors will be turned off. If input voltage rises to $V_{th1}=0.25^{V} < V_{input} < V_{th2}=0.58^{V,}$ just one of the transistors will be turned on. If input voltage rises further to $V_{input} > V_{th2}=0.58^{V}$, both transistors will be turned on. Hence analyzing the latest design shows that the output voltages are the result of voltage divisions which are produced by combination of these resistors and active transistors.

For each combination of inputs only one predominant output path is activated. Therefore through our circuit design structure the output was held at the expected stable voltage by appropriate voltage division.

In the efficient Galois field circuit design, by using carbon nanotube field effect transistors, we have achieved a significant improvement in the number of circuit elements as well as chip area, power and speed. Also the latest design exhibit the efficient field area, through Galois filed adder and multiplier in the multiple valued- logic using carbon nanotube field effect transistors.

5. AN IMPROVED CNTFET GALOIS CIRCUIT DESIGN AS A BASIC MVL FIELD

The state of the art Galois field circuit design included N-CNTFETs with resistance pull up. In the previous design we employed two threshold voltages (0.25 and 0.58) to detect all the ternary values and also we used two nanotube diameters to describe these thresholds. In the previous design the pull up resistance encountered our design with the permanent output value (V_{dd}) In order to approach the expected output values we have to control this permanent value by controlling all the other circuit elements. This problem would deteriorate our circuit design parameters such as delay, power and also our power delay product.

The Galois field operators use the novel circuit designs to control all the paths by detecting each combination of inputs. Even the previous permanent pull up voltage has been controlled by using P-CNTFETs to achieve the best performance. We approach an improvement in the circuit parameters such as delay, power and power delay product by controlling all the output paths so we could restrict affecting persistent V_{dd} value to the output. We add P-CNTFETs modules in both designs (Galois filed multiplier and adder) to appropriately activate our "Vdd to the output" path.

For each combination of inputs, only one predominant output path is activated. Therefore through our circuit design structure, the output is held at the expected stable voltage by appropriate voltage division. The vdd voltage in the novel Galois field design is 0.8 volt and consequently our nanotube transistors have two different diameters with two different threshold voltages. According to input voltage level and two different threshold voltages as $V_{th1}=0.25^{V}$ and $V_{th2}=0.58^{V}$, we will have three stable states.

If $V_{input} < V_{th} =0.25^{V}$, all the N-CNTFET transistors will be- turned off and P-CNTFETs will be turned on and when the input voltage rises to $V_{th}=0.25^{V} < V_{input} < V_{th}=0.58^{V,}$ only the N-CNTFET transistors with $V_{th} =0.25^{V}$ will be turned on and the other N-CNTFET will be turned off. The P-CNTFETs with $V_{th} =0.58^{V}$ will be turned on and the others will be turned off. If input voltage rises further to $V_{input} > V_{th}=0.58^{V}$, all the N-CNTFET transistors will be

turned on and all the P-CNTFETs will be turned off. Hence analyzing our new circuit designs shows that output voltages are the result of voltage divisions which are produced by combination of these resistors and active transistors [8]. When in1 or in2 are less than 0.25, in the novel multiplier circuit design (Figure 4), T7 or T8 will be turned on and the output reaches zero due to the only active connection to the ground. When in1 and in2 are more than 0.25, T9 or T10 will be turned on and these will activate the connection to the highest voltage (Vdd).

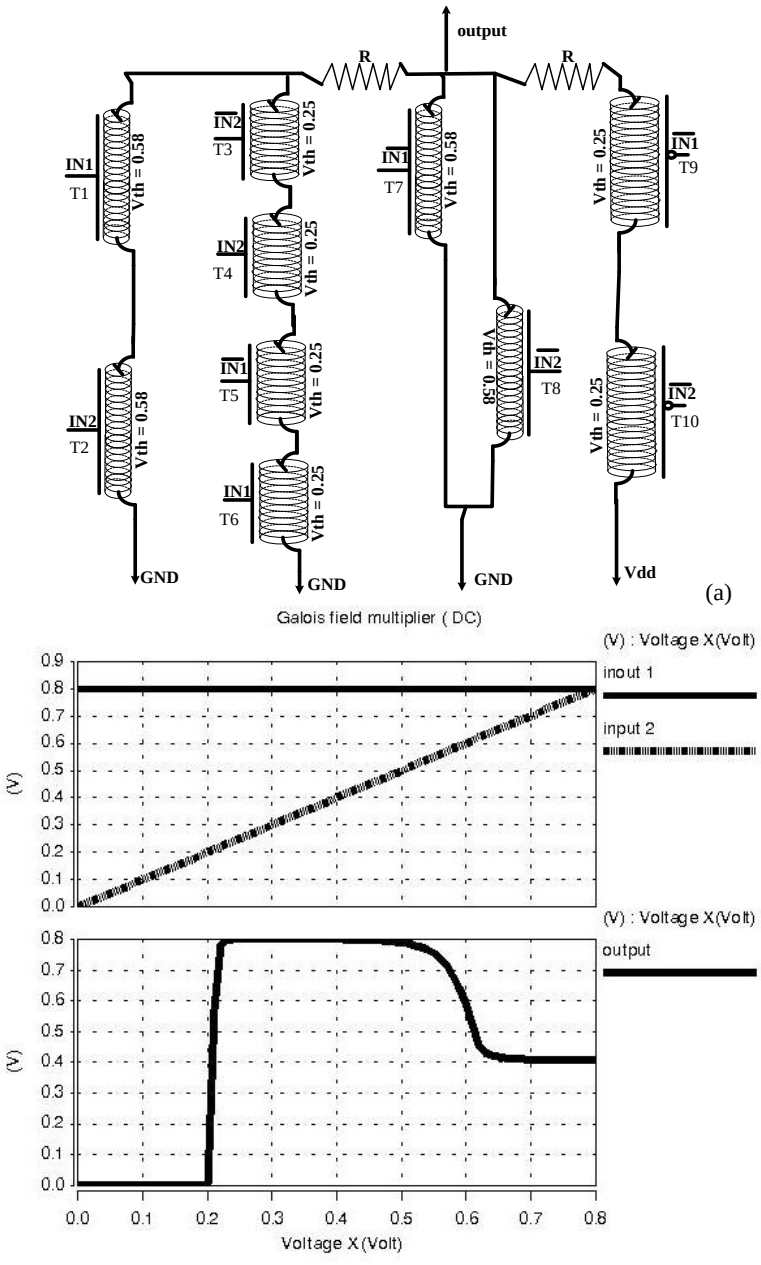

Figure 4. (a) Improved Galois field multiplier circuit design (b) DC simulation results sample.

If (in1, in2) = (1, 1) or (in1, in2) = (2, 2) then we have the other active connections to the ground so that because of the resistors, we have a voltage division to achieve the expected voltage on the output node (0.25<V<0.58). Obviously if (in1, in2) = (1, 2) or (in1, in2) = (2, 1) only the connection to the highest voltage is activated and the others are disabled so that we have Vout = Vdd. In the novel Galois field adder circuit design (Figure 5,6) when (in1, in2) = (2, 1) or (in1, in2) = (1, 2) or (in1, in2) = (0, 0) , due to the active transistors, connection to the ground will be activated and the output reaches zero.

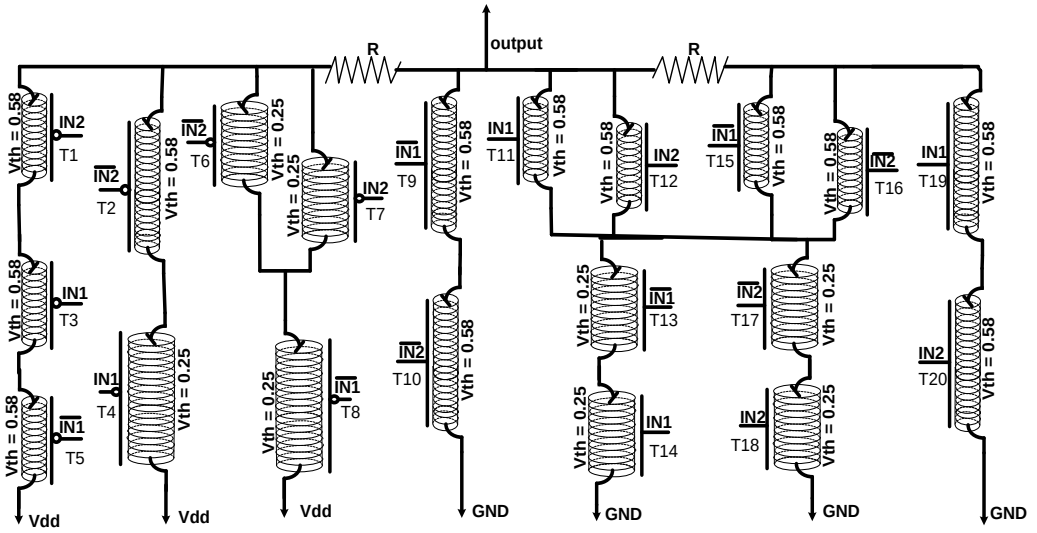

Figure 5. Improved Galois field adder circuit design.

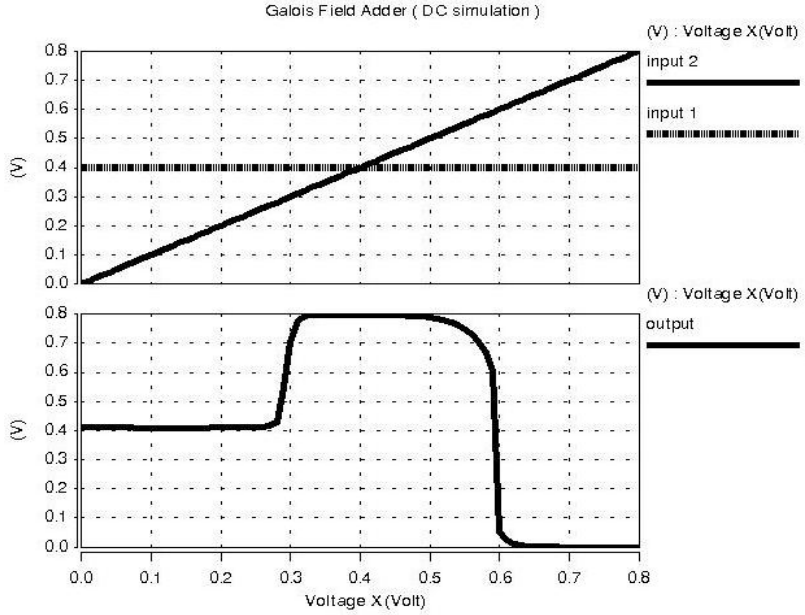

Figure 6. A sample of Galois field adder DC simulation result.

Table 2. The comparison results

Vdd= 0.8v	Average Delay (PS)	Average Power (μW)	PDP (J)
Galois field adder [8]	52.9322	5.4082	2.8626* 10 -16
Improved GF Adder	48.1699	4.0227	1.9377* 10 -16
Galois field multiplier [8]	46.5516	6.5086	3.0298* 10 -16
Improved GF multiplier	18.3156	3.3245	6.0890* 10 -17

In the other combination of inputs, we will have the active connection to the highest voltage (vdd) and also for (in1, in2) = { (1,0) , (0,1) , (2,2) } in addition we will have the other active connection to the ground so that these connections apply a voltage division resulting in ($0.25 < v < 0.58$) on the output node. For the other combination of inputs which we only have one connection to the highest voltage (V_{dd}), V_{out} will be equal to V_{dd}.

In this paper, a compact model of CNTFETs has been used and simulations have been carried out using HSPICE. The details of the modeling technique are available in [1, 19]. Short channel MOSFET like CNTFETs are of particular interest because they are shown to provide near ballistic current, thereby indicating maximum performance. Simulation results show degradation in terms of power consumption, delay and improvement in speed. Also, we have achieved an improved ternary Galois filed circuit design. We compared our simulation results with the state of the art Galois filed CNTFET circuit design [8]. We present the improved Galois field operators as the basic operators in the basic multiple valued-logic field (Galois field), The comparison results are illustrated in table 2.

CONCLUSION

In this paper we have presented an improved Galois field circuit design using carbon nanotube field effect transistors. We have achieved a significant improvement in delay, power and power delay product. This design controls all the three stable output voltage values by controlling the appropriate carbon nanotube field effect transistors. To achieve an improved Galois field circuit designs, all the CNTFETs have been used to activate the adequate guidance path and to disable all the other paths to the output, thus we have three stable voltage values on the output node.

In the novel Galois field adder we have achieved more than 34% improvement in terms of average delay and also more than 9.8% improvement in terms of average power resulting in more than 47% improvement in the power delay product, consequently. In the novel Galois field multiplier average delay and the average power are 1.95 times and 2.5 times better than the previous work respectively.

REFERENCES

[1] J. Deng; H.S. P. Wong; A Compact SPICE Model for Carbon-Nanotube Field-Effect Transistors Including Nonidealities and Its Application - Part I: Model of the Intrinsic Channel Region. *IEEE Trans. Electron Devices*, 2007, 54, 3186-3194.

[2] K. Navi; M. H. Moaiyeri; R. F. Mirzaee; O. Hashemipour; B. M. Nezhad; Two new low power full adders based on majority-not gates. *Microelectronics journal*, 2009, Elsevier,40,126.

[3] K. Navi; M. Rashtian; A. Khatir; P. Keshavarzian; O. hashemipour; High Speed Capacitor-Inverter Based Carbon Nanotube Full Adder. Springer, *Nanoscale Res Lett*. , 2010, 5, 859–862.

[4] K. Navi; A. Momeni; F. Sharifi; P. Keshavarzian; "Two novel ultra high speed carbon nanotube Full-Adder cells", *IEICE Electron*. Express, 2009, 6, No. 19, 1395-1401.

[5] K. Navi; F. Sharifi; A. Momeni; P. Keshavarzian; Ultra High Speed CNFET Full-Adder Cell Based on Majority Gates. *IEICE TRANS*. , to be appeared .

[6] P. Keshavarzian; K. Navi; efficient carbon nanotube lukasiewicz circuit design. In *Proceedings of 3'rd international conference on nanostructures*, 2010, kish island, 1022-1025.

[7] A. Raychowdhury; K. Roy; Carbon- Nanotube-Based Voltage-Mode Multiple-Valued Logic Design. *IEEE Tran. ON Nanotechnology*, 2005, 4, No. 2 , 168.

[8] P. Keshavarzian; K. Navi; Efficient carbon nanotube Galois field circuit design. *IEICE Electronic Express*, 2009, 6, No. 9, 546.

[9] P. Keshavarzian; K. Navi; Universal ternary logic circuit design through carbon nanotube technology, *Int. J. Nanotechnol*., 2009, 6, Nos. 10/11,942-953.

[10] S.J. Tans et al., Room-temperature transistor based on a single carbon nanotube. *Nature*, 1998, 393, 49.

[11] Ph. Avouris; R. Martel; V. Derycke; J. Appenzeller; Carbon nanotube transistors and logic circuits. *Physica B*, 323 , 2002, 6–14.

[12] J.S. Hwang et al, Electronic transport properties of a single-wall carbon nanotube field effect transistor with deoxyribonucleic acid conjugation. *Physica E: Low-dimensional Systems and Nanostructures*, 2008, 40, No. 5, 1115-1117.

[13] Peter J. Burke; AC performance of nanoelectronics: towards a ballistic THz nanotube transistor. *Solid-State Electronics*, 48, 2004, 1981–1986.

[14] G. Gruner; Carbon nanotube transistors for biosensing applications. *Anal. Bioanal Chem*, 2006, 384, 322–335 review.

[15] D.J. Yanga; Qing Zhang; S.G. Wanga; G.F. Zhong; Memory effects of carbon nanotube-based field effect transistors. *Diamond and Related Materials*, 2004, 13, 1967–1970.

[16] J. B. Cui; R. Sordan; M. Burghard; K. Kern; Carbon nanotube memory devices of high charge storage stability. *Applied Physics Letters*,2002, 81, No. 17,3260-3262.

[17] M. Pourfath, et al ; Numerical Analysis of Coaxial Double Gate Schottky Barrier Carbon Nanotube Field Effect Transistors. *Journal of Computational Electronics* , 2005, 4, 75–78.

[18] J. Guo; A. Javey; H. Dai; S. Datta; M. Lundstrom; Predicted Performance advantages of carbon nanotube transistors with doped nanotubes source/drain. *Phys. Rev. B, Condens. Matter*, 2003, cond-mat/0 309 039.

[19] J. Deng; H.S. P. Wong; A Compact SPICE Model for Carbon-Nanotube Field-Effect Transistors Including Nonidealities and Its Application - Part II: Full Device Model and Circuit Performance Benchmarking. *IEEE Trans. Electron Devices*, 2007, 54, 3195-3205.

Smart Nanocomposites
Volume 1, Issue 2
ISSN: 1949-4823

INFLUENCE OF NICKEL-SiO_2 SUBSTRATE INTERACTION AND ANNEALING TEMPERATURE ON THE CNTS GROWTH BY THERMAL CVD

C. Verissimo* and S. A. Moshkalev
Center for Semiconductor Components – CCS,
State University of Campinas – UNICAMP,
Campinas, SP, CEP 13083-870, Brazil

ABSTRACT

The interaction between metal catalyst and the substrate can influence the growth of carbon nanomaterials in thermal chemical vapor deposition experiments. According to our observations, the oxidation of catalyst particles can be favored under specific conditions by the silica layer over the silicon wafer used as substrate decreasing the catalyst activity. The temperature of the catalyst thermal pre-treatment can also change the catalyst particles properties (shape, size distribution and crystallographic phase) and influence the final characteristics of the carbon nanomaterials such as the crystallinity and density. The use of both, methane and acetylene, as carbon precursor gases also affected the material grown and showed different nucleation time for the catalyst particles.

Keywords: Carbon nanotubes; Chemical vapor deposition; Methane and acetylene decomposition; Electron microscopy.

1. INTRODUCTION

Carbon nanotubes (CNTs) have shown great potential for technological applications due to their extraordinary properties [1-4]. However, the development of nanodevices based on carbon nanostructures aiming the fabrication of nanoelectronic devices, nanoelectromechanical systems, nanosensors, etc., depends on a number of factors. For example, the capability to control the characteristics of carbon nanomaterials during the growth process is still a challenge to be overcome before the fabrication of CNTs based devices in large scale [5-7].

* Corresponding author. Tel.: +55 19 3521-5332; fax.: +55 19 3521-5177. E-mail address: carla@iqm.unicamp.br (C. Verissimo).

Chemical vapor deposition (CVD) process associated with metal catalyses has been considered the most interesting method to obtain carbon nanostructured materials due to the possibility to control experimental parameters. Catalytic CVD process also presents experimental conditions compatible with silicon technology which is very significant for the nanodevices development [6,8]. In the catalytic CVD process, the catalyst is a very important parameter for the CNTs growth since carbon precursor molecules decompose on a metal catalyst surface to yield carbon atoms available for graphitization and further carbon nanotube formation. This suggests the significance of the catalyst in the CNTs formation via CVD. The catalyst can be formed *in situ*, along with the carbon nanotube growth, in a floating chemical vapor deposition process [9,10]. On the other hand, catalyst particles can be prepared previously, by using different syntheses approaches of metal nanoparticles followed by their dispersion over a substrate [11]. Another procedure is the deposition of a metal thin film over a substrate followed by an thermal treatment (annealing) leading to the formation of supported metal catalyst particles [5,6,12].

Literature shows that different catalytic metals under the same CVD conditions can produce carbon nanomaterials presenting different characteristics [5,13-15]. Ichi-oka et al. reported the growth of well-crystalline double-walled carbon nanotube, multi-walled carbon nanotube and irregular carbon nanofiber according to the metal species used as catalyst during the growth experiments [16]. Martin-Gullon et al. [17] also showed the important influence of metal specie in the final characteristics of the carbon material grown using different catalysts. Consequently, each catalytic metal can demand specific experimental conditions to form a specific carbon nanostructure. The metal catalyst features, such as chemical state, composition, initial metal film thickness, metal particle size, etc., can promote differences in the catalytic behavior, as well as the interaction between the catalyst and a specific substrate [13-21]. It has also been found that the catalyst pretreatment can influence the metal catalyst capability, resulting in the either improvement or deficiency of the carbon nanotube growth [21-24]. The catalyst can also be responsible for the growth density of the carbon nanotubes by controlling its: i) reactivity, ii) deposition on specific pre-fabricated positions by lithography, iii) dispersion over an either flat or particulate substrate. Another approach to control the CNT density during the syntheses involves the use of hydrocarbon gases as carbon precursors presenting varied reactivity. In such case, more reactive precursors lead to a higher density of CNT growth [15]. In the work of Siegal et al. [25], the use of carbon precursor gases presenting higher heat of formation (more reactive gases) resulted in an increased density of carbon nanotubes grown.

In this work, the effect of the interaction between nickel catalyst and silica support layer thermally grown over silicon wafers on the final carbon nanomaterial characteristics has been investigated. The influence of the thermal pre-treatment (annealing process) of the catalyst, the growth temperature and the carbon precursor gases on the nucleation time, catalyst activity and CNTs density were also evaluated.

2. EXPERIMENTAL

Thin metal film of Ni with a thickness of 6 nm was deposited using electron beam evaporation onto silicon wafers covered by a 50 nm thick thermally grown silicon oxide

layer. Further, silicon wafers coated by metal film were cut in small pieces (5x5 mm^2) and annealed in a quartz tube furnace at 500 or 700 ^oC in a H_2 flow of 400 sccm during 30 minutes. After the annealing process, the hydrogen was replaced by NH_3 flow of 400 sccm during 5 minutes. Then, the temperature was raised to 800-950 ^oC, and the synthesis was started by addition of 25-100 sccm of CH_4 for 30 minutes. After the first 5 minutes of the synthesis, NH_3 was replaced by the same flow of H_2.

During the main growth phase, the H_2:CH_4 gas ratios were 4:1, 8:1 or 16:1. For the growth using acetylene, the temperature was increased to 800 ^oC after the annealing process and 10 sccm of C_2H_2 were introduced inside the furnace for 1, 2 or 30 minutes (H_2:C_2H_2 gas ratio = 40:1).

High resolution scanning electron microscopy (SEM) was performed by using a FEG-SEM JSM 6330F microscope (LME, LNLS-Campinas, Brazil). A HR-TEM JEM 3010 URP microscope operating at 300 kV and with a point resolution of 0.17 nm was used for high resolution transmission electron microscopy (HR-TEM) and x-ray energy dispersive spectroscopy (EDS) (LME, LNLS-Campinas, Brazil). Differential thermal analyses (DTA) was performed using a TA equipment, model SDT Q600, over the 30-1500 °C temperature range with a heating rate of 10 °C min^{-1} under argon flow of 100 mL min^{-1}.

Raman spectroscopy was performed employing a Renishaw System 3000 Raman Imaging Microscope, using the 632.8 nm line of a He-Ne laser. Grazing incidence x-ray diffraction (GIXRD) measurements were performed in the x-ray diffraction beamline of the Brazilian Synchrotron Light Laboratory (LNLS-Campinas, Brazil) by using an incidence angle of 1.5° while the detector was swept to vary 2θ (λ = 1.5417 Å).

3. RESULTS AND DISCUSSIONS

3.1. Annealing Effect on the Catalyst Particle Formation

Nickel was used as catalyst metal for the growth of carbon nanotube by catalytic chemical vapor deposition method. After the deposition of 6 nm thick Ni film over silicon wafer covered by thermally grown silicon oxide, to prevent nickel silicide formation [26], the metal film was thermally treated at 700 ^oC to generate nickel nanoparticles. TEM image obtained for nickel particles after air exposition showed core-shelled particles due the formation of a nickel oxide layer around the metal particles (Figure 1).

The EDS spectrum (not shown) obtained for the 5 nm thick external layer of the particles presented peaks related to the existence of both nickel and oxygen elements indicating the formation of nickel oxide around the particles. The spectrum of the core particle region showed only the peak related to nickel. Malesevic et al. [21] also showed the formation of nickel oxide by XPS studies around nickel particles formed after the annealing of a thin film deposited over a SiO_2/Si substrate and air exposition.

As already demonstrated in the literature, nickel oxide is not an efficient catalyst to convert carbon precursor molecules in carbon nanotubes [27]. Consequently, metal thin films were annealed under a reducing atmosphere (H_2 flow) just before CNTs growth, aiming the removal of the undesired oxide layer [28].

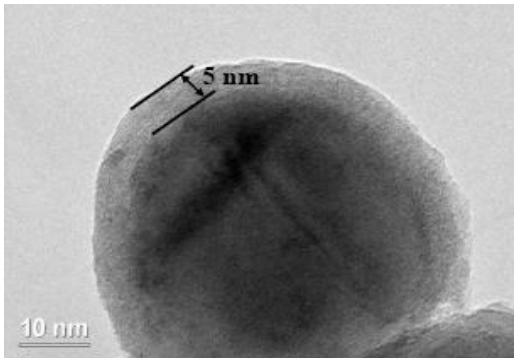

Figure 1. TEM image of a nickel particle presenting a 5 nm thick external layer of nickel oxide formed after air exposition.

To study the annealing process, thermal treatments using Ni film with a thickness of 6 nm were performed at different temperatures (500, 700 or 900 ^{o}C) under hydrogen flow. Usually, thermal treatment can change metal films promoting morphological instabilities and leading to a final break up of the film into isolated particles on the substrate. The formation of metal particles from metal films deposited onto ceramic materials, such as oxides and nitrides, has been observed for several decades. This phenomenon, called agglomeration, is a thermally activated process and takes place because ceramic materials have a lower surface energy compared to metals. Consequently, metal films tend to reduce their area to decrease the surface energy of the system by forming spherical particles. Thus, nickel film form nickel particles on the silicon oxide layer to reduce the surface energy of the system under heating. This process occurs by surface diffusion of the atoms and it is improved with the temperature increase [29-31].

Scanning electron micrograph obtained for the Ni film annealed at 500 ^{o}C shows the Ni film broken in pieces of different sizes, ranging from 0.02 to 1.00 μm or more (Figure 2(a)). This was observed near to the edge of the SiO_2/Si substrate and suggests the nickel particles generation from the metal film rupture followed by the atomic nickel thermal motion leading to a broad particle size distribution. In the central part of the substrate, continuous Ni film was found presenting failures similar to holes probably originated by the thermal motion of the Ni atoms (Figure 2(b)). This phenomenon seems to be the initial stage of the particle formation in the central region of the substrate. Apparently, the metal film in the substrate edge suffers different effects compared to the central region and 500 ^{o}C was not enough to break the metal film and promote the formation of Ni particles all over the substrate. The prior particle formation in the edges can be related to the smaller adhesion between metal film and substrate near to the film border among others instabilities [32-34], and indicates the existence of different mechanisms for nickel particle formation taking place over the substrate.

For the annealing performed at 700 ^{o}C, isolated round (disk-like) particles were formed presenting diameters from 10 to 100 nm, which suggests the Ni film assumed a liquid-like behavior at 700 ^{o}C. This liquid-like behavior can leads to the formation of metal particles possessing Gauss-like size distribution as observed in Figures 3 (a) and (c) [35]. SEM images also showed a different size distribution of the particle in the edge compared to the center of the substrate.

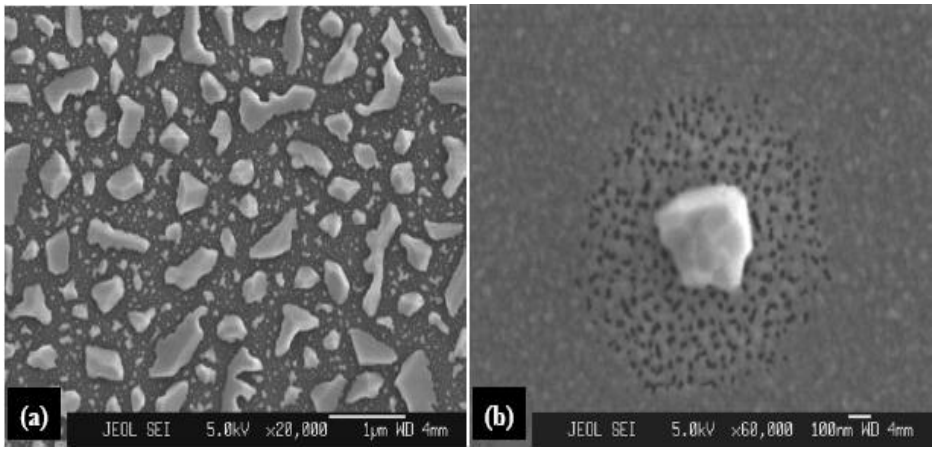

Figure 2. Scanning electron micrographs of 6 nm thick Ni film annealed under H_2 flow for 30 minutes at 500 ^{o}C: (a) substrate edge: Ni film broken in pieces of different sizes and presenting facets; (b) central part of the substrate: holes in the continuous Ni film and the initial stage of the particle formation.

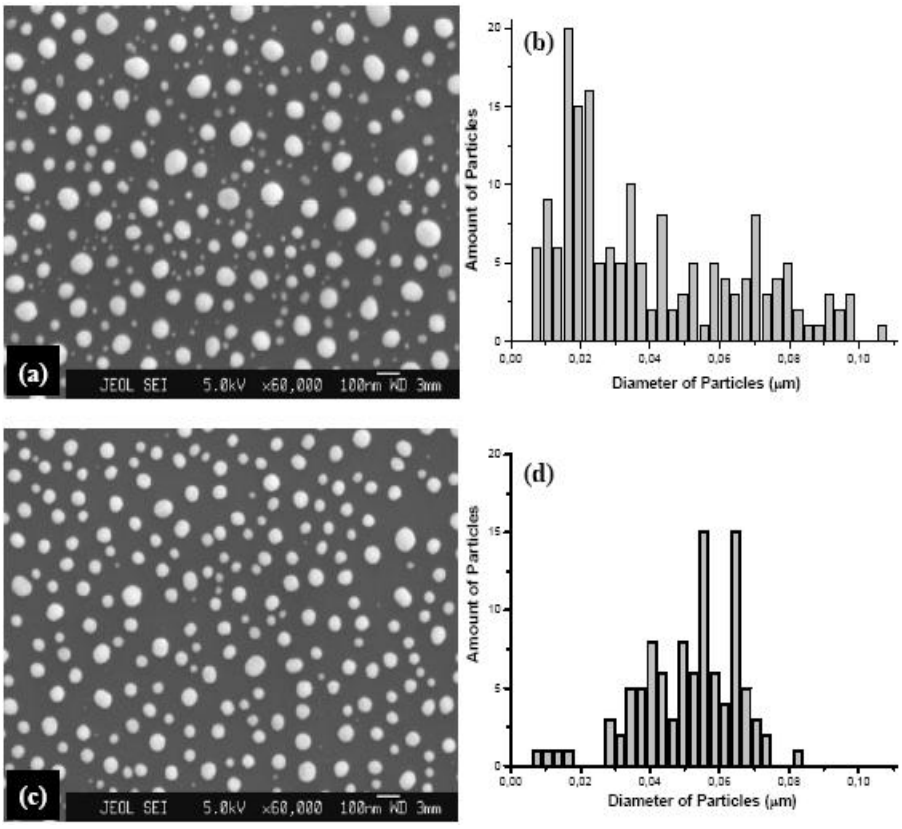

Figure 3. Scanning electron micrographs of 6 nm thick Ni film annealed under H_2 flow for 30 minutes at 700 ^{o}C: (a) edge and (c) center of the substrate. Histograms show a narrower distribution of metal particle diameters in the central region of the substrate: histogram (d) shows 96 % of particles with diameters between 27-74 nm against 43 % in histogram (b).

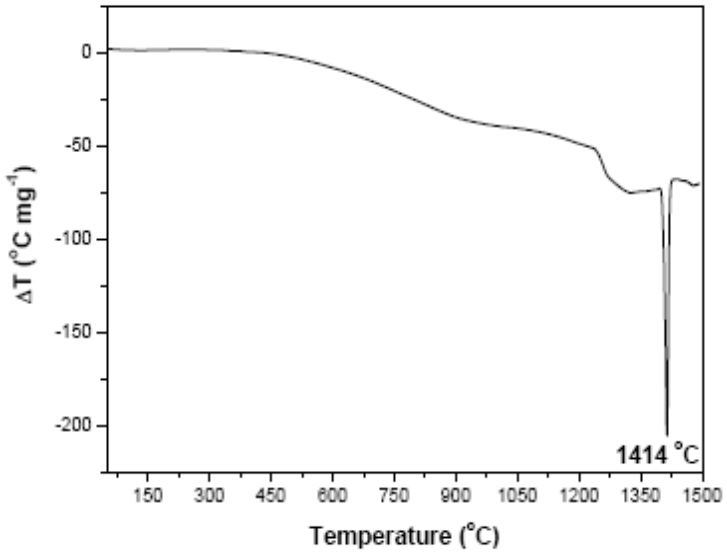

Figure 4. DTA curve of 6 nm thick Ni film deposited over a SiO_2/Si substrate.

A narrower distribution of the metal particle diameters was found in the central region of the substrate (histograms showed in Figures 3 (b) and (d)). According to observations made for Ni film annealed at 500 ^oC, metal film apparently breaks initially in the border of the substrate leading to the formation of metal particles presenting very broad size distribution. This phenomenon probably is related to the different metal particle size distribution observed in different regions of the substrate for the Ni film annealed at 700 ^oC. In spite of the reduced dimension of the metal film (6 nm thick) and the rounded particle formation, the nickel film do not melts at the annealing temperature (700 ^oC). According to DTA analyses, an initial softening of the thin Ni film takes place around 450 ^oC whereas the melting point is observed at 1414 ^oC (Figure 4), which is very similar to the melting temperature for bulk material (1453 ^oC) [12,36,37].

Grazing incident x-ray diffraction pattern for Ni particles formed at 700 ^oC presented peaks at 44.2, 51.5 and 75.9^o (2θ) corresponding to face centered cubic (fcc) Ni structure [38]. In the case of Ni particles obtained at 500 ^oC, the diffraction pattern showed peaks at 29.8, 34.3, 41.6, 42.7 and 45.1^o (2θ) (Figure 5). Therefore, in addition to the influence on the particles morphology, different annealing temperatures also promoted the formation of different metal crystallographic phases.

For Ni film annealed at 900 ^oC, the amount of larger particles was increased compared to the metal film treated at 700 ^oC (see Table 1). Since the percentage of smaller particles decrease after the thermal treatment at 900 ^oC, a coarsening process is taking place at higher temperature. The narrower size distribution of metal particles in the central region of the substrate was also observed by SEM images (Figs. 6(a) and (c)). The multimodal size distribution of nickel particles observed in Figure 6(a), histogram (b) (edge region of the substrate), is once more believed to be related to the differences occurred during the metal film rupture process and further particle formation. GIXRD pattern of this sample also showed the fcc Ni structure for the metal after heating at 900 ^oC (not shown).

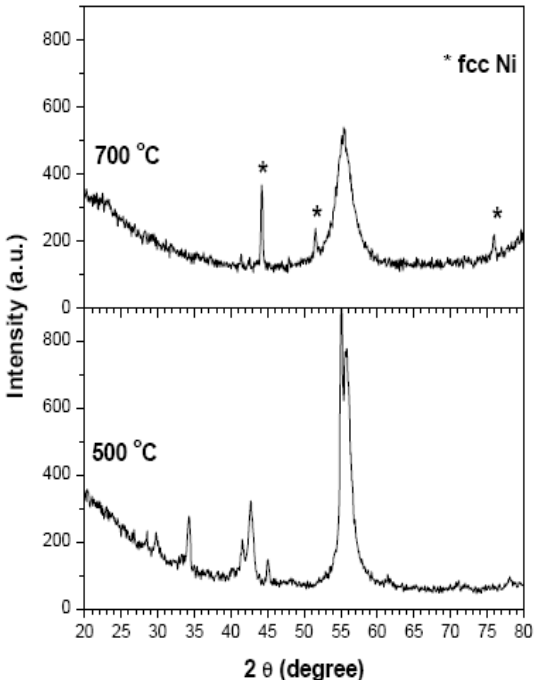

Figure 5. GIRXD pattern of 6 nm thick Ni film annealed under H_2 flow for 30 minutes at 500 and 700°C. The intense peak around 55-60° (2θ) is related to silicon substrate.

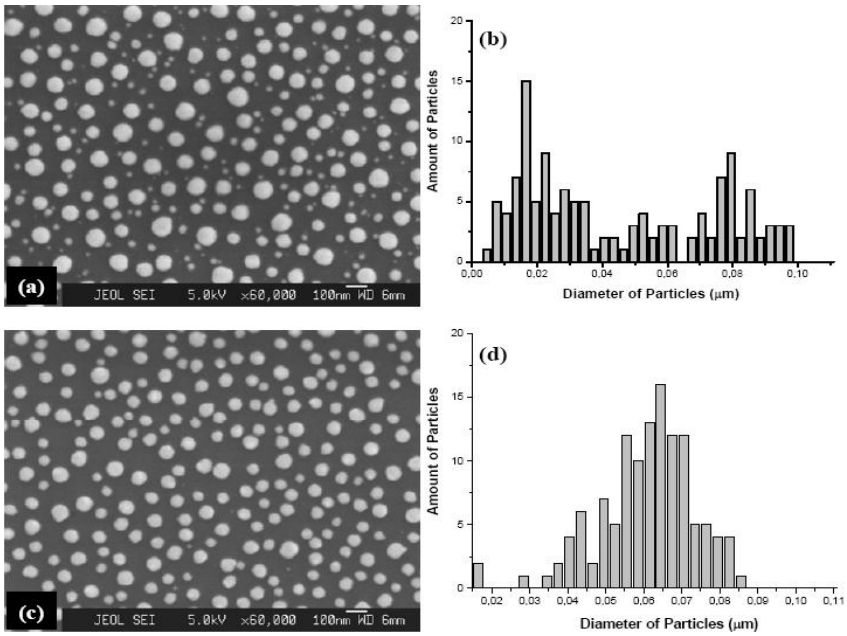

Figure 6. Scanning electron micrographs of 6 nm thick Ni film annealed under H_2 flow for 30 minutes at 900 °C: (a) edge and (c) center of the substrate. Histogram (d) shows a narrower distribution of metal particle diameters in the central region of the substrate compared to the substrate edge (histogram b).

Table 1. Distribution of nickel particle diameters obtained from Ni film with a thickness of 6 nm thermally treated at 700 and 900 °C: comparison between histograms d presented in Figures 3 and 6

Annealing Temperature	Ni Particle Size (S)		
	S < 27 nm	27 nm < S < 74 nm	S > 74 nm
700 °C	44 %	43 %	13 %
900 °C	38 %	35 %	27 %

3.2. CNTs Growth

Figure 7 presents SEM images for CNTs samples grown using Ni film annealed at 500°C. After the annealing, the substrate containing supported catalysts particles was pushed to a furnace zone already heated at 900 °C and methane was introduced. Scanning electron micrographs show a lack of control in the formation of CNTs, been possible to notice several differences in the carbon nanomaterial, such as smooth or rough surface, tubes with or without metal inside, besides the formation of carbonaceous materials. GIXRD pattern (Figure 8) shows the transformation of the unknown Ni phase observed at 500 °C to fcc structure after the heating at 900 °C along with graphite and diamond phases formation [38]. Probably, the simultaneous occurrence of metal particles with different characteristics in the initial step of the growth process, such as size, shape and aspect ratio, are responsible for the growth of diverse carbon materials [39].

The CNTs growth performed from Ni film annealed at 700 °C presented a higher control on the characteristics of the carbon material obtained. SEM images show the formation of only carbon nanotubes independently of the H_2:CH_4 gas ratios employed during the growth process at 900 °C, with diameters ranging from 30 to 130 nm and lengths that can reach values upper to 10 μm (Figure 9).

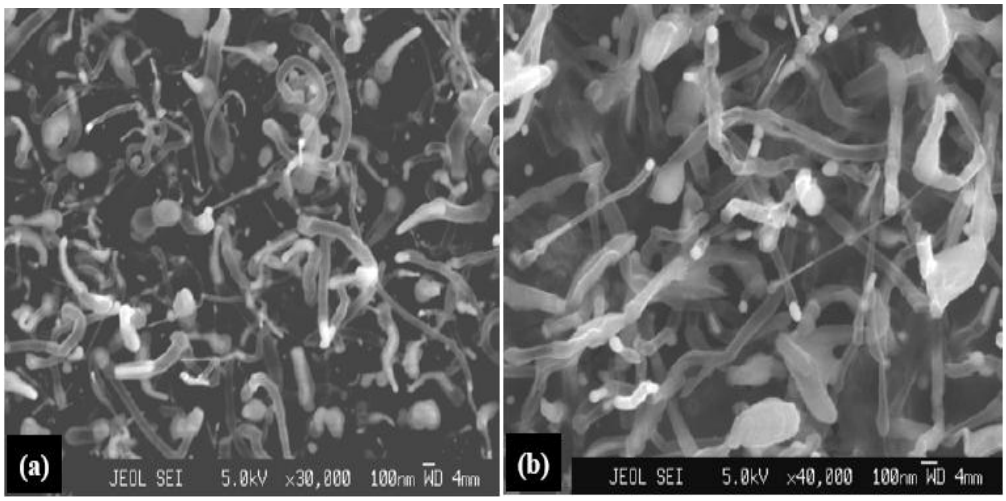

Figure 7. Scanning electron micrographs of CNTs grown using Ni film annealed at 500 °C and different H_2:CH_4 gas ratios: (a) 4:1 and (b) 8:1.

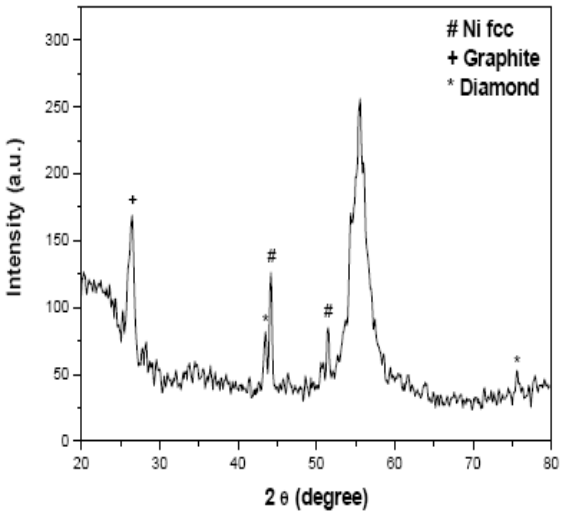

Figure 8. GIRXD pattern for carbon material grown at 900 ^{o}C and H_2:CH_4 gas ratio of 8:1 using Ni film annealed at 500 ^{o}C. The intense peak around 55-60^{o} (2θ) is related to silicon substrate.

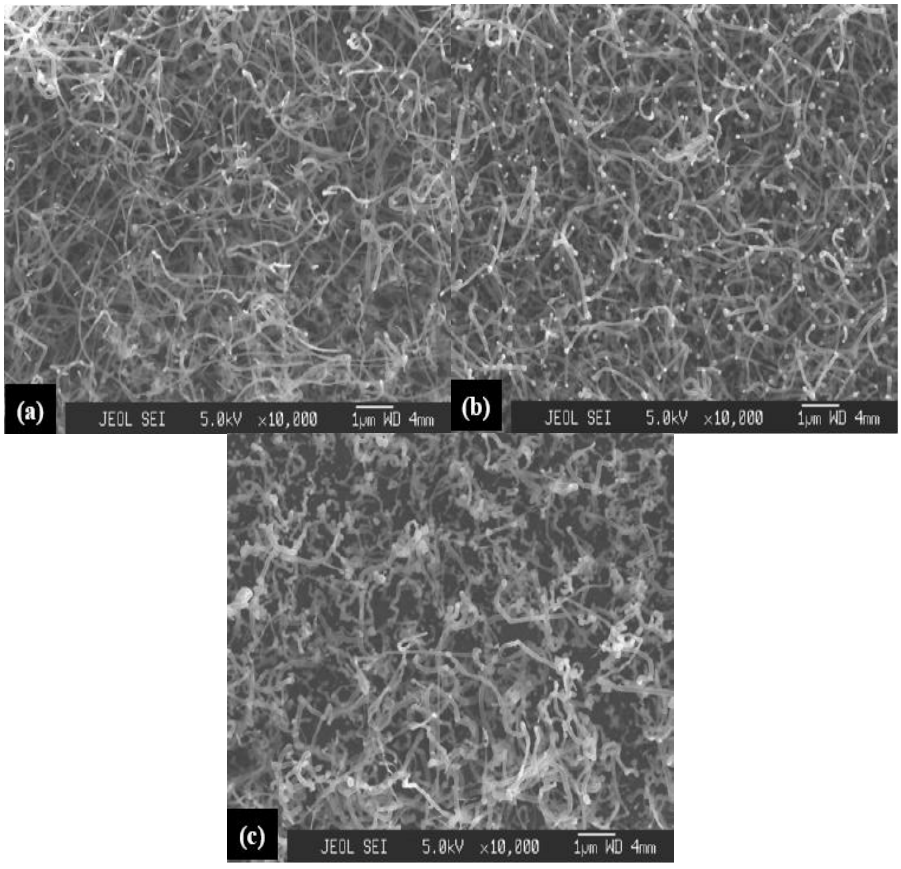

Figure 9. Scanning electron micrographs of CNTs grown using Ni film annealed at 700 ^{o}C and different H_2:CH_4 gas ratios: (a) 4:1, (b) 8:1 and (c) 16:1.

In this case, nickel particles determined the diameter of the nanotubes formed, since the size of catalyst particles is in the same range. As a consequence of the differences promoted by the distinct thermal pre-treatments, the carbon material obtained after annealing at 700 ^{o}C also presented higher order degree, according to the ratio of the D- and G-lines intensities (ID/IG) observed by Raman spectroscopy (Figure 10). This ID/IG ratio is used to characterize the structural defects in carbon nanotubes and higher ID/IG ratio indicates a lower crystallinity of the CNTs. Since the ID/IG ratio values are 0.51 and 0.69 for samples pre-treated at 700 and 500 ^{o}C, respectively, a higher crystallinity is observed for carbon nanotubes prepared from Ni pre-heated at 700 ^{o}C, which shows the importance of the catalyst pre-treatment. Moreover, Raman spectra show a characteristic profile which corroborates the formation of multiwalled carbon nanotubes (MWCNTs), presenting G-line at 1578 cm^{-1} associated to the crystalline graphitic structure and D-line near 1328 cm^{-1} accompanied by a D' band at 1612 cm^{-1} and the second order G' band around 2665 cm^{-1} related to a disordered graphitic structure [40].

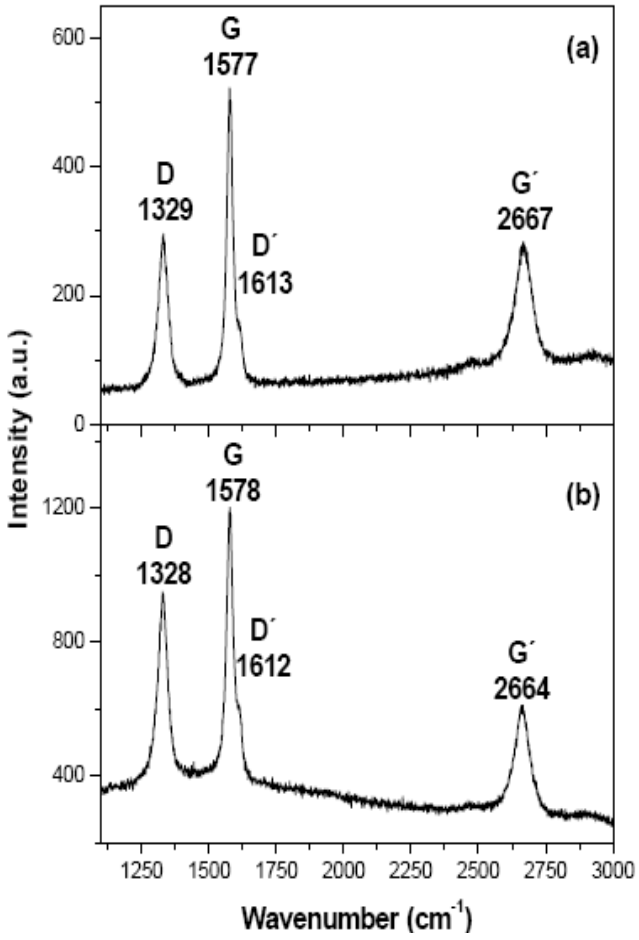

Figure 10. Raman spectra for carbon materials grown at 900 ^{o}C and H_2:CH_4 gas ratio of 4:1 using Ni film annealed at (a) 700 ^{o}C and (b) 500 ^{o}C.

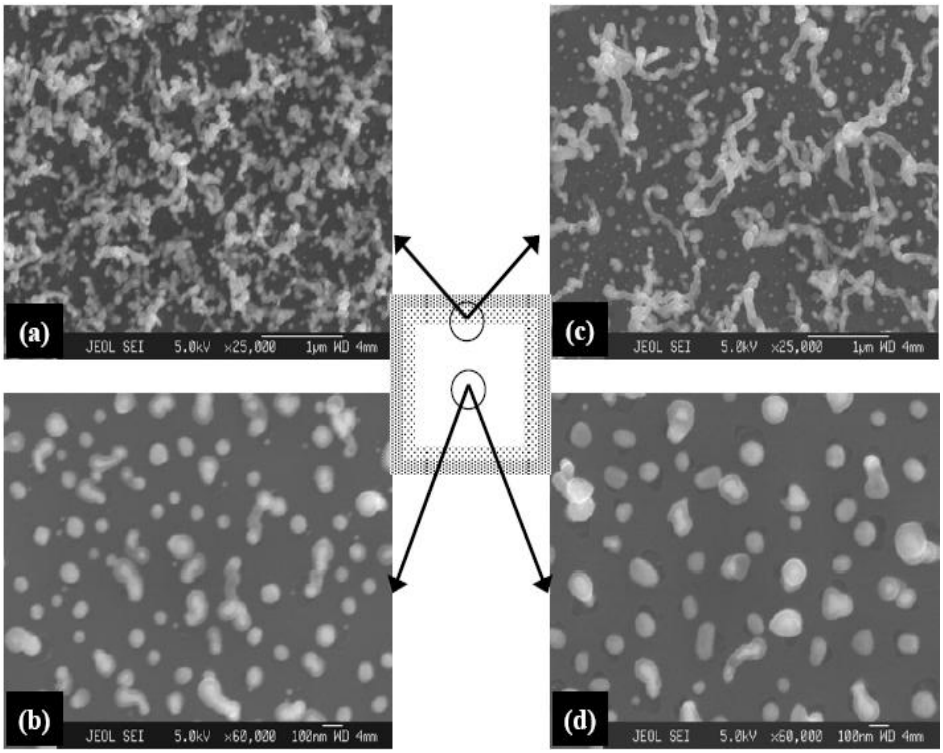

Figure 11. Scanning electron micrographs for CNTs grown using Ni films annealed at 700 ^{o}C, growth temperature of 900 ^{o}C and different H_2:CH_4 gas ratios: (a) and (b) 4:1; (c) and (d) 16:1. Images (a) and (c) were obtained some microns away from the edge; images (b) and (d) were obtained in the central region of the substrate. The central illustration represents a substrate and the gradient of the CNTs density (out of scale).

For these three samples previously described and presented in Figure 9 it was observed a curious phenomenon: the growth of CNTs did not occur over the entire substrate but only in a restrict region, near to the edges, as observed in the SEM images obtained near to substrates edges showing a high CNTs density (Figure 9). Scanning electron micrographs presented in Figure 11 show the CNTs density decreasing from the edge to the central region of the substrate. As shown by Figures 11(a) and (c), SEM images obtained some microns from the edge of the substrate presents carbonaceous material covering metal catalyst, whereas the central region is almost completely dominated by nickel particles covered by a carbon layer (Figures 11(b) and (d)). The same behavior was observed for samples prepared at 950 ^{o}C (not shown). These results suggest that neither temperature nor methane concentration are decisive parameters to improve the CNTs growth all over the substrate.

In the last decade, the formation of metal particles has pay attention due to the CNTs growth using metal film deposited onto a substrate to provide supported metal catalyst particles for the conversion of carbon precursor molecules in carbon nanotubes [^{4}1-44]. Usually, reports bring information about the general influence of the metal film thickness in the particle diameter and the lack of a fine control on the particle size formed by this procedure [5,7,^{4}5,46]. However, there is no mention about differences among metal particles generated from a metal film over a substrate, as suggested by the results observed in this work

due the fact of only a fraction of the particles is able to catalyze the growth of carbon nanotubes.

Investigations are in course to explain and overcome the absence of CNTs grown over the entire substrate. A possible cause may be correlated with the presence of residual oxygen inside the furnace or the release of oxygen due to the possible decomposition of SiO_2 layer catalyzed by the metal film under high temperature [47]. In this case, the metallic nickel could catalyze the following conversion: $SiO_2 \rightarrow ½\ O_2 + SiO$, and the concentration of oxygen released from the silicon oxide layer could be higher at the center compared to the edges of the substrate. In turn, this would result in formation of the nickel oxide (which is known to be much less efficient as a catalyst as compared with the metallic nickel) [1], the process being stronger in the central part of the substrate. Literature data also show non-homogeneity in the CNTs growth being caused by nickel oxidation. Yen et al. [48] observed worm-like carbon fibers, similar to carbon structures shown in Figure 11a and c, when nickel particles were partially oxidized. The catalytic behavior of nickel was also inhibited when a metallic titanium film was deposited between a nickel film and SiO_2 layer due to the titanium and SiO_2 reaction with $TiSi_2$ formation and oxygen release, which led to Ni oxidation [49].

As previously presented in this work, nickel particles were firstly formed in the substrate edge. Since the oxygen can act more effectively over a thinner metal film than in thicker metal particles, the maintenance of the metal film in the central region of the substrate for a larger period of time could accent the formation of oxidized particles and consequent absence of the catalytic growth of CNTs in the meddle of the substrate. Moreover, energetic aspects of the process can also be related with the lack of CNTs formation all over the substrate. Since the methane is a relatively stable carbon gas precursor, with a negative value of heat of formation [25], its decomposition consumes energy from the catalyst particle causing a superficial cooling. The reduction of the temperature can lead to a particle poisoning by the segregation of the dissolved carbon atoms existent inside the particle to the surface, resulting in a carbon layer formation around the metal particle and consequent catalyst deactivation either before or after the CNTs nucleation, the process being more effective for oxidized particles due to their less catalytic efficiency (Figure 12).

Previous experiments using acetylene (a more reactive carbon precursor gas) showed a high density of carbon nanotube grown even under softened experimental conditions, such as lower growth temperature and carbon supply, compared to methane. In this case, the higher reactivity of acetylene made the growth process less sensitive to variations of the metal catalytic capacity, resulting in more uniform CNTs growth in all regions of the substrate. Since its heat of formation is a positive value higher than 50 Kcal mol^{-1} [25], acetylene decomposition releases energy to the catalyst particle causing a superficial heating, which can improve the metal catalyst capability.

In search of explanations for our results, experiments employing acetylene with reduced growth time (only 1 or 2 minutes) were performed. A very similar behavior, compared to methane experiments, was observed when growth time was 1 minute: CNTs grown only in the substrate edge (Figure 13). When growth time was increased to 2 minutes, carbon nanotube growth took place all over the substrate (Figure 14). Probably, differences in metal particles lead to different nucleation time among particles in the central region of the substrate compared to the particles near to the edge and, the energetic aspects of the growth process involving methane result in the poisoning of the particles in detriment of the CNTs formation.

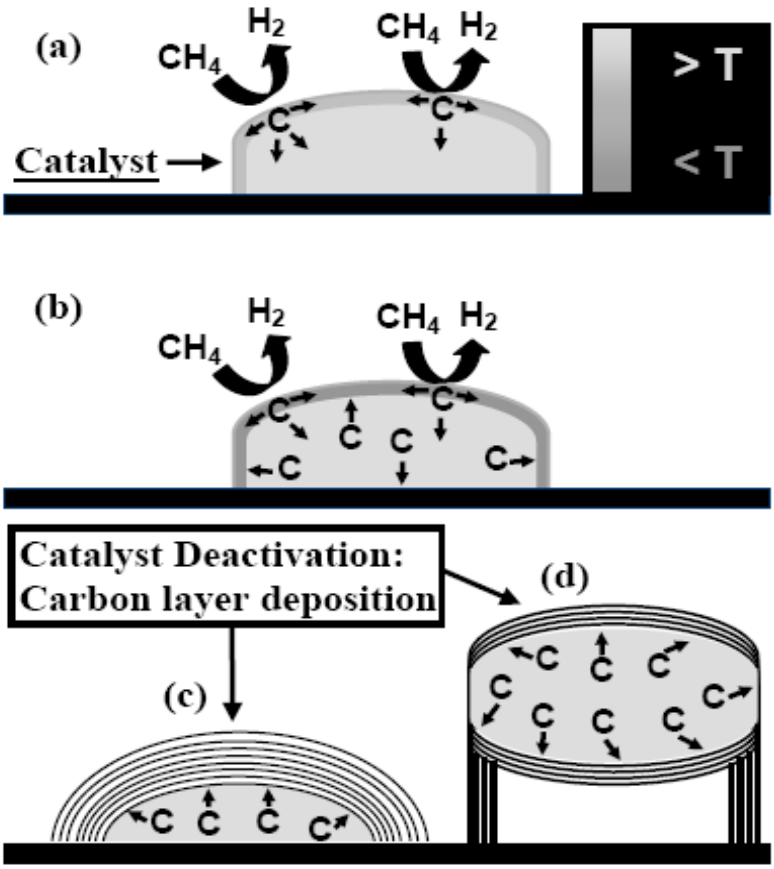

Figure 12. Representation of the catalyst deactivation promoted by the metal particle cooling during the methane decomposition (a, b), due to the carbon layer deposition around the particle before (c) or after (d) the CNT nucleation.

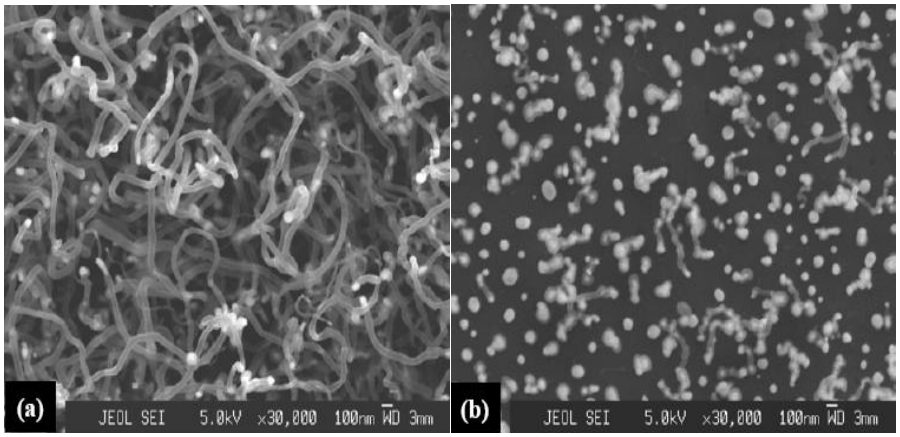

Figure 13. Scanning electron micrographs for CNTs grown using Ni film annealed at 700 ^{o}C. The growth was performed at 800 ^{o}C using H_2:C_2H_2 gas ratio of 40:1 during 1 minute. Image (a) was obtained in the edge whereas image (b) was obtained in the central region of the substrate.

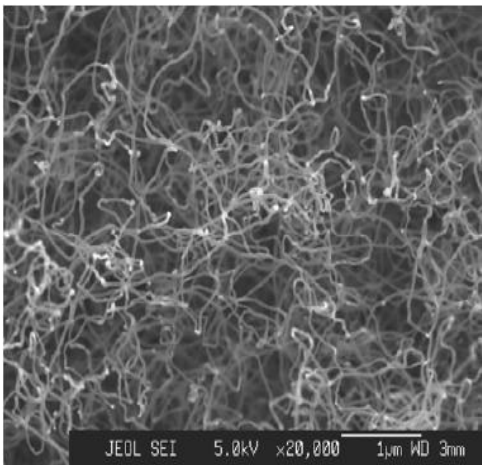

Figure 14. Scanning electron micrograph for CNTs grown using Ni film annealed at 700 ^{o}C. The growth was performed at 800 ^{o}C, using H_2:C_2H_2 gas ratio of 40:1 during 2 minutes. The image is characteristic of the entire sample.

CONCLUSIONS

According to our observations, different annealing temperatures led to the formation of metal particles with different characteristics that modified their catalytic properties. Thus, these results indicated that the initial features of the catalyst can influence the carbon material formed during the growth process. Along with the differences among catalyst particles over the substrate, energetic aspects related to the carbon precursor gas decomposition are also crucial for the CNTs formation. As a general trend, in the catalytic thermal chemical vapor deposition process, the carbon nanotube growth is very sensitive to the experimental conditions and a specific combination of different growth parameters has to be reached to obtain the desired final material.

ACKNOWLEDGMENTS

The work was financially supported by CNPq and INCT NAMITEC. The authors would like to thank LME/LNLS, Campinas, Brazil, by the use of scanning electron microscope, LEM/USP, São Paulo, Brazil, by the use of Raman spectrometer, and LQES/UNICAMP, Campinas, Brazil, by the use of TA equipment.

REFERENCES

[1] E.S. Snow, F.K. Perkins, *Nano Lett*., 5 (2005) 2414.

[2] P. Beecher, P. Servati, A. Rozhin, A. Colli, V. Scardaci, S. Pisana, T. Hasan, A.J. Flewitt, J. Robertson, G.W. Hsieh, F.M. Li, A. Nathan, A.C. Ferrari, W.I. Milne, *J. Appl. Phys.* 102 (2007) 043710.

[3] K. Subramanian, Y.M. Wong, W.P. Kang, J.L. Davidson, B.K. Choi, M. Ho, *Diamond Relat. Mater*. 16 (2007) 1997.
[4] W. Hoenlein, G.S. Duesberg, A.P. Graham, F. Kreupl, M. Liebau, W. Pamler, R. Seidel, E. Unger, *Microelectron. Eng*. 83 (2006) 619.
[5] K.Y. Shin, H.C. Su, C.H. Tsai, *J. Vac. Sci. Technol.* B 24 (2006) 358.
[6] R.E. Morjan, M.S. Kabir, S.W. Lee, O.A. Nerushev, P. Lundgren, S. Bengtsson, Y.W. Park, E.E.B. Campbell, *Curr. Appl. Phys.* 4 (2004) 591.
[7] S.R. Lustig, E.D. Boyes, R.H. French, T.D. Gierke, M.A. Harmer, P.B. Hietpas, A. Jagota, R.S. McLean, G.P. Mitchell, G.B. Onoa, K.D. *Sams, Nano Lett*., 3 (2003) 1007.
[8] W. Hoenlein, F. Kreupl, G.S. Duesberg, A.P. Graham, M. Liebau, R. Seidel, E. Unger, *Mater. Sci. Eng*., C 23 (2003) 663.
[9] S. Musso, S. Porro, M. Vinante, L. Vanzetti, R. Ploeger, M. Giorcelli, B. Possetti, F. Trotta, C. Pederzolli, A. Tagliaferro, *Diamond Relat. Mater*. 16 (2007) 1183.
[10] R. Xiang, G. Luo, Z. Yang, Q. Zhang, W. Qian, F. Wei, *Nanotechnology* 18 (2007) 415703.
[11] Y. Li, B. Zhang, X. Xie, J. Liu, Y. Xu, W. Shen, *J. Catal*. 238 (2006) 412.
[12] A. Jungen, S. Hofmann, J.C. Meyer, C. Stampfer, S. Roth, J. Robertson, C. Hierold, J. *Micromech. Microeng*. 17 (2007) 603.
[13] R.L. Vander Wal, T.M. Ticich, V.E. Curtis, *Carbon* 39 (2001) 2277.
[14] A. Reyhani, S.Z. Mortazavi, O. Akhavan, A.Z. Moshfegh, Sh. Lahooti, *Appl. Surf. Sci.* 253 (2007) 8458.
[15] C. Veríssimo, S.A. Moshkalyov, A.C.S. Ramos, J.L. Gonçalves, O.L. Alves, J.W. Swart, J. *Braz. Chem. Soc*. 17 (2006) 1124.
[16] H. Ichi-oka, N. Higashi, Y. Yamada, T. Miyake, T. Suzuki, *Diamond Relat. Mater*. 16 (2007) 1121.
[17] I. Martin-Gullon, J. Vera, J.A. Conesa, J.L. González, C. Merino, *Carbon* 44 (2006) 1572.
[18] C.L. Cheung, A. Kuetz, H. Park, C.M. Lieber, *J. Phys. Chem*. B 106 (2002) 2429.
[19] M.A. Ermakova, D.Yu. Ermakov, A.L. Chuvilin, G.G. Kuvshinov, *J. Catal.* 201 (2001) 183.
[20] M.A. Ermakova, D.Yu. Ermakov, *Kinet. Catal.* 44 (2003) 268.
[21] A. Malesevic, H. Chen, T. Hauffman, A. Vanhulsel, H. Terryn, C.V. Haesendonck, *Nanotechnology* 18 (2007) 455602.
[22] J.H. Yen, I.C. Leu, C.C. Lin, M.H. Hon, *Diamond Relat. Mater*. 13 (2004) 1237.
[23] M. Cantoro, S. Hofmann, S. Pisana, C. Ducati, A. Parvez, A.C. Ferrari, J. Robertson, *Diamond Relat. Mater*. 15 (2006) 1029.
[24] K. Bartsch, B. Arnold, R. Kaltofen, C. Täschner, J. Thomas, A. Leonhardt, *Carbon* 45 (2007) 543.
[25] M.P. Siegal, D.L. Overmyer, F.H. Kaatz, *Appl. Phys. Lett*. 84 (2004) 5156.
[26] S. Hofmann, C. Ducati, J. Robertson, B. Kleinsorge, *Appl. Phys. Lett*. 83 (2003) 135.
[27] G. Bertoni, C. Cepek, F. Romanato, C.S. Casari, A.L. Bassi, C.E. Bottani, M. Sancrotti, *Carbon 4*2 (2004) 423.
[28] J.A. Rodriguez, J.C. Hanson, A.I. Frenkel, J.Y. Kim, M. Pérez, *J. Am. Chem. Soc*. 124 (2002) 346.
[29] K.J. Duxstad, E.E. Haller, K.M. Yu, *J. Appl. Phys*. 81 (1997) 3134.
[30] W.C. Maskell, N.M. Sammes, B.C.H Steele, *J. Phys. D: Appl. Phys*. 20 (1987) 99.

[31] P.R. Gadkari, A.P. Warren, R.M. Todi, R.V. Petrova, K.R. Coffey, *J. Vac. Sci.* Technol. A 23 (2005) 1152.
[32] M.D. Thouless, IBM J. *Res. Develop*. 38 (1994) 367.
[33] E. Jiran, C.V. Thompson, J. Electron. Mater. 19 (1990) 1153; C.V. Thompson, *Thin Solid Films* 208 (1992) 23.
[34] W. Kan, H. Wong, J. Appl. Phys. 97 (2005) 043515.
[35] E.F. Kukovitsky, S.G. L'vov, N.A. Sainov, V.A. Shustov, L.A. Chernozatonskii, *Chem. Phys. Lett*. 355 (2002) 497.
[36] J.A. Moulijn, A.E. van Diepen, F. Kapteijn, *Appl. Catal. A: Gen*. 212 (2001) 3.
[37] D. Nicholls, in: J.C. Bailar, Jr., H.J. Emeléus, R. Nyholm, A.F. Trotman-Dickenson (Eds.), The Chemistry of Iron, Cobalt and Nickel, *Pergamon Texts in Inorganic Chemistry*, vol. 24; Pergamon, Oxford, 1973, p. 1112.
[38] X-ray Powder Diffraction File JCPDS-ICDD (Joint Committee on Powder Diffraction Standards-International Centre for Diffraction Data) (1997).
[39] C. Ducati, I. Alexandrou, M. Chhowalla, G.A.J. Amaratunga, J. Robertson, *J Appl. Phys.* 92 (2002) 3299.
[40] V.P. Dymont, M.P. Samtsov, E.M. Nekrashevich, Tech. Phys. 45 (2000) 905; T. de los Arcos, M.G. Garnier, P. Oelhafen, D. Mathys, J.W Seo, C. Domingo, J.V. García-Ramos, S. Sánchez-Cortés, *Carbon* 42 (2004) 187.
[41] J.D. Carey, L.L. Ong, S.R.P. Silva, *Nanotechnology* 14 (2003) 1223.
[42] S.A. Moshkalyov, A.L.D. Moreau, H.R. Guttiérrez, M.A. Cotta, J.W. Swart, *Mater. Sci. Eng. B* 112 (2004) 147.
[43] M. Chhowalla, K.B.K. Teo, C. Ducati, N.L. Rupesinghe, G.A.J. Amaratunga, A.C. Ferrari, D. Roy, J. Robertson, W.I. Milne, *J. Appl. Phys.* 90 (2001) 5308.
[44] V.I. Merkulov, D.H. Lowndes, Y.Y. Wei, G. Eres, E. Voelkl, *Appl. Phys. Lett*. 76 (2000) 3555.
[45] Th. D. Makris, R. Giorgi, N. Lisi, L. Pilloni, E. Salernitano, F. Sarto, M. Alvisi, *Diamond Relat. Mater*. 13 (2004) 305.
[46] C. Bower, O. Zhou, W. Zhu, D.J. Werder, S. Jin, *Appl. Phys. Lett*. 77 (2000) 2767.
[47] Y. Yao, L.K.L. Falk, R.E. Morjan, O.A. Nerushev, E.E.B. Campbell, *J. Mater. Sci.: Mater. Electron*. 15 (2004) 533.
[48] J.H. Yen, I.C. Leu, C.C. Lin, M.H. Hon, *Diamond Relat. Mater*. 13 (2004) 1237.
[49] M.S. Kabir, R.E. Morjan, O.A. Nerushev, P. Lundgren, S. Bengtsson, P. Anokson, E.E.B. Campbell, *Nanotechnology* 16 (2005) 458.